5-2004

Alpha and Gamma-ray Spectroscopic Studies of Au, Pt, and Ir Nuclei Near the Proton Dripline

Tuck-Meng Goon
University of Tennessee, Knoxville

To the Graduate Council:

I am submitting herewith a dissertation written by Tuck-Meng Goon entitled "Alpha and Gamma-ray Spectroscopic Studies of Au, Pt, and Ir Nuclei Near the Proton Dripline." I have examined the final electronic copy of this dissertation for form and content and recommend that it be accepted in partial fulfillment of the requirements for the degree of Doctor of Philosophy, with a major in Physics.

Leo L. Riedinger, Major Professor

We have read this dissertation and recommend its acceptance:

Carol Bingham, Witek Nazarewicz, Rick Williams

Accepted for the Council:

Carolyn R. Hodges

Vice Provost and Dean of the Graduate School

(Original signatures are on file with official student records.)

To the Graduate Council:

I am submitting herewith a dissertation written by Tuck-Meng Goon entitled "Alpha and Gamma-ray Spectroscopic Studies of Au, Pt, and Ir Nuclei Near the Proton Dripline" I have examined the final paper copy of this dissertation for form and content and recommend that it be accepted in partial fulfillment of the requirements for the degree of Doctor of Philosophy, with a major in Physics.

Leo L. Riedinger, Major Professor

We have read this dissertation
and recommend its acceptance:

Accepted for the Council:

Vice Provost and Dean of
Graduate Studies

Alpha and Gamma-ray Spectroscopic Studies of Au, Pt, and Ir Nuclei Near the Proton Dripline

A Dissertation
Presented for the
Doctor of Philosophy
Degree
The University of Tennessee, Knoxville

Tuck-Meng Goon

May 2004

This dissertaion is dedicated to my
mom (*Chuah Kooi-Cheng*) and dad (*Goon Swee-Loong*)

ACKNOWLEDGMENT

Many thanks to all the people who have helped to make this dissertation a reality. First and foremost, I would like thank my primary adviser, Dr. Lee Riedinger for providing valuable guidance to me and also being such a wonderful adviser. He has always managed to find time to discuss physics and imparting many skills to me despite having many administrative duties as the deputy director for science and technology at the Oak Ridge National Laboratory. I would like to give my greatest gratitude to Dr. Daryl Hartley who spent so much time advising and teaching me about experimental analysis and the physics of high-spin spectroscopy. I would like to thank Dr. Carrol Bingham for advising and guiding me after Dr. Hartley left for a position at the U.S. Naval Academy. Without Dr. Bingham, my understanding of the properties of α decay would be incomplete. The many theoretical discussions I had with Dr. Jingye Zhang are greatly appreciated.

Special thanks to Drs. Mike Carpenter and Filip Kondev of the Argonne National Laboratory (ANL) for their advise and input. I will never forget all the interesting discussion and video conferences we had. I would like to acknowledge all the help and support provided by the staff and the Physics Support Group of the ATLAS accelerator facility in various phases of the experiment. Also I would like to thank my committee members, Drs. Witek Nazarewicz and Rick Williams for reviewing this manuscript. I am grateful to Dr. Nazarewicz for introducing me to the theoretical field of nuclear structure. Finally, I would like to thank my family for their support.

ABSTRACT

This dissertation reports the observation of α-decay and in-beam level structures in the neutron-deficient nuclei ^{176,174}Au, ^{173,174}Pt, and ^{175}Ir from an experiment which was performed at Argonne National Laboratory (ANL). A beam of ^{84}Sr projectiles was used to bombard ^{92,94,96}Mo targets. From these reactions, the ^{176,178,180}Hg compound nuclei were made which eventually decayed into more than 20 product nuclei. The experiment was performed with the Atlas accelerator and utilized the Gammasphere array at the target position in conjunction with the Fragment Mass Analyzer (FMA) for mass identification and a Double-Sided Silicon Strip Detector (DSSD), which was used to observe the recoiling implants and the alpha particles associated with each nuclide.

The Recoil Decay Tagging method (RDT) was used to study high-spin states in ^{174}Pt populated via the ^{92}Mo(^{84}Sr,2p) and ^{94}Mo(^{84}Sr,2p2n) reactions. The ground-state rotational band of levels has been extended from $I = 14$ to 24 (tentatively 26) and a new side band is observed up to a spin of 21 (tentatively 23). A change or band crossing is observed in the latter structure at a low rotational frequency which is similar to that seen in the ground-state band. The first and second $i_{13/2}$ neutron alignment processes are observed for the first time in ^{174}Pt. Surprisingly, these crossings occur at approximately the same rotational frequency. Total Routhian Surface and Cranked Shell Model calculations are used in an attempt to understand this behavior.

The α-decay properties of ^{174,176}Au, ^{175}Ir, and ^{173}Pt were studied following the ^{92}Mo(^{84}Sr,pn), ^{94}Mo(^{84}Sr,pn), ^{94}Mo(^{84}Sr,3p), and ^{92}Mo(^{84}Sr,2pn) reactions, respectively. Correlations between first- and second-generation α decays and γ-ray transitions in daughter nuclei were measured, giving evidence for fine structure α peaks in these odd-odd gold nuclei. Inverse RDT was used to provide further collaborating evidence. Four α decay lines, including three new transitions, were observed and assigned to ^{176}Au. ^{174}Au was observed to have four α decay lines including two newly discovered transitions. In addition, excited states in ^{174,176}Au and ^{172}Ir have

been observed for the first time by use of RDT method. Spin and configuration assignments are discussed.

TABLE OF CONTENTS

LIST OF TABLES

LIST OF FIGURES

CHAPTER 1

Introduction

The study of the atomic nucleus involves a vast collection of phenomena, many still not fully understood [1]. The study of nuclear physics began with the discovery of radioactivity by Becquerel in 1896 and continues today with the discovery of new phenomena. Investigation of such phenomena is a continuous effort where nuclear physicists have developed and improved techniques in order to study a greater variety of nuclear properties. This dissertation focuses on some of the most enduring topics of study in nuclear physics - isomerism and shape co-existence. The development of very sensitive mass separation and detection techniques has enabled the study of these phenomena far from the valley of stability.

Information on nuclear properties is usually obtained via the detection of particle and radiation emissions following the excitation of nuclear matter. One of the commonly used methods employed by nuclear physicists to excite the nucleus is the fusion-evaporation reaction. In such a reaction, high nuclear angular momentum is applied to the system when a target nucleus is bombarded with an accelerated nucleus that has enough energy to overcome the Coulomb repulsion. A great deal of information can be obtained from the emissions of γ rays and α particles from the rapidly rotating unstable nucleus that is formed after the evaporation of free neutrons, protons, and/or α particles. The experimental devices and techniques used in detecting and analyzing data are discussed in Chapter 3.

This dissertation work focuses on the study of structures of nuclei near the $Z=$ 82 shell gap and the proton dripline by using γ-ray and α-decay measurements and the Recoil Decay Tagging method [2, 3] (in sec. 3.3). This powerful technique enables the study of high-spin states in a nucleus (*e.g.*, ^{174}Pt in Chapter 4) produced

near the proton dripline with extremely small cross-section. It identifies specific in-beam γ rays which feed the ground or excited state by correlation with the emitted α particle. This method can also be used to study α particles by employing the associated in-beam structure as a "tagging" marker (^{175}Ir in Chapter 5).

The primary nuclei studied in this work are ^{174,176}Au, ^{173,174}Pt, and ^{172}Ir. Fig. 1.1 displays the location of these nuclei on the theoretical nuclear deformation chart. One can see that the nuclei of interest are found close to the edge of a spherical region defined by dark lines at $Z = 82$ and $N = 82$ (magic numbers). This figure illustrates the particle number effects on the shape of the nucleus where one can see the evolutionary change from spherical to deformed shape as the nucleus moves away from the region near the closed shells.

The nuclei studied in this dissertation display structure characteristics of great interest. In this region, the ground-state shape can vary from being well deformed to nearly spherical. A good example of this evolving behavior is observed in the light Pt nuclei with $N \leq 102$. Heavier ^{178,180}Pt [4, 5] are known to exhibit prolate ground-state deformation while lighter ^{172,174}Pt [6, 7] are thought to have near-spherical or γ-soft triaxial shapes.

In addition to triaxiality, many nuclei in the $A = 170$ region are known to exhibit coexistence between an oblate (or a near-spherical ground state) minimum and a prolate minimum which lies a few hundred keV in excitation energy above the ground state. This phenomenon has been observed in ^{172,174,176}Pt [7, 8], ^{179}Hg [9], ^{174,176,178,180}Os [10], and $^{173-177}$Au [11], and has been interpreted in terms of an interaction between deformation-driving intruder orbitals, $\pi h_{9/2}$, $\pi f_{7/2}$, and $\pi i_{13/2}$ and the near-spherical core. Theoretical models, such as the Cranked Shell Model and Total Routhian Surface calculations (see Chapter 2), have been successfully used to discuss such phenomena.

Hild *et al.* [12] suggested that the prolate-driving orbital $\pi h_{9/2}$ [541]1/2 in combination with the $\pi h_{11/2}$ [514]9/2 orbital near the Fermi surface would give rise to isomerism in ^{167,169,171}Re, while in $^{173-177}$Ir [13] and $^{171-177}$Au [11] the orbitals involved are $\pi s_{1/2}$, $\pi h_{11/2}$, and $\pi d_{3/2}$. Furthermore, isomerism has been observed in odd-odd ^{172,174}Ir [13] and ^{174,176}Au (this work), in addition to the odd-A Re, Ir, and

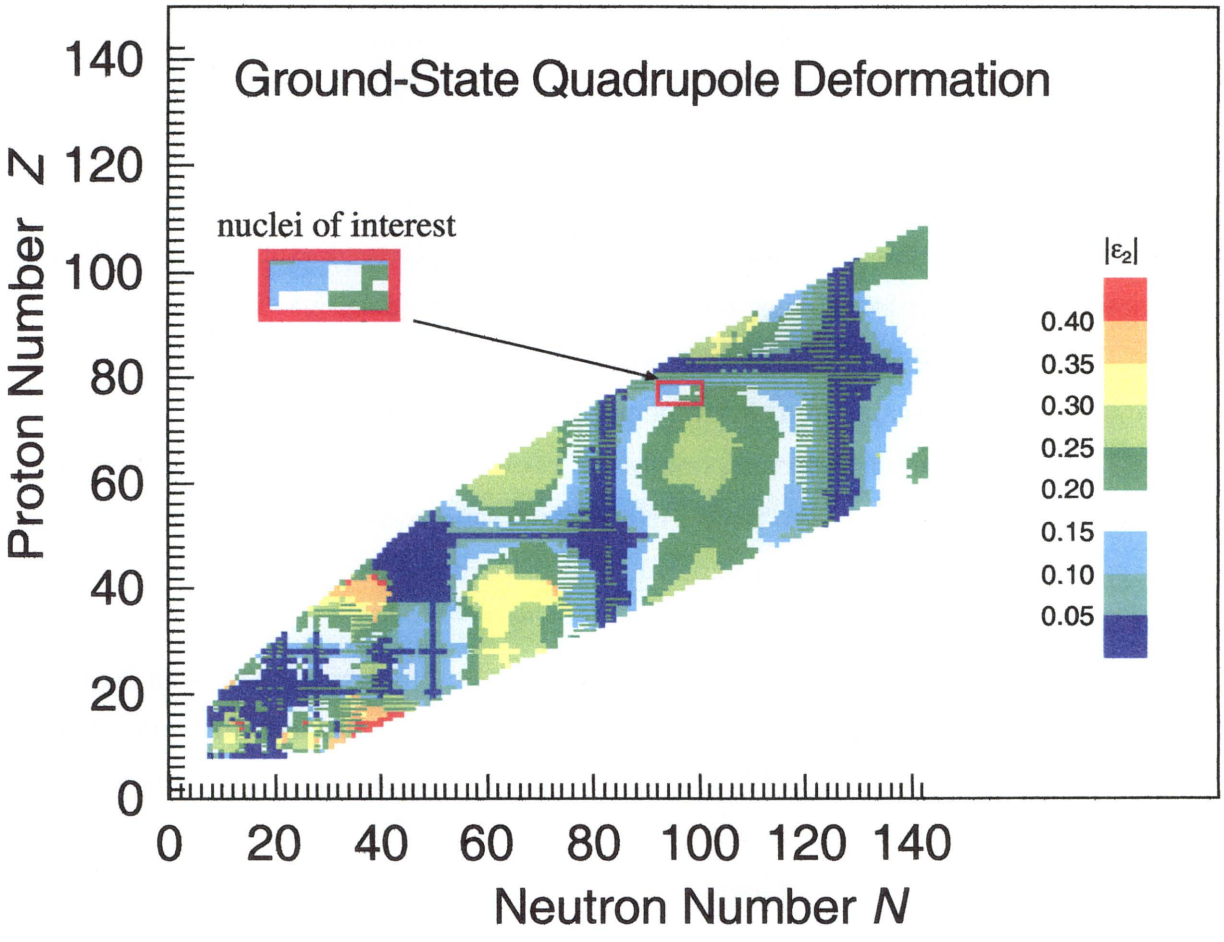

Figure 1.1: Calculated ground-state deformation values ($|\epsilon_2|$) for nuclei. The arrow points to the location of the ^{174,176}Au, ^{173,174}Pt, and ^{172}Ir nuclei (thick square) which will be discussed in this work. Reproduced from Ref. [14, 15].

Au nuclei.

Interpretation of these structures is usually based on data obtained from in-beam γ-ray spectroscopy as well as β and α decay measurements. The first method is used to analyze the behavior of rotational bands of nuclei but often fails to connect these bands with the low-spin and low-energy band members. Therefore, α-decay study of these nuclei coupled with γ-ray spectroscopy data can provide detailed nuclear structure information on the single-particle levels of these neutron-deficient nuclei.

The spectroscopic data for this dissertation were obtained from an experiment at Argonne National Laboratory from December 12 to 20, 1999. Three different reactions were used to produce more than 20 different nuclei (see sec. 3.2). The Recoil Decay Tagging method (sec. 3.3) was employed in this experiment. This method utilized the Gammasphere, the Fragment Mass Analyzer, and a setup at the FMA focal plane of three Ge detectors, one LEPS counter, and a double-sided silicon strip dectector for γ-ray detection, mass identification, and α-decay study, respectively. A more detailed discussion of the experimental devices and techniques can be found in Chapter 3.

In Chapter 4, new α-decay fine structure and high-spin structures including a new side band in ^{174}Pt will be presented. In-beam γ-ray structures and α-decay lines observed for the first time in ^{176,174}Au and ^{172}Ir are presented in Chapter 6. Chapter 5 deals with new α-decay lines observed in ^{173}Pt and ^{175}Ir as well as their α-decay properties such as the reduced-widths, hindrance factors and their associated Nilsson configurations. Finally, a summary of all experimental findings from this dissertation are presented in Chapter 7. In this chapter the advantages of the FMA and RDT method are briefly discussed.

CHAPTER 2

Theoretical Formalism

In order to obtain an understanding of the nuclear system, theoretical models that are able to interpret experimental data may also be able to predict effects not yet observed. It is the experimentalist's job to test the strengths and weaknesses of the model. In the absence of a unified nuclear theory that describes all traits of known nuclei, there are some models which are able to recreate particular nuclear features of interest. The use of the "tunneling" process to describe α decay has been one of the early successes of quantum mechanics. Semi-classical models like the Nilsson model, Total Routhian Surface calculations, and the Cranked Shell Model will be discussed in a qualitative context when applied to nuclear low- and high-spin physics. These models help us to understand how the observed level structures can provide knowledge of the shape of the nucleus under various rotational frequencies and the effect of single-particle motion in a deformed nuclear field. However, other phenomena like nucleon pairing are best described within the framework of the microscopic mean-field theories. The predictive powers and limitations of each model in interpreting experimental results are discussed in the following sections. A brief summary of the theory of nuclear multipole radiation is also presented at the end of this chapter.

2.1 Nuclear Deformation Parameters

Nuclei in their ground or isomeric states can assume a number of different shapes: spherical, oblate (two semi-major axes equal), prolate (two semi-minor axes equal), and triaxial (all three principal axes are different). It is common to describe the nuclear shapes by their deformation parameters. This can be done easily by expanding

the radial vector, R, in terms of the spherical harmonics,

$$R(\theta,\phi) = R_0 \left[1 + \alpha_{00} + \sum_{\lambda=1}^{\infty} \sum_{\mu=-\lambda}^{\lambda} \alpha_{\lambda\mu} Y_{\lambda\mu}(\theta,\phi) \right], \tag{2.1}$$

where R_0 is the radius of a sphere having the same volume as the parameterized shape. The parameter α_{00} is obtained from the condition when nuclear volume is fixed for all deformations. The shifting effect of the whole system is associated with terms which include $\lambda = 1$. The $\alpha_{\lambda\mu}$ constants are kept fixed when the origin is constrained to coincide with the center of mass. For nuclear high-spin spectroscopy, the $\lambda = 2$ and $\lambda = 4$ degrees of freedom in the parameterization of Eqn. 2.1 are sufficient. In order to further simplify the parameterization, the three planes defined by the principal axes are assumed to be symmetrical. Hence, we get the following relations

$$\alpha_{\lambda\mu} = \alpha_{\lambda-\mu}, \text{ and } \alpha_{\lambda\mu} = 0 \text{ for odd } \lambda \text{ or } \mu$$

and, for expansion up to $\lambda = 2$, the radial vector can be represented as

$$R(\theta,\phi) = R_0 \left[1 + \alpha_{00} + \alpha_{20} Y_{20}(\theta',\phi') + 2\alpha_{22} Y_{22}(\theta',\phi') \right]. \tag{2.2}$$

When the "Lund" convention is applied to Eqn. 2.2, α_{20} and α_{22} become $\beta_2 \cos\gamma$ and $-\frac{1}{\sqrt{2}} \beta_2 \sin\gamma$, respectively. β_2 represents the effect of the nucleus being stretched, while the degree of triaxiality is defined by γ. The relationship between nuclear shapes and the deformation parameters β_2 and γ is illustrated in Fig. 2.1.

A non-zero γ value corresponds to a triaxial shape. Prolate and oblate shapes are associated with positive and negative values of β_2, respectively. Both shapes have γ equal to zero. A spherical shape occurs when both β_2 and γ are zero. Another commonly used expansion is the Nilsson parameterization (ϵ_2, ϵ_4, γ, ...) and it is obtained by modifying the characteristic harmonic-oscillator frequencies (ω_1, ω_2, ω_3). The Nilsson parameters are discussed in detail in section 2.3.1.

2.2 Rotations of Axially Symmetric Deformed Nuclei

One of the unique properties of non-spherical nuclei is their ability to undergo rotations about an axis perpendicular to the symmetry axis. The total wavefunction

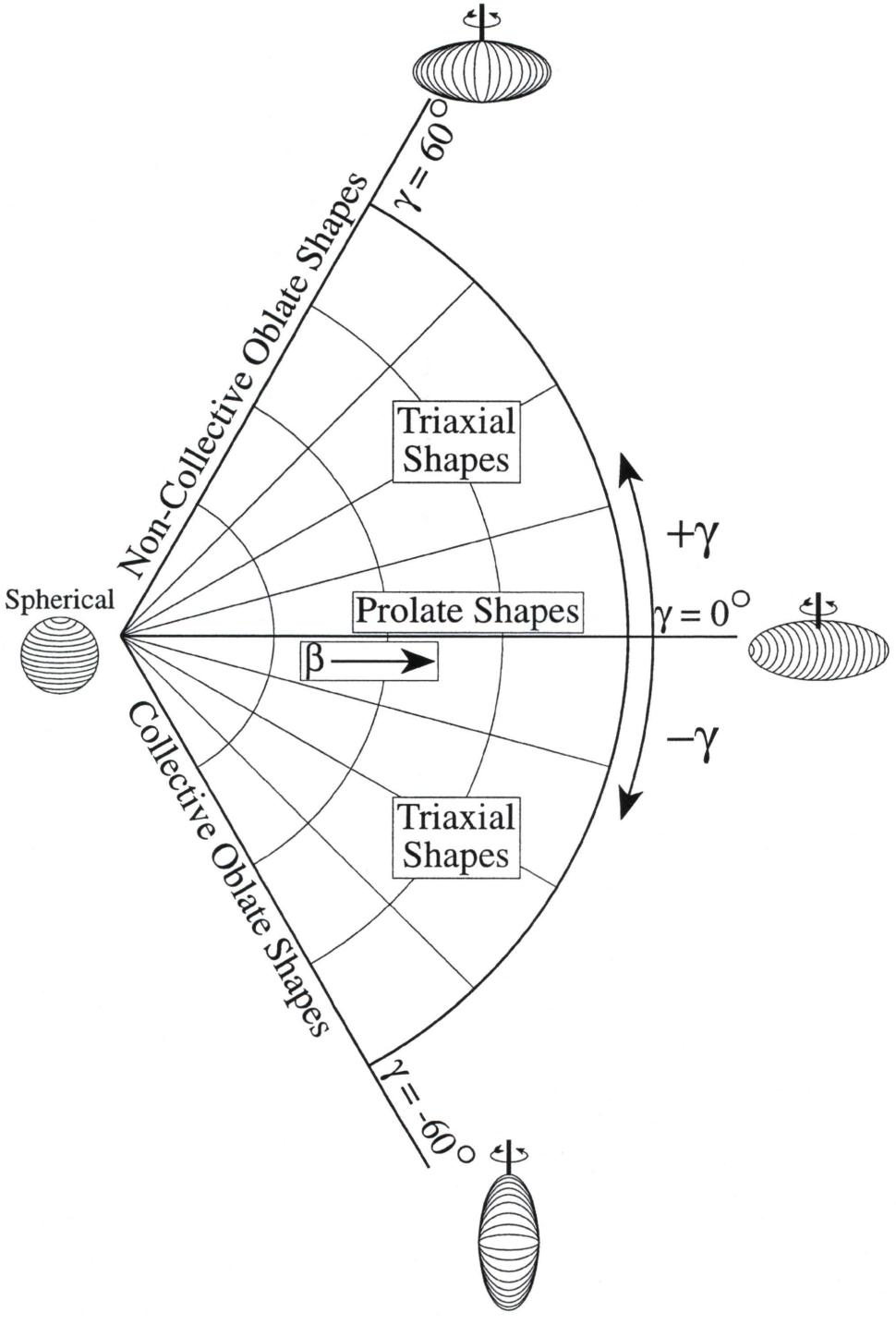

Figure 2.1: The relation between nuclear shapes and the deformation parameters β_2 and γ. These parameters are expressed as polar coordinates. It is assumed that the nucleus rotates along the first axis. Reproduced from Ref. [15].

in a particle-plus-rotor model is defined by specific deformed wavefunction which describes intrinsic excitation (defined by the function χ_K) and a factor to describe the rotational motion (specified by D matrices). For a nucleon in a deformed field, its motions are two-fold degenerate (clockwise and counter-clockwise directions) and are distinguishable by their projection of angular momenta on the symmetry axis, K. A general nuclear wavefunction of a rotating deformed nucleus with nucleons in time-reversed orbitals is given by [1]

$$\Psi_{IM} = \left(\frac{2I+1}{16\pi^2}\right)^{1/2} \left[D_{IMK}\chi_K + (-1)^{I-K} D_{IM-K}\chi_{-K}\right], \tag{2.3}$$

where M and I are the projections of the total angular momentum on the z axis of the rotating coordinate system and the total angular momentum of the nucleus, respectively. When the intrinsic state of χ_K is rotated 180° about the z axis, the time-reversal state χ_{-K} is obtained. From this, one would get a rotational band with a sequence of

$$I = K, K+1, K+2, ... \tag{2.4}$$

When $K = 0$, only even I values are allowed. For a ground state with $I^\pi = 0$, $K = 0$ (e.g. in deformed even-even nuclei), all the angular momentum of the system is ascribed to rotation. This would result in the rotational energy expression for a symmetrical top

$$E_{rot}(I) = \frac{\hbar^2}{2\mathcal{J}} I(I+1), \tag{2.5}$$

where only even I values are allowed and $\mathcal{J}$ is defined as the moment of inertia of the core. Using this expression, the energy ratio $E_{(I=4)}/E_{(I=2)} = 3.33$ for even-even nuclei can be obtained. This ratio is one of the most defining pieces of evidence for deformed rotational motion observed in an atomic nucleus.

2.3 Deformed Shell Model

To discuss the Deformed Shell Model, a brief understanding of nuclear forces and shell structure is required. Until now, the exact nature of the strong nuclear force remains a puzzle, although certain characteristics of it are revealed by a few empirical facts. The

very existence of nuclei which consist of uncharged neutrons and positively charged protons implies that the strong force is attractive and stronger than the Coulomb repulsive force. The repulsive force arises from the interaction between the positively charged protons. It is widely known that the strong force interacts at small range ($\sim 10^{-12}$ to 10^{-13} cm).

Studies from nuclear physics experiments have shown that the interactions between the short-range strong nuclear force, the long-range Coulomb force, and centrifugal stretching due to rotation may give rise to a non-spherical or deformed equilibrium deformed shape. In addition, the evolutionary trend of the protons and neutrons separation energies can also give us some insight into the nature of interaction between nucleons. It is observed that at certain proton and neutron numbers (magic numbers), the binding energies become very pronounced. This trend is quite similar to the large electron ionization energies in nobel gases and small ionization energies of the alkali group. It is this evolutionary trend of the binding energy and other properties that lead to the development of the shell model which is able to reproduce the observed magic numbers correctly. The magic numbers are interpreted from the large gap between certain shells when either the proton or neutron number reaches 2, 8, 20, 28, 50, 82, or 126 (only for neutron).

The independent particle model which is based on the shell structure of the nucleus was developed in order to predict and to reproduce the observed experimental data. It describes a particle moving in a spherical potential and enjoyed great success in the early years of experimental nuclear physics, when nuclear experimentalists were restricted to nuclei near the closed shells and near the valley of stability. However, with the use of more powerful accelerators, which permit the investigation of nuclei far from the shell gap, the independent particle model breaks down. In these heavier nuclei that exist a large number of valence nucleons that interact with each other, leading to complex multi-dimensional systems which do not display shell strcture in a simple picture. It was clear then that new models are required in order to study complex nuclei.

The shape of the nucleus can be obtained by measuring its quadruple moment. From such measurements, it was revealed that magic nuclei are spherical while

nuclei with many valence particles have deformed shapes. This leads to the common understanding that rotational bands observed in heavier nuclei imply axially deformed shapes. In this light, Sven G. Nilsson proposed the Deformed Shell Model in 1955 [16] which described these heavier nuclei in terms of particles moving in a deformed potential.

2.3.1 Nilsson Model

This model has been used extensively to describe the single-particle levels observed in many deformed nuclei. It also provides a microscopic basis for the existence of rotational and vibrational collective motions that are directly linked to the spherical shell model. The Nilsson model [16, 17] uses an axially symmetric harmonic oscillator potential such that the single-particle Hamiltonian takes the form

$$H = \frac{\mathbf{p^2}}{2m} + \frac{1}{2}m\left[{\omega_\perp}^2(x^2+y^2) + {\omega_z}^2 z^2\right] + C\mathbf{l}\cdot\mathbf{s} + D\mathbf{l^2}. \tag{2.6}$$

The first and second terms represent the kinetic energy and harmonic oscillator potential of the particle, respectively. The one-dimensional oscillator frequencies in the x, y, and z directions are defined by ω_x, ω_y, and ω_z. The third term arises from the influence of spin-orbit interaction. This interaction occurs when the particle experiences a force due to the alignment (aligned or anti-aligned) of the orbital angular momentum l with the spin angular momentum s. The fourth term is an attractive term added to the particle orbiting near the edge of the nucleus. This term constrains all nucleons to experience the same potential regardless of their positions in the nucleus. We can obtain the Nilsson eigenvalue E with this Hamiltonian where $\mathrm{H}\psi = \mathrm{E}\psi$ and ψ is the Nilsson wavefunction.

While Eq. 2.6 is written as a function of harmonic potential, it is more common to describe the Hamiltonian in terms of the nuclear deformation parameter, ϵ_2. In order to do that, the frequencies have to be transformed and the transformation equations are

$$\begin{aligned} \omega_x^2 = \omega_y^2 = \omega_\perp^2 &= \omega_0^2(\epsilon_2)(1+\frac{2}{3}\epsilon_2), \\ \omega_z^2 &= \omega_0^2(\epsilon_2)(1-\frac{4}{3}\epsilon_2). \end{aligned} \tag{2.7}$$

The term ω_0 is the oscillator frequency ($\hbar\omega_0 = 41A^{-1/3}$) in the spherical potential (ϵ_2 = 0). This procedure assumes that the volume of the nucleus remains constant as a function of ω_0, with the constraint, $\omega_x\omega_y\omega_z = \omega_0^3$. Using the relations 2.7, we get the transformed potential

$$V_{h.o.} = \frac{\hbar\bar{\omega}}{2}\left[r_t^2 - \epsilon_2 \frac{4}{3}\sqrt{\frac{\pi}{5}}\, r_t^2\, Y_{20}(\theta_t, \phi_t)\right], \tag{2.8}$$

where $\bar{\omega} \equiv (2\omega_\perp + \omega_z)/3$ is defined as the average oscillator strength and the terms r_t, θ_t, and ϕ_t are spherical coordinates in the stretched frame. One of the advantages of transforming the Cartesian coordinate x_i into the stretched coordinate system $x_{t_i} = (m\omega_i/\hbar)^{1/2}x_i$ is that the potential can be separated into two components, spherical and deformed. Therefore, the potential is seen as linearly dependent on ϵ_2 via the second term.

With Eq. 2.8, the Hamiltonian shown in Eq. 2.6 can be solved analytically as a function of ϵ_2 to give the energy eigenvalues plotted in the so-called Nilsson diagrams for neutrons (Fig. 2.2) and protons (Fig. 2.3). It should be noted that at ϵ_2 equals 0, where the nucleus is spherical, the Nilsson model reduces to the spherical shell model and the magic numbers are reproduced. The ϵ_2 value can be either positive or negative and the $\pm$ signs have specific meanings. A positive sign corresponds to a prolate shape (rugby ball) while the negative sign refers to an oblate shape (doorknob). A diagram illustrating these shapes with their corresponding ϵ_2 is shown in Fig. 2.4.

Understanding the Nilsson diagrams can be difficult, however, there are a few qualitative rules that may help to unravel the mystery of the dotted and solid lines. First, consider $\epsilon_2 = 0.0$ in Fig. 2.3 for $50 \leq Z \leq 82$ and notice the shells within this range. Each of these shells, $1g_{7/2}$, $2d_{5/2}$, $1h_{11/2}$, $2d_{3/2}$, and $3s_{1/2}$ can hold $2j + 1$ protons where the j is the angular momentum of the particle in that shell. For a proton orbiting a prolate nucleus in a j orbit, the projection of the j vector onto the symmetry axis z is Ω. So, for a proton in a particular j shell, it can have a specific range of Ω $(j, j-1, ..., 1/2)$. For example, the $1g_{7/2}$ shell has Ω orbitals of 7/2, 5/2, .., 1/2 with each of the orbitals being double degenerate ($|\Omega|$ and $|\text{-}\Omega|$). For $\epsilon_2 > 0$, the energies of low Ω orbitals of the same shell lie lower than high Ω orbitals and vice verse for $\epsilon_2 < 0$ (see Fig. 2.3).

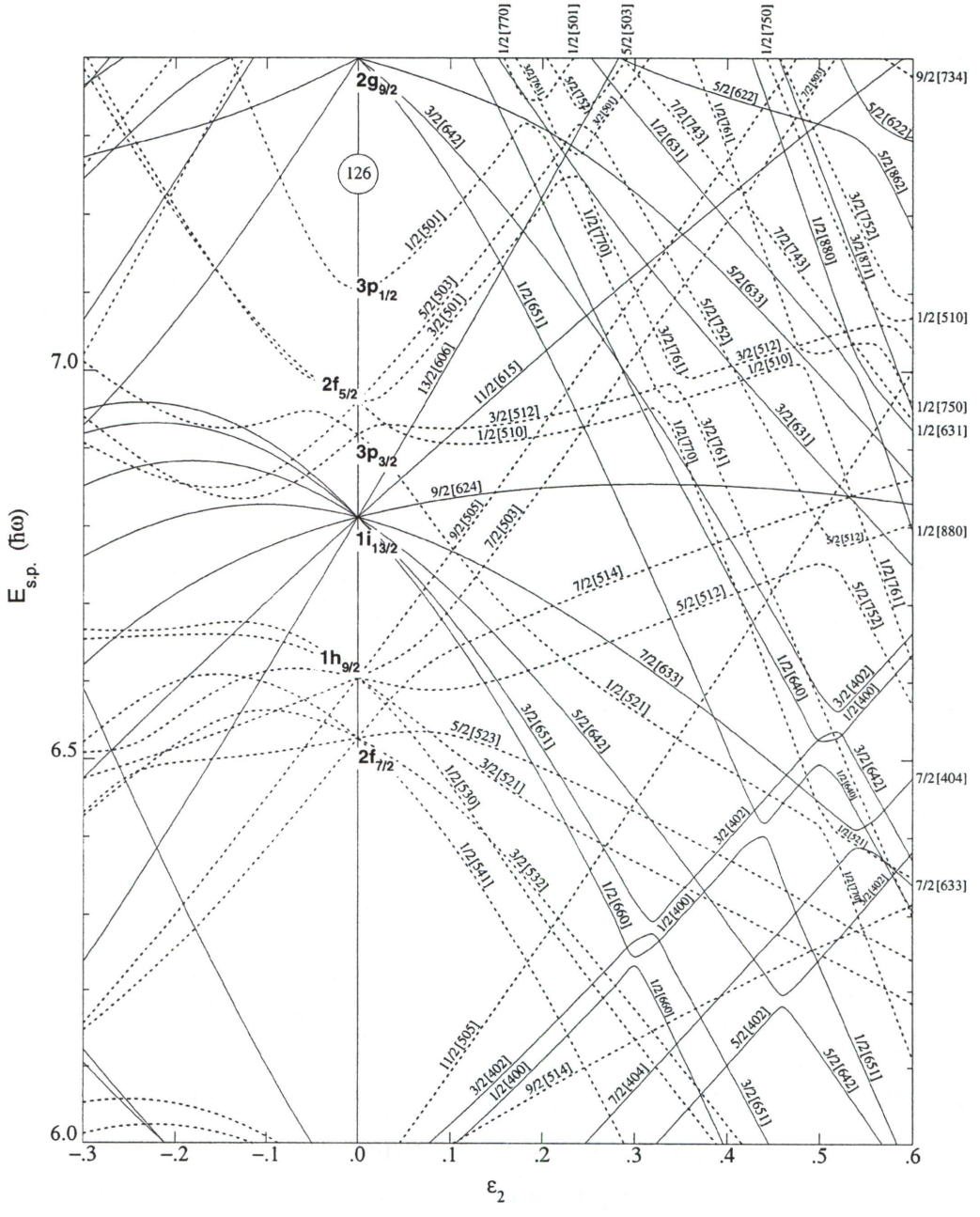

Figure 2.2: Nilsson diagram for neutrons, $82 \leq N \leq 126$ ($\epsilon_4 = {\epsilon_2}^2/6$). Reproduced from Ref. [18].

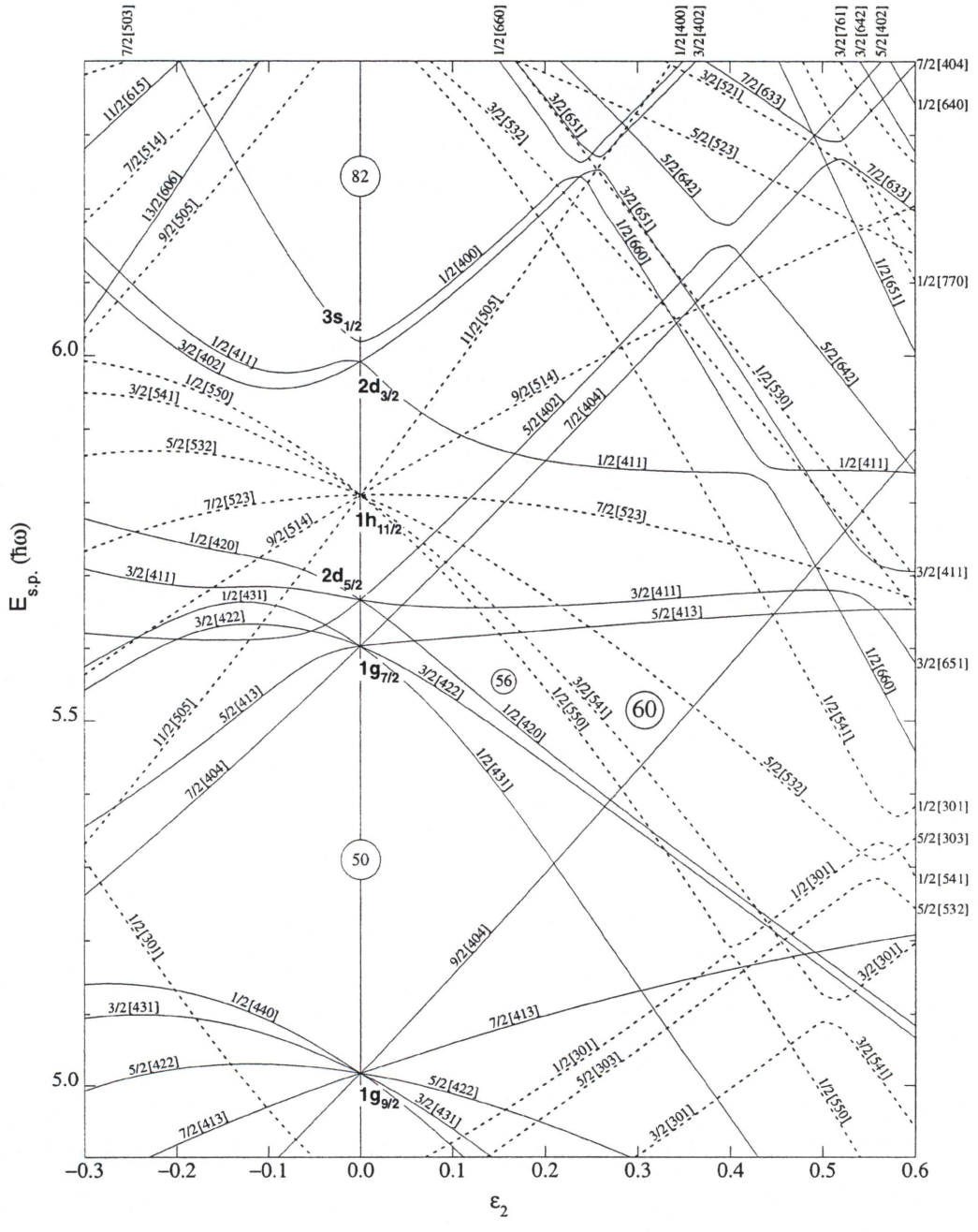

Figure 2.3: Nilsson diagram for protons, $50 \leq Z \leq 82$ ($\epsilon_4 = {\epsilon_2}^2/6$). Reproduced from Ref. [18].

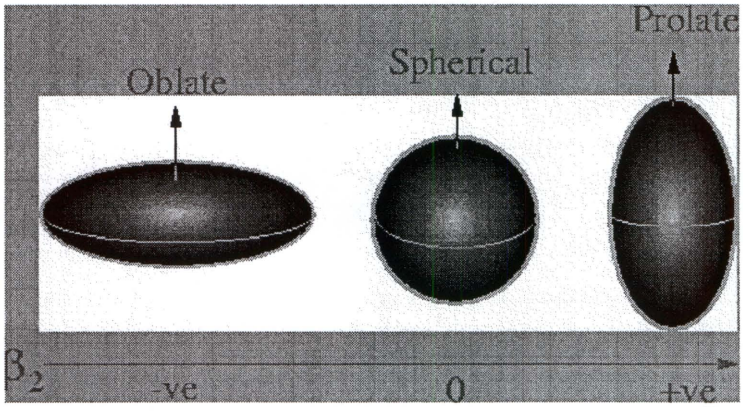

Figure 2.4: Diagram illustrates oblate, spherical, and prolate shapes. The arrows for these shapes indicate the symmetry axis. This figure is taken from Ref. [15].

The Pauli exclusion principle also applies to the Nilsson model where no two orbitals with the same quantum numbers may cross. In the Nilsson diagrams, the only good quantum numbers are parity (π) and Ω. Positive-parity orbitals are denoted by the solid lines while the dotted lines denote negative-parity orbitals. When two orbitals with the same Ω and π approach each other, they repel. Near the inflection point, the two wave-functions are greatly mixed and they exchange "characters". An example of this behavior is shown by the $\Omega = 5/2$ member of the $i_{13/2}$ shell as it moves toward higher deformation (see Fig. 2.2). This orbital remains in its course until another positive-parity $\Omega = 5/2$ orbital arises from a lower shell. At $\epsilon_2 \approx 0.46$, both $\Omega = 5/2$ orbitals repel each other and, soon after the inflection, the line that was labeled 5/2[642] becomes 5/2[402] and vice versa. At the deformation region near the inflection point, the wavefunctions $\psi_{[642]}$ and $\psi_{[402]}$ are mixed. When the orbital from the $i_{13/2}$ passes the inflection point, the $\psi_{[402]}$ becomes more dominant than the $\psi_{[642]}$ hence it resembles later. The exact opposite occurs to the orbital originating from the lower shell. For all intents and purposes, the new down-sloping orbital which virtually points back to the $i_{13/2}$ shell may be considered as the continuation of the $\Omega = 5/2$ orbital of the $i_{13/2}$ shell.

From Figs. 2.2 and 2.3, one sees that each orbital has a specific labeling sequence and is defined as

$$[Nn_z|\Lambda|]\, K^{(\pi)}, \tag{2.9}$$

where $N = n_z + n_y + n_x$, n_z, and Λ are the total oscillator quantum number, oscillator quantum number along the symmetry axis, and the component of angular momentum along the z axis, respectively (see Fig. 2.5). Ω is constrained with two conditions, $\Omega = \Lambda + S_z$ ($S_z = \pm 1/2$) and $n_z + \Lambda$ must have the same parity as N. If N is even then both n_z and Λ are odd and if N is odd, then either n_z or Λ is odd. It is also important to note that the lowest-lying orbital has the highest possible n_z.

In the Nilsson proton diagram, one finds the majority of the orbitals for $50 \leq Z \leq 82$ have positive parity and these are due to the $N = 4$ quantum number. However, one can see the presence of low $h_{11/2}$ negative-parity (due to $N = 5$) orbitals which are due to spin-orbit coupling as described in Eq. 2.6. These unique parity orbitals are known as intruder orbitals and will remain mostly pure because of the absence of other similar negative-parity orbitals. These orbitals are crucial in testing the properties of the ground states of certain mass regions.

2.3.2 Woods-Saxon Model

The use of the Nilsson Hamiltonian has been very successful over the years, however the Nilsson potential is not "realistic" because it does not mimic the real nuclear potential. Therefore, another model which replaces the oscillator potential with the Woods-Saxon potential [19] was created. The Woods-Saxon potential takes the form

$$V_{w.s.} = -V_0 \left[1 + \exp\left(\frac{r - R}{a}\right)\right]^{-1} \tag{2.10}$$

where r, $a \sim 0.5\ fm$, and $V_0 \sim 50$ MeV are the nuclear radius ($R = r_0 \mathrm{A}^{1/3}$, A = mass number), the diffuseness of the potential surface, and the depth of the potential well at $r = 0$, respectively. In this model, the potential is constrained with two conditions. First, it is assumed that a nucleon near the center of the nucleus will feel a uniform potential, i.e no net forces. Secondly, the binding nuclear force is large at the surface ($r = R_0$) and for r greater than the surface radius, the potential goes to zero with increasing r.

In addition to the ability of the potential to reproduce the experimentally observed single-particle levels and the magic numbers, this potential can also simulate

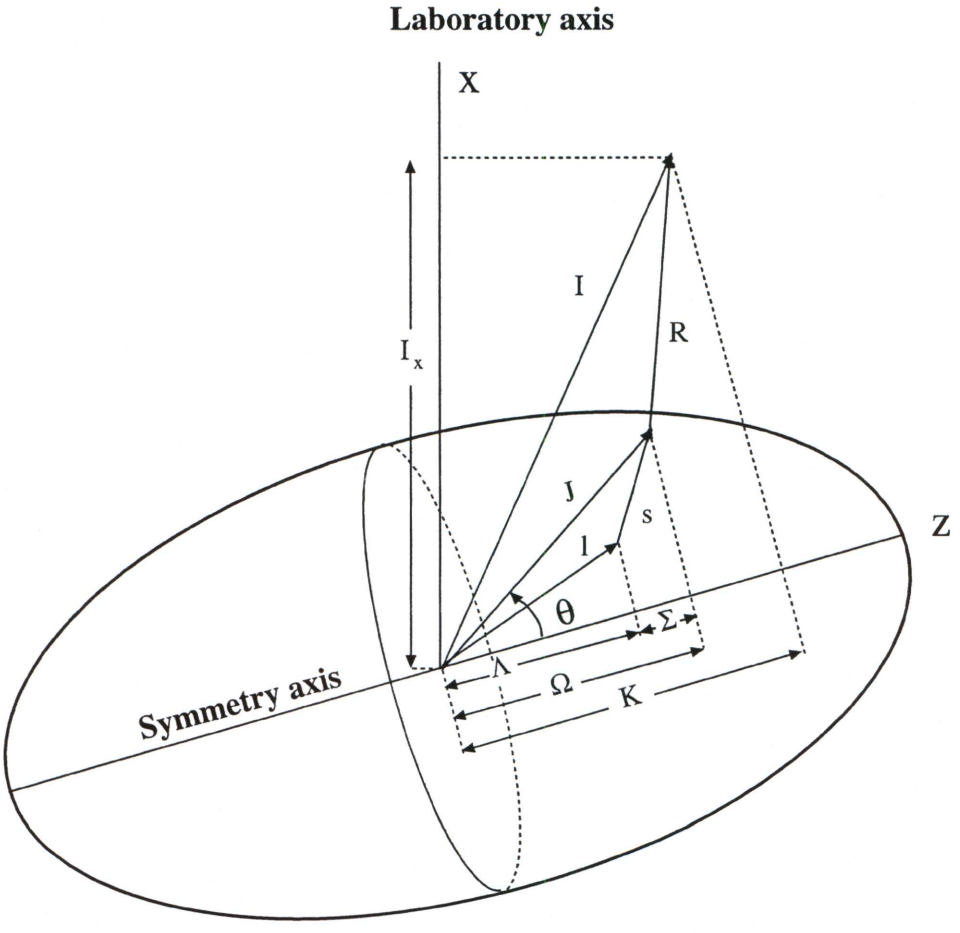

Figure 2.5: Asymptotic quantum numbers of the deformed Nilsson model. For odd-A nuclei, the intrinsic angular momentum J is the total angular momentum of the nucleon. This figure is taken from Ref. [15].

realistic theoretical wavefunctions. The labeling of the Woods-Saxon single-particle orbitals are similar to that of the Nilsson except for the placement of the Ω quantum number. The Ω value in the Woods-Saxon formalism is placed to the right of the bracketed quantum numbers. The deformation parameter also changes from ϵ_2 to β_2 where $\epsilon_2 \approx 0.95\beta_2$ when $\beta_2 \leq 0.2$. There are some subtle differences between the solutions of the two potentials, such as the relative placement of some orbitals, which may occur in certain mass regions.

2.4 The Pairing Interaction

In 1957, Bardeen, Cooper and Schrieffer [20] (BCS) introduced the theory of super conductivity. In this theory, a concept of pairing was introduced where fermions (protons and neutrons) tend to pair with similar fermions. It was not long before the BCS theory was incorporated in the nuclear structure theory [21] when experimental evidence supported the needs for a pairing correlation. Examples of these included the large odd-even mass differences due to a large gain in binding energy of even-even nuclei when compared to neighboring odd-A nuclei, the reduction of moment of inertia when compared to that of a rigid body, modification of the occupation probabilities near the Fermi surface, and the association between $I^\pi = 0^+$ ground states of even-even nuclei and excited particle states that are 1-2 MeV above the ground state.

A qualitative way to describe this phenomenon is to assume that a pair of particles orbit in the same j shell and K orbital but in opposite directions. The pair produces zero net angular momentum. Hence, all even-even nuclear ground states have 0^+ since all nucleons are paired initially. A collision between the two nucleons will occur and scatter them into other equal but opposite (time-reversal) orbitals (see Fig. 2.6). Therefore, there will be equal probability for paired nucleons in a particular j orbital to scatter back into the same or different j orbital. In other words, a pair raised to the next unoccupied orbital would have the observed pairing gap to be twice that of a single particle from j to j'.

Sometimes the 0^+ levels mix and cause the lowering of the ground-state

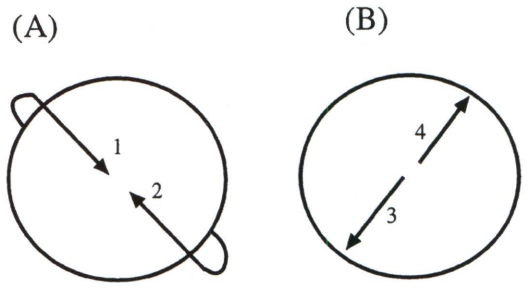

Figure 2.6: Diagram showing two particles in a time-reversed orbit. (A) Particles 1 and 2 collide and s catter into (B). Reproduced from Ref. [22].

energies and creation of a partial occupancy near the Fermi surface. This partial occupancy radicalized the concept of particle and hole excitations as shown by Fig. 2.7. λ is defined as the Fermi level while the ϵ_i corresponds to single-particle energies. The term ϵ_0 is reserved for the one nearest to the Fermi level. The pairing-gap parameter Δ is the summation of the terms over orbitals i, j shown below,

$$\Delta = G \sum_{i,j} U_i V_j, \tag{2.11}$$

where G, U, and V are known as the pairing strength, emptiness, and occupation factors, respectively. The emptiness and occupation factors are expressed by

$$\begin{aligned} U_i^2 &= \frac{1}{2}\left[1 + \frac{\varepsilon_i - \lambda}{E_i}\right], \\ V_i^2 &= \frac{1}{2}\left[1 - \frac{\varepsilon_i - \lambda}{E_i}\right], \end{aligned} \tag{2.12}$$

where ε_i is the single-particle energy and E_i is the energy necessary to excite a quasiparticle (Eqn. 2.13):

$$E_i = \sqrt{(\varepsilon_i - \lambda)^2 + \Delta^2}. \tag{2.13}$$

The plot on the right side of Fig. 2.7 is a plot of the ratio $(\epsilon - \lambda)/\Delta$ versus V^2. The emptiness and occupation parameters are constrained by following relation, $U^2 + V^2 = 1$. Therefore, it is proper to speak of quasiparticles partially filling levels instead particles and holes. An excitation of two-quasiparticle states is given by the following equation,

$$E_{i,j}^{e-e} = \sqrt{(\varepsilon_i - \lambda)^2 + \Delta^2} + \sqrt{(\varepsilon_j - \lambda)^2 + \Delta^2}. \tag{2.14}$$

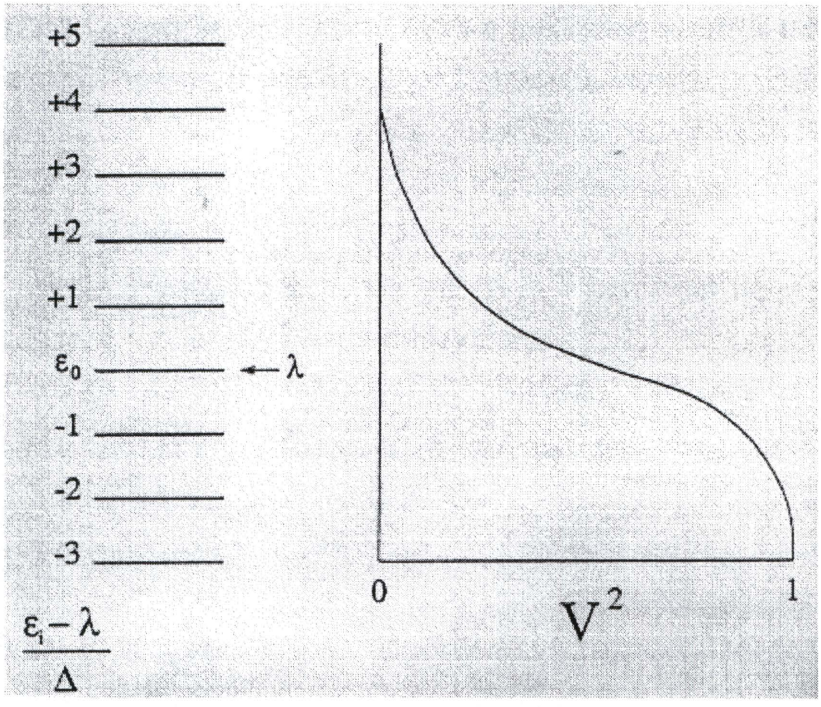

Figure 2.7: Diagram displays partial occupancy due to the effect of pairing. The left side shows an idealized set of equal spaced single-particle levels while the right side displays resultant orbit occupancies V^2. Reproduced from Ref. [22].

From this equation, it is obvious that a minimum of 2Δ in energy is required to observe a two-quasiparticle excitation in even-even nuclei. In fact, it has been observed that many two-quasiparticle structures occur in the 1.5-2 MeV range.

2.5 Cranked Shell Model

As discussed in the previous section, the Deformed Shell Model has been used successfully in determining particular states which are based on the different particle excitations. However, there are some limitations to this model. This model cannot provide information about the excited states that originate from nuclear rotations. In order to solve this problem, Inglis [23, 24] proposed a model to account for the collective rotation around an axis which is perpendicular to the symmetry axis. This model is known as the Cranked Shell Model (CSM) [25, 26] and has proven to be quite useful.

In this model, the deformed nuclear field is rotated externally and constantly with respect to the rotational axis. This would result in an explicit time dependence to the Schrödinger equation. This new equation can be reduced into a stationary equation of motion if the reference frame is transformed into the rotational frame. Furthermore, this transformation allows us to compare theoretical calculations with experimental observations and obtain single particle properties from the nuclear level scheme.

In order to perform this transformation, a rotation operator is required and is given by

$$R(\omega t) = e^{-i\omega t j_x}, \tag{2.15}$$

$$\Psi_{Lab} = R(\Psi_{Int}), \tag{2.16}$$

$$H_{Lab} = R(H_{Int})R^{-1}. \tag{2.17}$$

H and Ψ are the Hamiltonian and wave function of the system while the subscripts *Lab* and *Int* correspond to the lab and intrinsic frames, respectively. Eq. 2.18 is the transformed single particle time-dependent Schrödinger equation for the body fixed

(intrinsic rotating) frame.

$$i\hbar\frac{\partial\Psi_{int}}{\partial t} = (h_0 - \omega j_x)\Psi_{int}. \tag{2.18}$$

The term $h_0 - \omega j_x$ is known as Routhian of the rotational frame. The summation over all independent particles results in the total cranking Hamiltonian

$$H^{\omega} = H_0 - \omega J_x. \tag{2.19}$$

The term ω is the angular frequency of the system and J_x is the angular momentum operator along the axis of rotation x, which is perpendicular to the symmetry axis z. As in classical mechanics, the term ωJ_x corresponds to the centrifugal and Coriolis forces which are the results of the non-inertial system in the rotating frame. From Ref. [1], one can obtain an upper limit strength for the Coriolis force

$$V_{cor} = \frac{\hbar^2}{2\mathcal{J}} Ij \tag{2.20}$$

where I is the total angular momentum, j is the single-particle momentum, and $\mathcal{J}$ is the moment of inertia.

2.6 Symmetries in the Cranking Hamiltonian

In a cranking Routhian, there are only two conserved quantities or symmetries associated with H'. These symmetries are space reflection and rotation of 180° around the rotational axis. Space reflection is described by the parity (π) quantum number, while space rotation is defined by the signature (α) quantum number. The equation below describes the signature,

$$R_x(\pi)\Psi_\alpha = e^{-i\pi j_x}\Psi_\alpha = e^{-i\pi\alpha}\Psi_\alpha \tag{2.21}$$

$$r = e^{-i\pi\alpha} = (-1)^I, \tag{2.22}$$

where Ψ_α, r, and I are the wave function with signature α, the eigenvalue of R_x, and the total nuclear spin, respectively. Since I also depends on the atomic number of the

nucleus, the range of values which r can take is constrained. Therefore, in a system with an even number of nucleons r values are given by the equation below,

$$\begin{aligned} r = \ +1 \ (\alpha = 0), \ I = \ 0, 2, 4, ... \\ r = \ -1 \ (\alpha = 1), \ I = \ 1, 3, 5, ... \end{aligned} \tag{2.23}$$

and for a system with odd particle number,

$$\begin{aligned} r = \ -i \ (\alpha = +\frac{1}{2}), \ I = \ \frac{1}{2}, \frac{5}{2}, \frac{9}{2}, ... \\ r = \ +i \ (\alpha = -\frac{1}{2}), \ I = \ \frac{3}{2}, \frac{7}{2}, \frac{11}{2}, ... \end{aligned} \tag{2.24}$$

Therefore referring to the Eqns. 2.23 and 2.24, one can clearly see that the only good quantum numbers that define states in the CSM are parity and signature, denoted by π and α.

2.7 Total Routhian Surface Calculations

The Routhian energy of a system is dependent not only on the rotational frequency but also on the deformation parameters. It is formulated as

$$E^{\omega}_{n-qp}(\beta) = E^{\omega=0}_{Str}(\beta) + E^{\omega}_{vac}(\beta) + \sum_i E^{\omega}_i(\beta), \tag{2.25}$$

where $E^{\omega=0}_{Str}(\beta)$ and $E^{\omega}_{vac}(\beta)$ are the Strutinsky energy at $\omega = 0$ and the total Routhian energy of the quasiparticle vacuum at ω, respectively. $E^{\omega}_i(\beta)$ is defined as the excitation energy of quasiparticle i and the subscript β represents the deformation parameters β_2, γ, and β_4.

In order to construct the total Routhian surfaces where the Routhian energies are mapped out as function of deformation parameters, $E^{\omega}_i(\beta)$ is calculated at the discrete deformation value β with fixed ω and fixed quasiparticle configuration. The total Routhian, which is minimized against shape parameters, is mapped out in a cartesian plot where the β_2 and γ are transformed into $X = \beta_2 \cos(\gamma+30)$ and $Y = \beta_2 \sin(\gamma+30)$.

The TRS diagrams generated from a particular configuration are used to find the theoretical equilibrium shapes by inspecting the deformation of the TRS

surface that has a minimum. In many respects, there are advantages to the simple form of Eq. 2.25 because the Strutinsky energy needs to be calculated only once, at $\omega = 0$. The only calculations of non-zero rotational frequencies that remain are the calculations of the quasiparticle energies. These calculations are usually done using the HFBC method. Finally, the TRS calculations are performed with a non-axial Woods-Saxon potential as described in Ref. [27]. A more detailed description of these calculations can be found in Ref. [28, 29].

2.8 Transformation of Experimental Observables into the Rotating Frame

In order to test theoretical predictions with experimental results which are obtained in the laboratory frame, the experimental data have to be expressed in the rotating frame [25]. The excitation energy in the laboratory frame E_x is related to the excitation energy, E', in the rotating frame by

$$E' = E_x - \omega I_x \tag{2.26}$$

where I_x is the projection of the total angular momentum on the rotation axis. I_x can also be written in a semi-classical expression using geometrical arguments,

$$I_x(I) = \sqrt{I(I+1) - K^2} \approx \sqrt{(I+\frac{1}{2})^2 - K^2}. \tag{2.27}$$

The rotational frequency may be approximated by the method of finite differences:

$$\omega(I) = \frac{E(I+1) - E(I-1)}{I_x(I+1) - I_x(I-1)} \tag{2.28}$$

where the angular momentum states $I + 1$ and I - 1 correspond specifically to states within a rotational band consisting of $\Delta I = 2$ transitions. The I_x and E' consist of all contributions from collective effects which need to be subtracted since the CSM plot refers only to unpaired particles. The subtraction can be shown with the following relations,

$$e'(\omega) = E'(\omega) - E'_{ref}(\omega) \tag{2.29}$$

$$i(\omega) = I_x(\omega) - I_x^{ref}(\omega). \tag{2.30}$$

In these equations the I_x^{ref} and E'_{ref} are reference functions that simulate the contribution of collective rotation to their respective quantities. The $e'(\omega)$ and $i(\omega)$ are called Routhian and alignment, respectively. This would result in a non-constant moment of inertia that varies with rotational frequencies

$$\mathcal{J} = \mathcal{J}_0 + \mathcal{J}_1\omega^2, \tag{2.31}$$

where $\mathcal{J}_0$, $\mathcal{J}_1$ are known as Harris parameters [30] and they are adjusted for each specific nucleus. The relation between Harris parameters I_x^{ref} and E'_{ref} are given by the equation below

$$I_x^{ref} = \omega\mathcal{J}_0 + \omega^3\mathcal{J}_1. \tag{2.32}$$

Integrating I_x^{ref} with respect to ω gives the energy of the core in the rotating frame which is known as reference Routhian. The intregral is shown below

$$E'_{ref} = -\int I_x^{ref}(\omega)d\omega = -\frac{\omega^2}{2}\mathcal{J}_0 - \frac{\omega^4}{4}\mathcal{J}_1 + \frac{1}{8\mathcal{J}_0}, \tag{2.33}$$

where $I_x^{ref} = -dE/d\omega$ is defined as the canonical Hamilton. The last term in Eq. 2.33, which is a constant of integration, is added to make $E'_{ref} \sim 0$ at $I = 0$ [25].

The phenomenological representations of the quasiparticle vacuum are given by Eqn. 2.32 and 2.33. This quasiparticle vacuum is also associated with the ground-state band for the even-even nucleus. It is also common practice in high-spin spectroscopy to select $\mathcal{J}_0$ and $\mathcal{J}_1$ parameters such that the deformed ground-state band has zero initial alignment.

2.9 Multipole Radiations and Transition Probabilities

In γ-ray spectroscopy, it is common to consider the electromagnetic field as a sum of multipole fields denoted by $\mathcal{M}(\sigma, \lambda)$. The notations σ and λ represent E or M for electric or magnetic fields and the multipole order of the fields, respectively.

For an example, $E2$ is defined as electric quadrupole transition and a magnetic dipole transition is denoted by $M1$. When quantum mechanics are applied to

these fields, there is a restriction on the angular momentum of the initial and final states and the γ ray transition between those states. The angular momentum of the photon is given by the relation, $L = \lambda\hbar$ where λ = 1,2,3,.... This results in the conservation of angular momentum and parity between states as defined by the equations below,

$$I_i = \lambda + I_f, \tag{2.34}$$

$$|(I_i - I_f)| \leq \lambda \leq |I_i + I_f|, \tag{2.35}$$

$$\pi(E\lambda) = (-1)^{\lambda}, \tag{2.36}$$

$$\pi(M\lambda) = (-1)^{\lambda+1}. \tag{2.37}$$

With these relations above, it is clear that if a transition is an electric dipole, there is a change of parity between states while magnetic dipole transition will not change the parity. Another useful relation in nuclear physics is the Weisskopf estimate [31],

$$B(\sigma\lambda) = f_{\sigma}(\lambda)\left(\frac{\hbar c}{E_{\gamma}}\right)^{2\lambda+1}, \tag{2.38}$$

where $f_{\sigma}(\lambda)$ is a complicated expression of λ with a different functional form for magnetic and electric multipoles, and E_{γ} is the γ-ray energy of the electromagnetic transition between two nuclear energy states in MeV. With this equation, a single-particle transition probability can be roughly estimated.

If the measured intensity is much smaller than the Weisskopf estimate, it would indicate that the initial and final wavefunctions are different, while a larger intensity would signal more than one single nucleon at play. Hence this estimate gives a sense of "collectiveness" of the nuclear states connected by that particular transition. However, one should keep in mind that the properties of the state can change these estimates by many orders.

Table 2.1 displays the Weisskopf reduced estimates for transition probabilities and half-lives for the first three multipolarities in a nucleus with mass number A and γ-ray energy E_{γ}. From these transition probabilities, one can draw two immediate conclusions. First, the lower multipolarities are dominant; the difference in transition probability between adjacent multipoles is about 10^{-5}. Secondly, from observation, it was found that for a given multipole order, electric radiation is about

Table 2.1: Numerical values of Weisskopf estimates

Reduced single particle probability	γ-ray half life
$B(E1) = 0.064\ A^{2/3}\ e^2(fm)^2$	$T_{1/2} = 6.762\ A^{-2/3}\ E_\gamma^{-3}\times 10^{-15} sec$
$B(E2) = 0.059\ A^{4/3}\ e^2(fm)^4$	$T_{1/2} = 9.523\ A^{-4/3}\ E_\gamma^{-3}\times 10^{-9} sec$
$B(E3) = 0.059\ A^2\ e^2(fm)^6$	$T_{1/2} = 2.044\ A^{-2}\ E_\gamma^{-3}\times 10^{-2} sec$
$B(M1) = 1.790\ (e\hbar/2M_pc)^2$	$T_{1/2} = 2.202\ E_\gamma^{-3}\times 10^{-14} sec$
$B(M2) = 1.650\ A^{2/3}\ (e\hbar/2M_pc)^2(fm)^2$	$T_{1/2} = 3.100\ A^{-2/3}\ E_\gamma^{-3}\times 10^{-8} sec$
$B(M3) = 1.650\ A^{4/3}\ (e\hbar/2M_pc)^2(fm)^4$	$T_{1/2} = 6.655\ A^{-4/3}\ E_\gamma^{-3}\times 10^{-2} sec$

two orders of magnitude stronger than magnetic in medium and heavy nuclei. Hence, the most commonly observed radiations in γ-ray spectroscopy are those of magnetic dipoles, electric dipoles, and electric quadrupoles. The reader is advised to refer to Hamilton [32] for a more detailed discussion.

2.10 Alpha Decay Theory

Alpha decay is the process in which the parent nucleus decays into a daughter nucleus by emitting an α particle (which is basically a He atom). The daughter nucleus naturally has two protons and two neutrons less than the parent nucleus. Nuclear structure information can be obtained by measuring the spectroscopic properties of the emitted α particle due to its mono-energetic behavior. Symbolically, this process can be written as

$$Z^A \rightarrow (Z-2)^{A-4} + {}^4_2He, \tag{2.39}$$

where A and Z correspond to the parent's mass and proton numbers, respectively. Since this process is quantum mechanical, energy and linear momentum of the system are conserved. This leads to the definition of the α-decay Q-value shown below:

$$Q_\alpha = (M_A - M_{A-4} - M_{^4_2He})c^2 = T_{A-4} + T_\alpha, \tag{2.40}$$

where M_A, M_{a-4}, and $M_{^4_2He}$ are the masses of the parent, daughter, and helium atom, respectively. T_{A-4} is the kinetic energy of the daughter nucleus while T_α denotes the kinetic energy of the α particle. If the Q-value is greater than zero, then spontaneous α decay occurs. However, the rate of α emission does not become appreciable until the Q-value is in the MeV range.

Another property of the α-decay process is the α-decay constant (λ_α), which is defined as the probability per second that a nucleus will α decay. It is related to the half-life ($T_{1/2}$) as indicated here,

$$\lambda_\alpha = \frac{ln2}{T_{1/2\alpha}}. \tag{2.41}$$

Sometimes a nucleus may emit multiple α particles with different energies which populate different excited states in the daughter nucleus. Each decay from a particular state has a different decay constant, and this is known as the partial decay constant (λ_{α_i}).

In order to connect this partial decay constant to the total decay constant, a branching quantity is defined. This quantity is known as the α-decay branching ratio (b_{α_i}) and is defined as the ratio of the partial to the total decay constant and is given by the equations below,

$$b_{\alpha i} = \frac{\lambda_{\alpha i}}{\lambda}, \tag{2.42}$$

$$\lambda = \lambda_\alpha + \lambda_\beta + \lambda_{ic} + ..., \tag{2.43}$$

$$\lambda_\alpha = \sum_i \lambda_{\alpha_i}. \tag{2.44}$$

The terms λ_β and λ_{ic} correspond to the β-decay and interval-conversion-decay constants. From the investigation of the systematics of α decay of nuclei with $Z \geq 84$, an empirical formula of the transition rate (λ) was obtained.

It was observed that the transition rates of these α-decaying even-even nuclei when decaying to the ground states are smoothly varying as a function of charge and mass number of the nuclei. This empirical formula is known as the Gieger-Nuttal relation and a common way to express this relation is shown below,

$$log\lambda_\alpha(E_\alpha, Z) = -\frac{K_1(Z)}{\sqrt{E_\alpha}} + K_2(Z), \tag{2.45}$$

$$K_1 = 139.8 + 1.83(Z - 90) + 0.012(Z - 90)^2, \tag{2.46}$$

$$K_2 = 52.1 + 0.30(Z - 90) + 0.001(Z - 90)^2, \tag{2.47}$$

where λ_α and E_α are expressed in $\sec^{-1}$ and MeV, respectively. With the Gieger-Nuttal relation (Eq. 2.45), one can clearly see that the log value of half-life of the α decay is proportional to the square-root of its energy.

2.10.1 Alpha Emission

The α-decay process has been seen throughout the history of modern physics as a subject easily understood in principle, but difficult to interpret precisely. The α-decay rate depends on the tunneling probability through the Coulomb barrier as well as energies and angular momenta of the emitted particles, and configurations of the parent and daughter states. Alpha decays are likely to populate low lying states in daughter nuclei and can provide valuable information on the single-particle structure.

In 1928, a semi-classical theory of α decay was proposed whereby a pre-formed α particle could be described as "tunneling" through a barrier. However, with the discovery of the neutron, it was realized that α particles are made of constituent nucleons. This implied that many aspects of the α decay process needed to be resolved. These included how an α particle was formed in the nucleus and how it penetrates the barrier.

The emission of the α particle from the nucleus cannot be explained using classical mechanics. This fact is best illustrated using the schematic potential energy for ^{238}U, shown in Fig. 2.8. Starting with the formation of the alpha particle and daughter, it should be clear that from the decay process alone, the α particle should be trapped behind the barrier. However, reality says otherwise. The α particle does escape from the well.

The solution to this problem is quantum mechanical and that is to visualize a barrier which an α particle must tunnel through. The details of such calculations can be found in many quantum mechanics textbooks, however, some of the main features of this effect are discussed in a simple model. First, for simplicity, one assumes that the radius of the nucleonic matter is uniform, where $R = r_0 A^{1/3}$. The potential

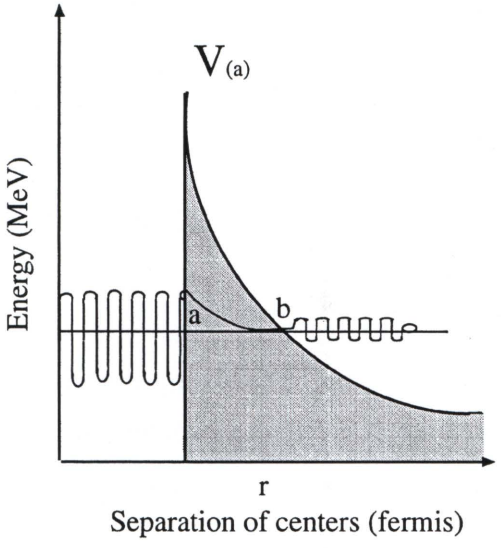

Figure 2.8: Tunneling model of α-particle emission.

outside the nuclear surface ($r > R$) is taken to be the Coulomb repulsive force,

$$V(r) = 2.88 Z r^{-1} MeV. \tag{2.48}$$

Inside the well, the α particle is assumed to interact with a square well potential. Using this approximation, the height of the barrier can be estimated from the work required to overcome the repulsive force.

The tunneling probability of the α particle through the barrier, i.e. transmission coefficient (T), can be obtained by solving the Schrödinger equation. The approximate T value is given by

$$T = e^{-2\pi\eta} = e^{-2\pi \frac{zZ\alpha c}{\sqrt{2E_\alpha / M_\alpha}}}, \tag{2.49}$$

where η is the Sommerfeld number. The terms Z, z, α, E_α, and M_α correspond to the parent's proton number, α-particle's proton number, fine-structure constant, α-particle's energy, and mass, respectively.

With the relation above, the transition probability can be written as $\lambda_\alpha = \nu P_\alpha T$. The terms $P_\alpha \sim 0.1$ and $\nu = 2.9 \times 10^{21} \times \frac{\sqrt{E_\alpha}}{A^{1/3}}$ (s) are defined as the probability

to find an α particle inside the nucleus and the frequency at which that α particle appears at the edge of the potential well, respectively. When written in a logarithm form, the equation above reduces to

$$log\lambda_\alpha = 20.46 + log\frac{\sqrt{E_\alpha}}{A^{1/3}} + 1.42\sqrt{ZA^{1/3}} - 1.72\frac{Z}{\sqrt{E_\alpha}}. \tag{2.50}$$

Hence, we get an equation which is in agreement with the empirical Gieger-Nuttal relation (Eq.2.45). The reader should refer to Ref. [33] for further detail.

2.10.2 One-Body Model and Reduced Width

In 1954 Winslow [34] introduced the theory of preformation factor and the "surface well potential". In this theory, it is assumed that an alpha particle exists for a short period of time (compared to the time of formation) and performs a one-body motion before it penetrates through a surface well potential.

In order to calculate the probability of α decay, the process has to be separated into two steps; the formation of an alpha particle in the nucleus from four nucleons and finally the penetration and escaping from the potential barrier. In 1959, Rasmussen [35] solved the one-body penetration probability by using a Woods-Saxon and Coulomb potential [36] with a method called WKB.

The second process, which involves the escape of the α particle from the barrier is described by the following equation,

$$\lambda = \frac{P\delta^2}{h}, \tag{2.51}$$

where λ and h is the decay and Plank constants, respectively. δ^2 is defined as the formation factor, and is better known as the reduced width. Using Eq. 2.51, experimentalists can extract the empirical nuclear effects of the formation factor δ^2, since the λ can be obtained from measuring the half-life while P can be calculated using the WKB method.

2.10.3 Alpha Selection Rules and Hindrance Factor

The emitted α particle has a spin of zero because all its protons and neutrons are paired. Hence the α-decay selection rules between parent and daughter nuclei are

very simple. The angular momentum of the α particle is constrained by the following equation

$$|(I_i - I_f)| \leq l \leq |(I_i + I_f)|, \tag{2.52}$$

where I_i and I_f are the spins of the initial and final states, respectively. Furthermore, the l value of the α particle is also restricted by the conservation of parity. The l is even if the initial and final states have the same parity and l is odd otherwise. A transition between the parent and daughter nuclei with $l = 0$ is known as an unhindered transition. Another important feature of the decay probability rate is that it changes exponentially with the decay energy. Thus, α decay can only be used to study low-lying states.

In order to characterize the nuclear structure properties of states that decay by α emission, it is important to obtain a quantity that is independent of the decay energy. The hindrance factor (F_α) is one such quantity. According to its definition, the hindrance factors of ground-state to ground-state decays of even-even nuclei are set to unity. The hindrance factor of an $l = 0$ α transition to an excited state in an even-even nucleus is equal to the ratio of the reduced-width of the ground-state transition over the reduced-width of the excited state transition. This can be written as

$$F_\alpha = \frac{(\delta^2_{00})_g}{(\delta^2_{00})_{ex}}, \tag{2.53}$$

while for odd-A mass nuclei, the hindrance factor for the α transition is given by

$$F_\alpha = \frac{(1/2)((\delta^2_{00})^A_g + (\delta^2_{00})^{A+2}_g)}{(\delta^2_{00})^{A+1}}. \tag{2.54}$$

In deformed odd-A nuclei, the α transitions are somewhat slower than for even-even nuclei. The decay from a parent to an excited state in a daughter nucleus will be slower if the process requires re-arrangement of more than two protons and two neutrons, i.e. some re-coupling of the remaining nucleons. When such processes happen, the resultant peaks are known as fine structure. The probability of the α decay will also be affected if the excited states have some admixture of the ground-state configuration.

CHAPTER 3

Experimental Techniques and the Recoil-Decay Tagging Method

3.1 Introduction

As we try to expand our knowledge of the nuclear chart toward the proton dripline, measurements of these neutron-deficient nuclei become more difficult since the cross-sections for populating these nuclei become extremely small. A typical approach to study nuclei near the proton dripline with extremely small cross-sections is to use a setup of highly sensitive γ-ray detectors which are coupled to a recoil mass separator. This method has been very successful; however, for some nuclei with $Z \geq 50$, identification of such nuclei is difficult because of weak selectivity and strong background from isobars (nuclei with the same atomic mass but different Z) which also have the same mass/charge (A/Q) ratio. Fortunately, an alternative method was developed to solve this problem. This is possible because many of the nuclei near the proton dripline and above $Z = 50$ decay via emitting α particles, protons, and β-delayed protons, which can be used to distinguish the nuclei produced.

Observations of such decay characteristics have made identification of their correlated isotopes produced in the nuclear reaction possible. This leads to the detection of a weak reaction channel when the radioactive decay detection method is combined with γ-ray spectroscopy. This coupled technique is known as the Recoil Decay Tagging (RDT) method [2, 3], first employed in the late eighties at GSI (Germany) and further developed at Daresbury Laboratory (U.K.). The RDT method is an extremely sensitive technique which combines mass separation and decay properties to identify specific weakly produced nuclear reaction products and to tag the prompt radiation emitted by these recoils.

3.2 Experimental Details

The data for this dissertation work was obtained from an experiment which was conducted at the Argonne National Laboratory (ANL) from December 7 to 20, 1999. Three different fusion-evaporation reactions (see below) were used to enhance the production of odd-A ^{173,175,177}Au nuclei.

- ^{92}Mo + ^{84}Sr $\rightarrow$ ^{176}Hg at beam energies of 390 and 395 MeV
- ^{94}Mo + ^{84}Sr $\rightarrow$ ^{178}Hg at beam energies of 380 and 385 MeV
- ^{96}Mo + ^{84}Sr $\rightarrow$ ^{180}Hg at beam energies of 380 and 385 MeV

From these reactions, more than twenty residual nuclei were produced (Fig. 3.1). The ^{84}Sr beam was delivered by the ATLAS superconducting linear accelerator. The targets were isotopically enriched ($\approx$ 98%) and had a thickness $\sim$ 0.7 mg/cm^2. Prompt γ rays were detected using 101 escape-suppressed Ge detectors of Gammasphere [40].

The recoiling evaporation residues were then passed through the Fragment Mass Analyzer (FMA) [41, 42, 43] and were dispersed according to their mass/charge (A/Q) ratio. A position-sensitive parallel-grid avalanche counter (PGAC), located at the focal plane of the FMA, was used to gather the time-of-flight and A/Q information of the recoiling nuclei. The recoils were implanted in a 40 mm $\times$ 40 mm, $\approx$ 60 μm thick double-sided silicon strip detector (DSSD) located approximately 40 cm behind the FMA. All in-beam and focal-plane signals were time stamped by a 47-bit, 1-MHz clock, such that γ rays observed at the target position could be correlated with the α decays detected in the DSSD. This method is known as the Recoil Decay Tagging (RDT) [2, 3] which allows us to correctly associate in-beam γ rays with a particular α-emitting nuclear ground-state or isomer.

In the off-line analysis, evaporation residues were separated from the background of high velocity scattered beam projectiles by using the time-of-flight information between the PGAC and the DSSD and the implantation energies. This enabled a cleaner determination of the mass of each recoil and reduced accidental correlations of decaying alphas with unrelated implants. An array of four Gammasphere-type Ge detectors and a single Low-Energy Photon Spectrometer (LEPS) surrounded the DSSD

Z \ N	92	93	94	95	96	97	98	99	100
80	^{172}Hg	^{173}Hg	^{174}Hg	^{175}Hg	^{176}Hg	^{177}Hg	^{178}Hg	^{179}Hg	^{180}Hg
79	^{171}Au	^{172}Au	^{173}Au	^{174}Au	^{175}Au	^{176}Au	^{177}Au	^{178}Au	^{179}Au
78	^{170}Pt	^{171}Pt	^{172}Pt	^{173}Pt	^{174}Pt	^{175}Pt	^{176}Pt	^{177}Pt	^{178}Pt
77	^{169}Ir	^{170}Ir	^{171}Ir	^{172}Ir	^{173}Ir	^{174}Ir	^{175}Ir	^{176}Ir	^{177}Ir
76	^{168}Os	^{169}Os	^{170}Os	^{171}Os	^{172}Os	^{173}Os	^{174}Os	^{175}Os	^{176}Os
75	^{167}Re	^{168}Re	^{169}Re	^{170}Re	^{171}Re	^{172}Re	^{173}Re	^{174}Re	^{175}Re

Figure 3.1: Map of the observed and possible populated nuclei following particle evaporation from the ^{176,178,180}Hg (purple boxes) compound nuclei. The nuclei in the yellow boxes indicate the observation of new α-decay lines and γ-ray transitions.

for measurenment of γ rays in coincidence with alphas from the implants and their daughters. This information was used to identify the excited states of the daughter and granddaughter nuclei fed by the α-decay fine-structure lines.

During the 14 days of experimental runs, the Gammasphere array detected more than 25 million γ-ray events associated with residues while the DSSD recorded approximately five million α particles. An approximately 2.8 million prompt γ-ray events are correlated with recoils that produced α particles within 10 s of the implantation. Only 16,000 γ-ray events were detected at the focal plane of the FMA. These are the γ rays that follow the emissions of α particles and are associated with excited states in daughter nuclei.

3.3 Recoil Decay Tagging Method

In an experiment utilizing the RDT technique, nuclei of interest are produced via the fusion-evaporation reactions (sec. 3.4) where a beam of ions, accelerated above the Coulomb barrier, is used to bombard a thin target foil. Surrounding the target position is an array of germanium detectors use to detect prompt γ rays emitted by the recoiling nuclei. The recoils are then separated by a recoil mass separator from the primary beam and the fission products, and dispressed in their mass over charge ratios. The recoiling nuclei are implanted into a position-sensitive double-sided silicon strip detector (DSSD) at the focal plane of the recoil mass separator. This detector records time, energy, and position information of specific implants, allowing for correlations between recoiling implants and their emitted decay particles.

All the events occurring at the target position, in the focal plane detector, and finally at the DSSD are time stamped. Consequently, after the arrival of each implanted recoil, its subsequent decay can be followed until the next implantation occurs in the same pixel of the DSSD. This method employs two types of data acquisition. First, all decay and implantation events, including the time at which the events occurred, were written to tapes. The other acquisition involved prompt γ ray events detected in coincidence (50 ns) at the target position where these events were written together with the events occurring at the DSSD. This allows the α or proton

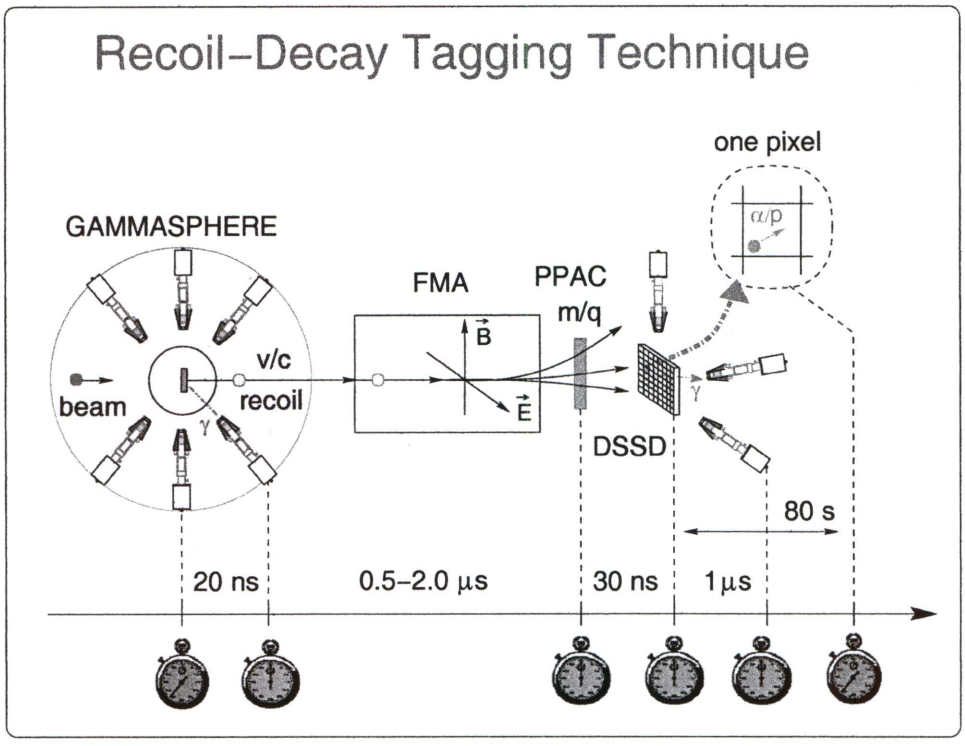

Figure 3.2: Schematic illustration of the RDT process. Obtained from Ref. [39].

decaying recoils detected at the DSSD to be correlated with prompt γ rays emitted at the target position. In addition to the α-γ coincidence, measurements of the decay energy and half-life are also possible. Fig. 3.2 illustrates the RDT technique.

3.4 Heavy-Ion Fusion Evaporation Reactions

The fusion-evaporation reaction is a powerful tool used to study high-spin states of neutron deficient nuclei. This technique when used with heavy-ion beams can create nuclei with large excitation energies and angular momenta. A compound nucleus is created when an accelerated heavy-ion projectile is fused with the target nucleus. The compound nucleus is unstable and decays by emitting particles and later, γ rays. It is the characteristics of the emitted γ rays that helps define the properties of the nucleus. Furthermore, this reaction can also provide the means to observe some of the unstable nuclei far from the valley of stability which cannot be produced by other

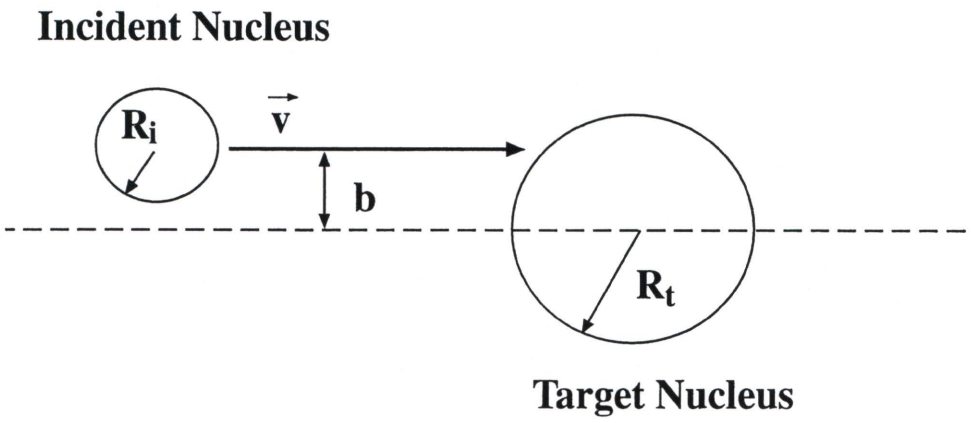

Figure 3.3: Schematic drawing of an incident nucleus impacting a target nucleus.

methods. The study of very heavy nuclei where fission is the dominant mode have also been made possible with this method.

In order to initialize fusion between the beam and target, the beam energy has to be large enough to overcome the Coulomb repulsion of the nucleus. The Coulomb potential in the center of mass system is given by

$$V_{CB}(R) = 1.44 \frac{Z_i Z_t}{R} \text{ MeV}, \tag{3.55}$$

where Z_i and Z_t are the number of protons in the beam and target nuclei, respectively. $R = R_i + R_t$ is defined as the Coulomb radius (in fm). The Coulomb radius can be determined from the relation between Eqn. 3.55 and the measured reaction cross section (σ_R) where

$$\sigma_R = \pi R^2 [\frac{1 - V_{CB}(R)}{E_{cm}}] \text{ MeV}. \tag{3.56}$$

Fig. 3.3 illustrates an accelerated nucleus on a collision path with a target nucleus. From a semi-classical perspective, the angular momentum of the projectile can be associated with its linear momentum (mv) and the impact parameter (b), where $l = mvb$. A complete fusion can only occur for a certain range of b values. If the impact parameter is too large then Coulomb scattering may occur. If there is some geometrical overlap between the nuclear matter of the projectile and the target, then inelastic nuclear scattering reactions can occur. Only with a complete overlap between the target and the projectile can a compound nucleus be formed, in which

case the fusion of beam and target nucleus has occurred.

In complete fusion, the nucleons in the compound nucleus reach thermal equilibrium and subsequent de-excitation is independent of the reaction mechanism. Once thermal equilibrium is reached, the compound nucleus becomes highly excited and has a very large angular momentum. The excitation energy of the resulting compound nucleus is given in Eq. 3.57:

$$E_{ex}^{max} = E_{CM} + Q, \tag{3.57}$$

$$where\ Q = (M_i + M_T - M_c)c^2,\ and \tag{3.58}$$

$$E_{CM} = \frac{M_i}{M_i + M_T} E_i. \tag{3.59}$$

E_{CM} is the center of mass energy of the system, and subscripts i, t, and c denote the incident, target, and compound nucleus, respectively. All the mass and energy units are given in MeV. In order to study the physics of highspins, the selection of the beam and the target characteristics are most important. This type of study requires inducing a large amount of angular momentum into the compound nuclear system, while still having a significant cross section. Since most of the angular momentum of the nucleonic system originates from the beam, selecting the beam of the heaviest nucleus with the most energy would likely produce the isotopes, with the desired high angular momentum.

In fact, the maximum angular momentum in a fusion reaction can be estimated using Eqn. 3.60, obtained from the sharp cut-off model, shown in Ref. [37]:

$$\ell_{max}(\hbar) \approx 0.219\ R_{fus}\ [\mu(E_{CM} - E_{CB})]^{1/2}, \tag{3.60}$$

where R_{fus} is an empirically derived radius of fusion,

$$R_{fus} = 0.95\ (M_i^{1/3} + M_T^{1/3})\ [\text{fm}]. \tag{3.61}$$

$\mu = \frac{M_i M_T}{M_i + M_T}$ [amu] is the reduced atomic mass, E_{CB} is the Coulomb barrier energy defined by Eqn. 3.55 and E_{CM} is the center of mass energy obtained from Eqn. 3.59.

3.4.1 Formation and Decay of Compound Nuclei

The creation and decay of a compound nucleus occurs in several stages. In order to create compound nuclei, the beam of projectiles is accelerated to an energy that is greater than the Coulomb barrier between projectile and target. Fusion between projectile and target takes place in $\approx 10^{-22}$ seconds to form a highly excited, rapidly spinning compound nucleus, assuming that the intermediate system survives fast fission.

The recently formed compound nucleus with a large amount of angular momentum and energy is unstable and after a relatively short period of time ($\sim 10^{-19}$ seconds), it decays by particle emissions. This process helps the compound nucleus to get rid of excess energy, at least equivalent to the particle's separation energy of 8 - 10 MeV. However, the emitted particles carry only a small faction ($\sim 1\hbar$) of the angular momentum of the system. Although the emission of protons, neutrons, and α particles are possible reaction channels, the Coulomb barrier at $A = 170$ region is sufficiently strong to greatly reduce emissions of charged particles. Therefore, the dominant decay process of the compound nucleus tends to be neutron evaporation. The emitted neutron removes a significant amount of energy ($\sim$ 1-2 MeV plus the binding energy of the neutron) from the nuclear system but carries only $\sim 1.5\hbar$ of angular momentum. For a neutron-deficient compound nucleus far from the β stability region, the separation energy tends to increase. The neutron separation energy is roughly equal to the proton binding energy *plus* its Coulomb barrier [38]. When the number of neutrons is approximately 15% less than those near β stability, the neutron and proton evaporation rates are comparable.

The emission of particles from the compound nucleus continues for about 10^{-15} seconds. Around this time, γ-ray emissions begin to compete with particle emissions. This process continues until the nucleus reaches an energy approximately less than the binding energy of one neutron above the yrast line. At this point, the nucleus begins to "cool" through the emission of statistical γ rays. This region exhibits an extremely high density of states which results in γ rays that are largely electric dipole in nature. Therefore, only a continuum of γ rays is observed. The level

density decreases as the nucleus cools when the excitation approaches ~3 MeV of the yrast line. Stretched quadrupole transitions begin to dominate and de-excite the nucleus through various collective structures. Both energy and angular momentum are dissipated as the nucleus decays through these rotational bands. In this region ("quasi-continuum"), it is impossible to resolve well defined structures because of the high concentration of bands.

The final stage of de-excitation occurs at about 10^{-12} seconds, when the nucleus approaches the ground state through discrete bands whose transitions can be cleanly detected. The final process can be constructed into a level scheme by using coincidence techniques ($\gamma - \gamma$ matrices or $\gamma - \gamma - \gamma$ cubes). The study of the level scheme constructed from the discrete lines is important for understanding the high-spin physics of the nucleus. The reader should refer to Fig. 3.4 where the various stages of decay of a compound nucleus are shown.

3.5 Experimental Devices

3.5.1 Compton-Suppression Spectrometer

For the last 25 years, high purity germanium (Ge) detectors have been used extensively to study the physics of high-spins in nuclei. These detectors are found in a number of large-volume γ-ray spectrometers around the world. These detectors, which have large volumes for a given surface area, are very efficient in detecting γ rays at a wide energy range (50 keV to 10 MeV). However, Ge detectors have some drawbacks.

Large-volume Ge detectors have poor resolution of Doppler-shifted γ rays emitted from recoils because they have a large angular acceptance. One technique being employed at Gammasphere (an array consisting of 110 Ge detectors and also sec. 3.5.3) in order to lower the size of the angular acceptance without reducing efficiency, is to electronically segment some of the detectors into two D-shaped halves. In this setup, the high-resolution, total-energy signal is read from the common electrode located at the center of the detector while the lower resolution signal is obtained

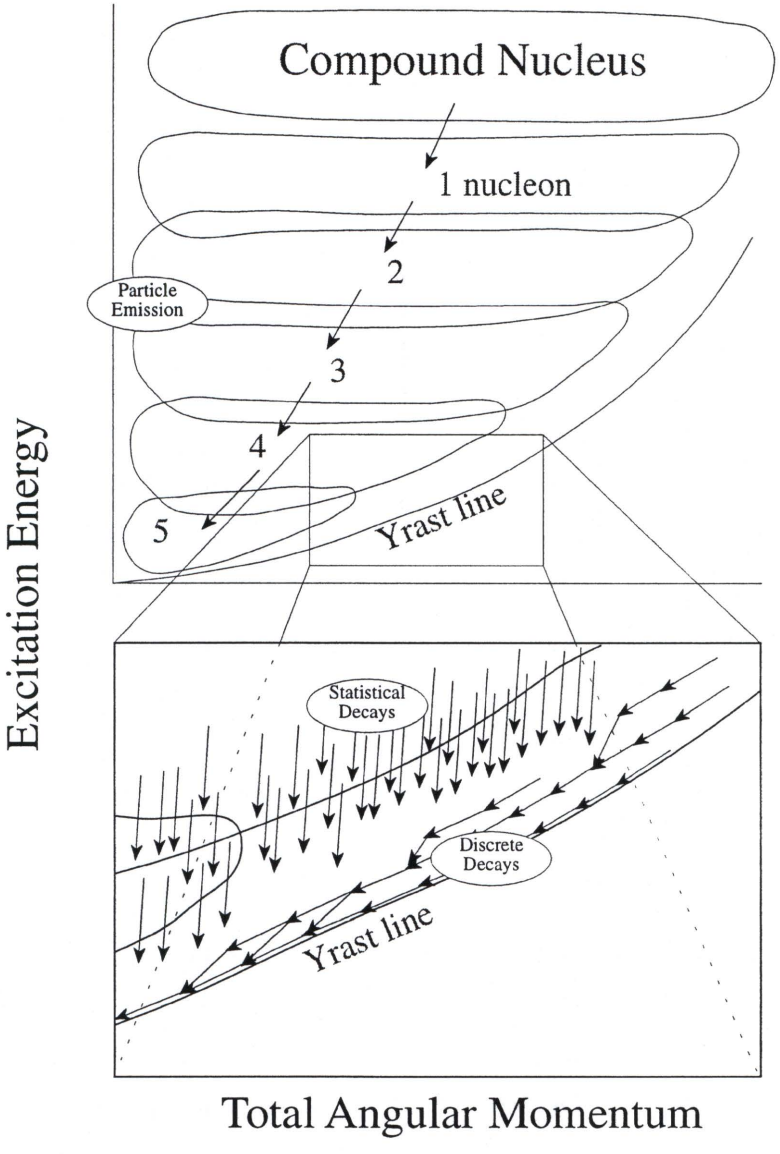

Figure 3.4: Illustration of angular momentum versus energy for the decay of a compound nucleus. Reproduced from Ref. [15].

separately from each side, hence indicating which side was hit first. This results in the reduced effective angular size of the Ge detector by a factor of two, thus doubling the resolving power of Gammasphere.

When a γ ray enters a Ge crystal, one of three processes (photoelectric effect, Compton scattering, or pair production) can happen. A photoelectric effect occurs when the γ ray in the Ge crystal is absorbed by an atomic electron which subsequently causes the electron to be ejected from the atom with a total energy equal to the γ-ray energy. On slowing down, this electron produces many electron-hole pairs in the Ge detector. The number is proportional to the initial energy of the electron. These electrons and holes are swept to opposite contacts where a charge, which is proportional to the γ-ray energy, can be measured. This process occurs dominantly at low energy (less than 150 keV).

The second process is Compton scattering which occurs when a photon is scattered by a free electron. In this case, the free electron will not absorb all of the photon energy due to the requirement of conservation of momentum. If the scattered photon escapes from the detector, then the total energy is not deposited. If the scattered photons are photo-absorbed by other bound electrons immediately after scattering, then the resulting charge is measured and the total photon energy is detected. The probabilities of a photon being photo-absorbed and Compton scattered are roughly dependent on Z^5 and Z, where Z is the proton number of a given material. This would imply that material with high Z is preferred for detecting γ rays. Compton scattering and photo-absorption processes are the dominant interactions between photons and crystal material for photon energy up to $\sim$ 2 MeV.

Finally, there is a possibility for photons with energies greater than 1022 keV to be converted in the vicinity of an atomic nucleus into a position-electron pair. Since the resulting positron eventually annihilates into two 511-keV γ rays, this process produces a full-energy peak as well as an escape peak that can be seen at 511 keV and 1022 keV below the photo-peak.

The most important aspect of the experimental data is the peak-to-total (P/T) ratio. Hence, the Compton Suppression Spectrometer (CSS) was created in order to greatly reduce the background caused by Compton scattering. CSS basically

consists of a Ge detector surrounded axially by another detector known as BGO. This BGO detector is made from a compound material called bismuth germanate ($Bi_4Ge_3O_{12}$). Bismuth germanate is widely used as shielding material due its high density ($\sim$ 7.1 g/cm^3).

The purpose of the BGO shield is to detect energetic γ rays which scatter out of the Ge crystal. When the BGO registers a γ ray signal, a simultaneous event which is recorded in the Ge detector is electronically deleted, hence the Compton continuum is reduced, and consequently the Compton continuum can be reduced and the P/T ratio increased. The P/T ratio is defined as the counts of the full energy peaks over the total counts in a given spectrum. The P/T ratio can give a rough measure of the performance of the CSS detector. To prevent the γ rays from the target from interacting directly with the BGO, a lead mask is put in front of the shield. The most important aspect in a γ-γ coincidence experiment is to achieve the highest possible P/T ratio. For example, a Ge detector with Compton shielding used in Gammasphere can achieve a P/T value of $\sim$ 0.7 for γ rays from a ^{60}Co source.

Compton-Suppression Electronics

In the early years of high-spin spectroscopy research involving a few germanium detectors, high-spin states in the rare earth region were observed up to around spin 30. At that time, the basic concept in γ-γ coincidence technique was to convert analog signals from the detectors into logic signals sent to a coincidence module. In the coincidence module, all pulses arriving within a time equal to the sum of their width were recorded as coincident pulses. Fig. 3.5 illustrates this point. Eventhough using those primitive detectors gave good experimental results, those detectors had one major problem, namely poor peak-to-background ratio.

For a Compton-suppression detector (shown in Fig. 3.6 and discussed in sec. 3.5.1) was developed. The detector will generate two identical signals E1 and E2 if the incoming γ ray is totally absorbed in the Ge crystal while the T signal is generated if the BGO completely absorbed the γ ray. Three signals, E1, E2, and T are created when the γ ray scatters between the two detector materials. The circuit

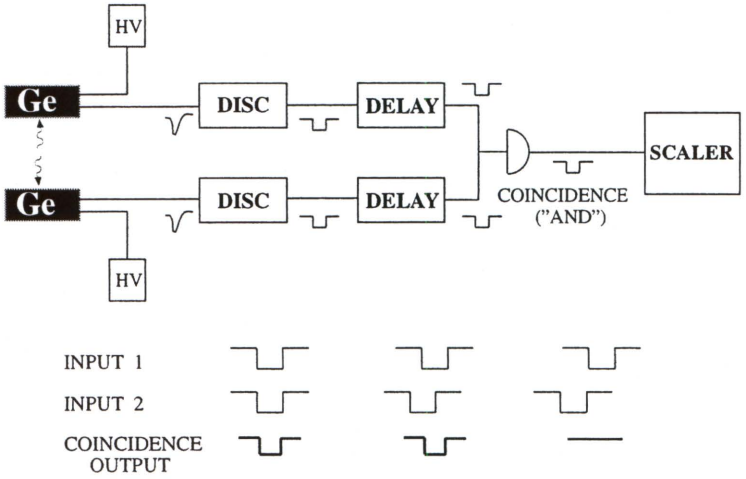

Figure 3.5: A simple coincidence circuit for two non-suppressed Ge detectors. Reproduced from Ref. [15].

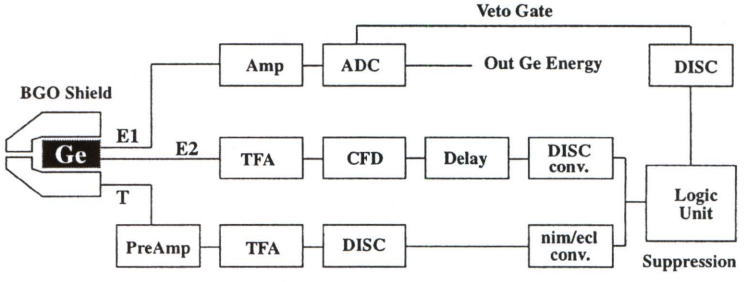

Figure 3.6: The schematics of a typical Compton-suppression setup. It is of a single Ge detector with BGO shield. Reproduced from Ref. [15].

shown in Fig. 3.6 works by recording the timing and energy of a "good" event, i.e. γ ray that is totally absorbed in the Ge crystal and rejects others.

Coincidence Concept

In a typical high-spin experment, ten of millions of γ rays are emitted. Charged-particle detectors, recoil separators, and the RDT technique have been used extensively in order to sort out γ rays that are associated with nuclei of interest. To observe cascades of γ rays from the highly excited states, it is important to observe time coincidence relations between different γ rays of a specific nucleus rather than just a "singles" γ-ray spectrum.

This has lead to the development of the coincidence technique between two or more γ rays, which greatly reduces the background in γ-ray spectra which is due to random uncorrelated events. The coincidence concept is illustrated in Fig. 3.7 for three different γ rays. It is assumed that all the levels in the figure have half-lives shorter than the coincidence gate used for the detectors in coincidence. By setting a "time" window (t_w) greater than τ, the coincidence between γ_1 and γ_2 will be detected by the two detectors. Observation of γ_3 and γ_2 in coincidence could only occur by random coincidence since γ_3 and γ_2 cannot both result from the decay of a single nucleus. By setting a small "time window" ($t_w \sim$ 50 ns), random coincidences between γ_3 and γ_2 are minimized.

3.5.2 Low-Energy Photon Spectrometers

A Low-Energy Photon Spectrometer (LEPS) is used to detect low energy γ and x rays (up to 300 keV). The planar shaped LEPS has a relatively small volume when compared to the surface area facing the reaction. Because of the excellent timing resolution, LEPS detectors are irreplaceable in detecting low energy photons. This is due to the small capacitance of the detector. When the detector is fully depleted and operates with a large over-voltage, a near uniform electric field can be achieved in the detectors from one contact to another. This results in a very fast collection time for charge carriers and comparatively large signal to noise ratio. Even though LEPS has better energy and time resolutions than a coaxial Ge detector, the efficiency for detection of γ rays with energies greater than 400 keV is very low. This is due to their small sensitive volume which generally fails to absorb high-energy γ rays as they pass through.

3.5.3 Gammasphere Array

All the in-beam γ-ray data in dissertation was acquired using the Gammasphere array at ANL. Gammasphere is a spectrometer extremely sensitive to the presence of nuclear electromagnetic radiation due its efficiency, high resolution, and granularity. It is the combination of these features that makes Gammasphere an ideal tool to study nuclear

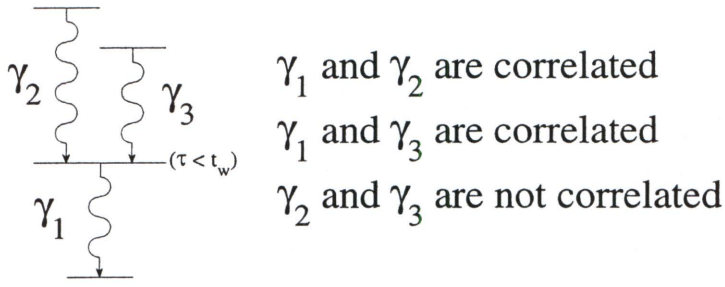

Figure 3.7: Schematic decay scheme illustrating correlated γ decays. Reproduced from Ref. [15].

physics of rare and exotic processes. Currently, Gammasphere is used to study nuclei at the very limits of nuclear stability due to their high angular momentum, high mass, unusual proton to neutron ratio, and internal excitation.

The Gammasphere consists of a spherical shell with up to 110 Compton-suppressed high-purity germanium detectors. The spherical shell has a diameter of 1.46 m and is divided into two hemispheres and a total Ge detector coverage of 46%. With respect to the beam axis, these detectors are mounted at the following angles (with a forward-backward symmetry): 10 detectors at 17.3°, 10 at 31.7°, 10 at 37.4°, 20 at 50.1°, 10 at 58.3°, 20 at 69.8°, 10 at 79.2°, 10 at 80.7°, and 10 at 90°. Gammasphere, with all its 110 Ge detectors mounted, has a peak to total ratio of approximately 60% and a total photopeak efficiency of 9.9% for a 1.33-MeV γ ray. A summary of the characteristic parameters for Gammasphere is shown in Table 3.1. The two hemispheres are supported mechanically such that one can easily mount and dismount the detectors. This structure can be moved transversely from and rotated along the axis that is perpendicular to the beam line.

A creative data collection system was implemented in order to handle the immense amount of data coming from the Gammasphere array. This includes signals from preamplifiers, high voltage supplies, and temperature control devices all of which are mounted on the Compton-suppressed germanium detectors. These devices are interfaced with nearby VXI crates in order to have complete signal processing, to control which gating conditions are used to obtain Compton suppression, to record coincidence events, and to monitor detector units. This system is remotely controlled

Table 3.1: Properties of Gammasphere. Reproduced from [15].

Number of Detectors	110 hexagonal units w/BGO
	40 unsegmented
	70 segmented
Ge Detector size	7.1 cm (D) × 8 cm (L)
Target to Ge distance	25.25 cm
Total Ge solid angle	46% of 4π
Total peak efficiency (1.33 MeV)	9.9%
P/T (1.33 MeV)	0.6
Energy resolution (1.33 MeV)	2.5 keV (FWHM)

by external computers and all the data obtained are stored on 8 mm tapes with a maximum writing rate of 40 Mbytes/sec. A photograph displaying the Gammasphere array is shown in Fig. 3.8. In a typical high-spin experiment, using a fusion-evaporation reaction to produce rare-earth nuclei, with several pnA of beam current, one can expect a reaction rate of the order of 10^5 per second. A three-day experiment thus produces $N_R \sim 3{\times}10^{10}$ reactions with a typical γ-ray multiplicity of $M_\gamma \sim 25$. Gammasphere has an efficiency of $\epsilon \sim 0.15$, resulting in $\approx 1.6 \times 10^{10}$ four-fold or higher events, which can be histogrammed in a three-dimensional cube (sec. 3.6).

3.5.4 Fragment Mass Analyzer

The Fragment Mass Analyzer (FMA) is an isochronous mass-dispersing energy focusing recoil mass spectrometer. It is used in heavy-ion reactions to separate nuclear products from the primary beam and then disperse them according to their mass/charge (A/Q) ratio. The FMA when combined with the Gammasphere array can be a powerful tool to study the physics of nuclei whose production cross-sections fall below 0.01 % of the fusion cross-section.

The FMA is 8.2 m long and consists of two electric dipoles and a magnetic dipole set in a chromatically symmetric combination (Fig. 3.9). The electric dipoles

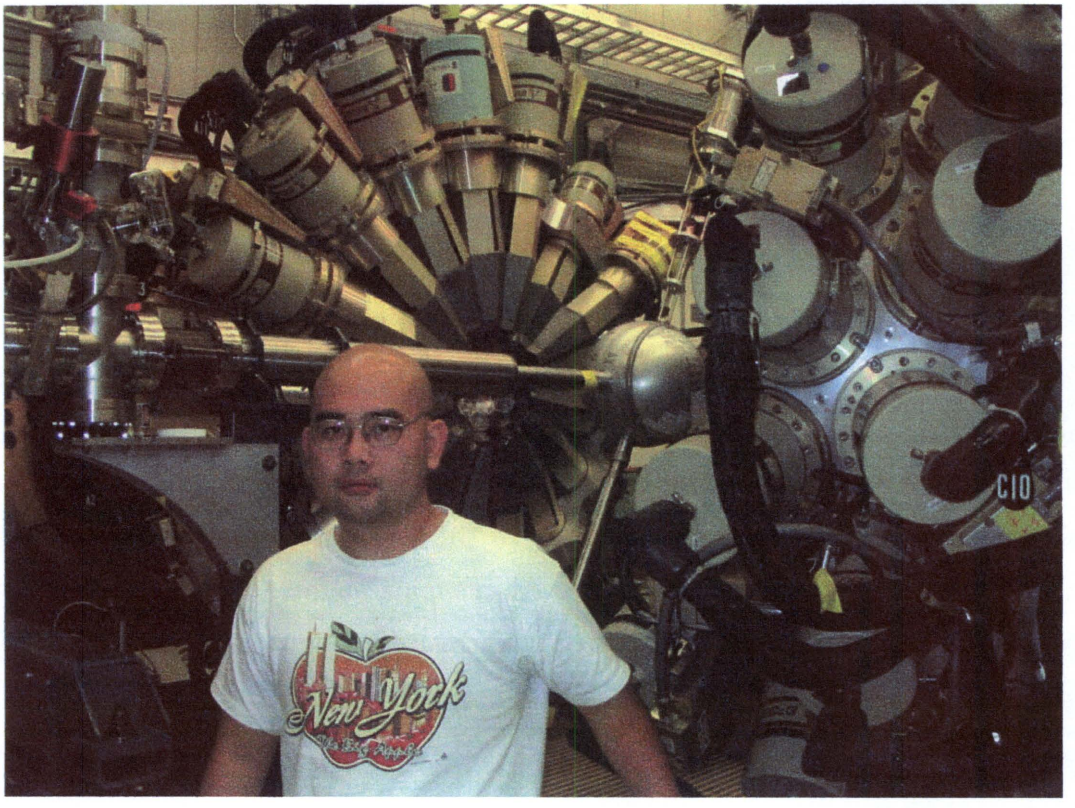

Figure 3.8: Gammasphere array with its 102 Compton-suppression Ge detectors.

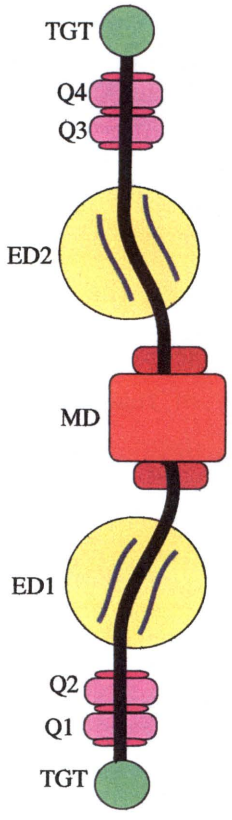

Figure 3.9: A schematic view of the ATLAS Fragment Mass Analyzer. The beam enters the target shown at the top of the figure. The recoils are dispersed according to their charge-to-mass ratio A/Q at the focal plane. The device consists of two electric dipoles (E1 and E2), a magnetic dipole (MD), four magnetic quadrupoles (Q1-Q4), and two magnetic sextuploes (TGT).

have a curvature radius of 4 m while the magnetic dipole has curvature radius of 1 m. The FMA has a mass resolution of $A/(\Delta A) > 300$ FWHM and a solid angle of 8 msr. Furthermore, it has acceptances of $\pm$ 20% in recoil ion energy and $\pm$ 7% of A/Q around the central mass.

One of the most useful features of the FMA is its small time scale operation after the creation of recoils at the target position. The time scale is determined by measuring the time-of-flight of the recoils from the target position to the focal plane against the RF beam structure and it is on the order of 1 μs. It is the measurement of the time-of-flight of the recoils that removes the ambiguities of the A/Q and makes

the FMA a true mass determining device. The small time scale of the FMA also permits prompt γ-rays emitted at the Gammasphere to be correlated with the decay of the nuclei occurring at the focal plane within a few μs. Furthermore, with these timing advantages, the FMA can also permit the study of short-lived isomers. The masses of these isomers can be determined quite accurately if they lives at least 1 μs which is the time of travel through the FMA. Other classes of experiment that can be made possible using the FMA are the measurement of nuclear moments using radioactive beams and the study of reaction mechanisms, i.e. incomplete fusion, sub-barrier fusion, and resonances in quasi-elastic scattering.

3.5.5 The Parallel Grid Avalanche Counter

The Parallel Grid Avalanche Counter (PGAC) is a standard focal plane detector housed in a chamber which is located at the focal plane of the FMA. This multi-wired proportional counter is used to provide x-, y-postion, time, and energy lost information on particles reaching the FMA focal plane. It has a 15 x 5 cm active area and contains four wire planes; cathode-, x-, anode-, and y-plane at 3.2 mm distance apart. The chamber is constantly circulated with isobutane gas at a pressure of 3 torr.

Charges are formed on the x-plane and y-plane when ions pass through the chamber. Spatial information is derived from the time delays of the x and y signals. This information is obtained from the ends of the x- (right, left) and y-plane (up, down) wires. The signals from the anode and cathode are used to identify recoiling events.

3.5.6 The Double-Sided Strip Silicon Detectors

The Double-Sided Silicon Strip Detector (DSSD) (Fig. 3.10), which is a "pixelation" silicon detector, is used for implantation and decay studies. It is located at a distance approximately 40 cm behind the PGAC. The 60 μm thick DSSD used in this experiment consists of 40 cm horizontal and 40 cm vertical strips (40 x 40 cm). This arrangement resulted in a total of 1600 pixels for the DSSD where each pixel acts as

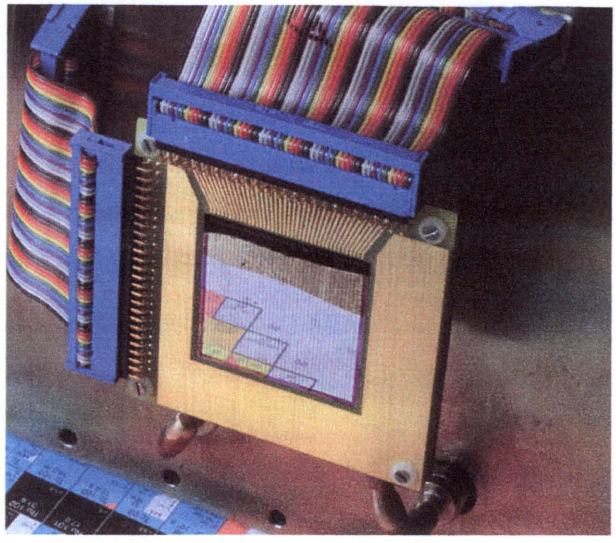

Figure 3.10: View of a typical 40×40 mm double-sided silicon strip detectors.

a separate detector.

A setup of combined DSSD and PGAC enables a decay detected at the DSSD to be associated with a particular recoil observed in coincidence in the PGAC. Because most α particle lifetimes are often several milliseconds to seconds, a time coincidence between the PGAC and α decay is impossible. Instead, a position coincidence is recorded. From observation, it was found that nearly 100% of the recoils passing through the PGAC will be implanted at the DSSD. Therefore, a time coincidence between PGAC and implantation at the DSSD can be observed. If the lifetime of the implant is small compared to the average time between implants, then the decay can be correlated with the recoil of interest. Accidental correlations can also occur if the average time between implants is not so large when compared to the decay time.

All the events in the DSSD are time stamped, where correlated implantation events and energy are recorded. When an implant is detected and subsequently the recoil decays in the DSSD, two times (t_0 and t_1) are recorded for the implant and decay signals. The half-lives of the specific recoils observed in-beam can be determined from t_0 and t_1. The decay pulse signal from the DSSD is proportional to the α decay energy. External α sources and online production of known particle activities are used to gain-match individual strips and calibrate the energy spectra.

3.6 Offline Data Analysis

The purpose of off-line analysis is to build a level scheme in order to interpret α-decay and γ-ray structures in the nucleus of interest. In this section, the analysis process and the off-line tools used are introduced. The first step is to scan the 8-mm data tapes, followed by energy and efficiency calibration of the Ge detectors and the building of coincidence cubes and matrices. This procedure requires software packages and a scanning routine which will be discussed briefly.

3.6.1 FMA and RDT Analysis

The combination of the recoil mass separator like the FMA with a large array detector such as the Gammasphere along with the RDT technique makes the study of nuclei with extremely small cross-sections (approximately less than 0.01% of the fusion cross-section) possible. Since each event detected in the Gammasphere, the FMA, and the DSSD is time-stamped, it is possible to select a particular mass channel and study its correlated γ rays and α particles.

The compressed data tapes are scanned so that a 2-dimensional histogram of mass-channel events versus their correlated in-beam γ rays or α particles can be constructed. By "taking gates" on a particular mass channel, we can select the α and γ transitions emitted by the nuclei of interest. This is illustrated in Fig. 3.11 where in part (a) all γ rays associated with the α-decaying nuclei which were produced in the ^{84}Sr + ^{92}Mo $\rightarrow$ ^{176}Hg reaction are displayed. The resulting mass spectrum is displayed in part (b) and those γ rays asssociated with mass 174 gates indicated in part (b) are shown in part (c).

3.6.2 Efficiency and Energy Calibration of Ge Detectors

Generally it is expected that a linear relationship between energy deposition and the generated signal is maintained in the Ge detectors. However, calibrating such devices is required in order to determine this linear relationship for each detector, each with unique characteristics and electronic setups. The electronics of the analog to digital converter (ADC) are designed to produce a linear output such that $E = A + Bx$,

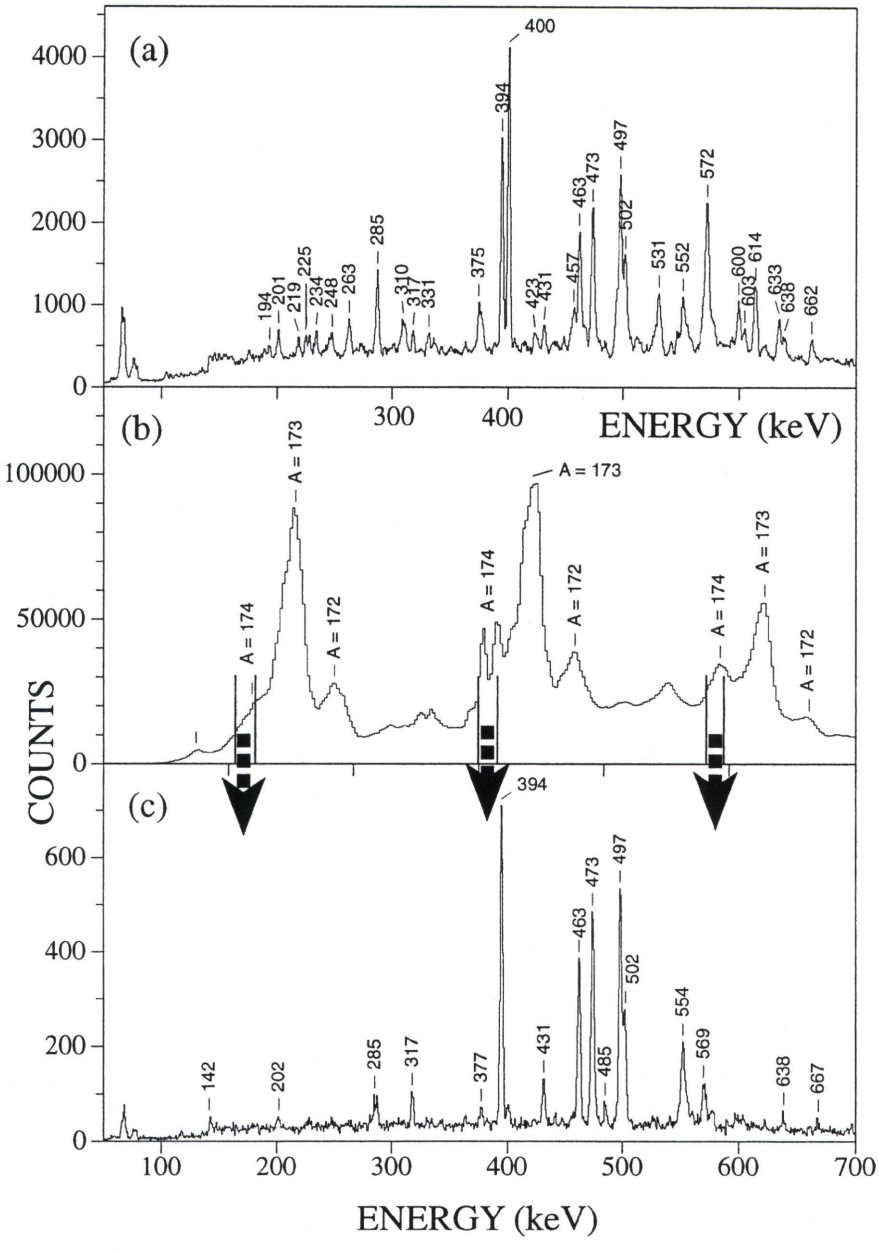

Figure 3.11: Schematic illustration of mass-gating γ-ray spectrum. Part (a), (b), and (c) correspond to all γ rays that are correlated with α-decaying nuclei, the mass spectrum, and γ rays in coincidence with $A = 174$ recoils, respectively. The arrows show the portion of the mass spectrum used to produce the $A = 174$ γ spectrum in part (c). All these spectra are produced via the ^{84}Sr + ^{92}Mo $\rightarrow$ ^{176}Hg reaction.

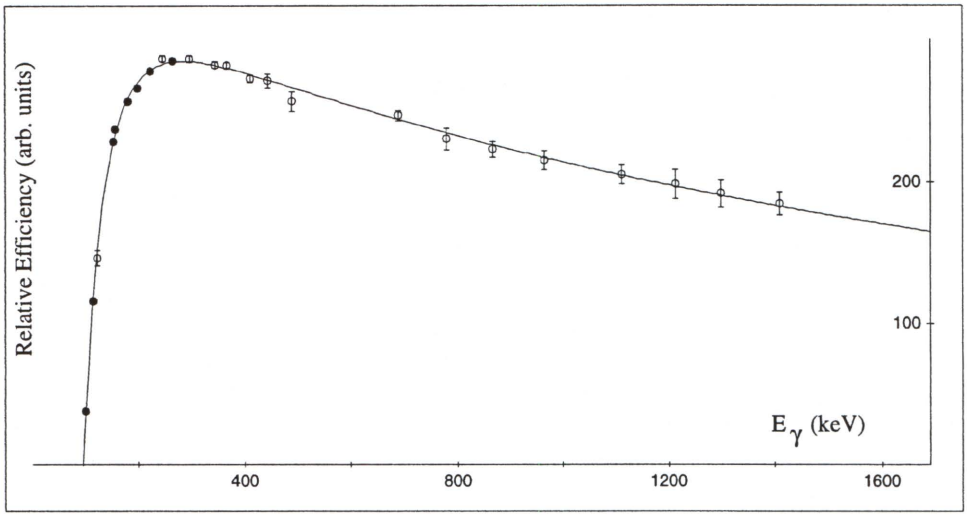

Figure 3.12: Gammasphere detector efficiency calibration curve. The filled-circle (^{182}Ta) and open-circle (^{152}Eu) data points are generated from all Ge detectors of Gammasphere when the sources are applied to them. This figure also displays the efficiency function $\varepsilon(E_\gamma)$, fit to the data. Reproduced from Ref. [15].

where E and x are the γ-ray energy and channel number, respectively. In many instances, the calibration spectra of the standard ^{152}Eu and ^{182}Ta sources are used to determine the A and B constants.

The ability of the Ge detectors to fully absorb γ rays also varies nonlinearly with the γ-ray energy. Utilizing the universally accepted intensities of γ transitions in ^{152}Eu and ^{182}Ta, a relative efficiency curve, shown in Fig. 3.12, can be created. For relative normalization, peaks with similar energies from both sources are normalized to the same relative intensity. Fig. 3.13 displays the spectra from both sources using all Gammasphere detectors in the setup of the ANL experiment.

3.6.3 Level Scheme Construction

As mentioned earlier, all the data obtained from our experiment was written to tapes. The written data were scanned and sorted into histograms, using a sorting routine package called *RDT-SORT*85. This sorting program was developed at Argonne National Laboratory. In this package, there are input subroutine programs which cor-

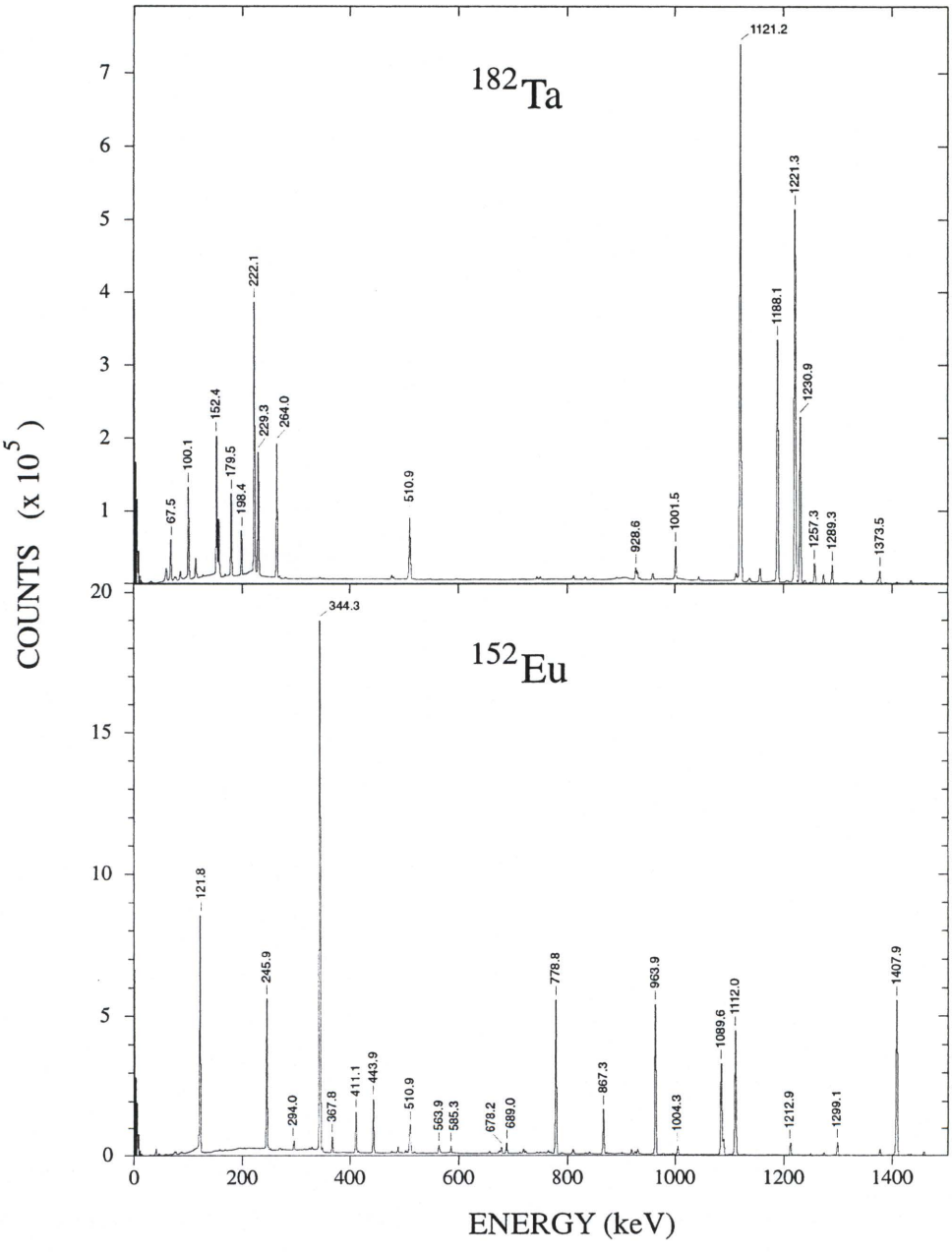

Figure 3.13: Calibration spectra of ^{152}Eu and ^{182}Ta. Spectra displayed are the sum of all Gammasphere Ge detectors singles spectra. The 511-keV γ-ray peak, observed in both spectra, is due the electron-positron annihilation.

relate histograms with specific masses and α particles. Histograms are created in order to analyze prompt γ-decay cascades, α-α, and α-γ coincidences. For γ-ray coincidences, the histogram is a two-dimensional spectrum (matrix) of sorted $\gamma - \gamma$ events.

In a prompt γ-decay experiment, when detectors in the Gammasphere array simultaneously observed two γ rays, γ_1 and γ_2, in a given event, then two histogram cells are incremented in the following way: (row, column) = (γ_1, γ_2) and (row, column) = (γ_2, γ_1). This results in a symmetrical E_γ-E_γ matrix. When data are collected using a large detector array, such as Gammasphere, three and higher-fold Ge coincidences are common. This makes possible the creation of a cube (3-D histogram) which stores the information of γ-γ-γ correlated events.

It is also possible to associate a particular mass of the recoiling nucleus via the FMA mass channels with the emitted γ rays detected at the target position. In this case, all γ-ray events which were sorted into a matrix/cube are essentially correlated with a selected mass channel of a particular nucleus. Such matrices/cubes are known as the mass-gated matrices/cubes. When it is not possible to isolate reaction products by their A/Q ratios, due to the insufficient selectivity and interfering backgrounds of isobars (nuclei with the same mass but with different Zs), an α-gating method is used. This is known as the RDT method (discussed in sec. 3.3), which correlates the α particles at the DSSD from an implanted nucleus with the coincidence γ rays emitted at the target position. Therefore, these matrices/cubes are associated with a particular nucleus via its α-decay energies.

The mass- or α-gated $\gamma - \gamma$ matrix is analyzed with a program called ESCL8R [45], which incorporates a background subtraction algorithm. This program enables the user to automatically keep track of the energy calibrations, efficiencies, and electron conversion coefficients. The γ-γ coincidence relation matrix can be examined by taking "gates", that is to select a particular γ ray on one axis and project the spectrum of coincident γ rays on the other axis. With these "gates", the γ-ray cascade to the ground state can be determined.

All the counts in a $\gamma - \gamma$ matrix with the same coordinate γ_x are projected on the other axis (y). The width in channels, i.e. γ_x, is dependent on the full width

at half maximum (FWHM) of the peak determined by

$$\mathrm{FWHM}(x) = \sqrt{f^2 + g^2 \frac{x}{1000} + (h \frac{x}{1000})^2} \tag{3.62}$$

where x is the channel number and f is a constant due to noise in the detectors and amplifiers. The term g is obtained from the statistics of the charge collection process and h is associated with the Doppler-broadening of the peaks. For an energy dispersion of 0.5 keV per channel and recoil velocity of $\sim 2.5\%$ of the speed of light, the typical parameter values are $f = 3$, $g = 1$, and $h = 4$.

In a typical Gammasphere experiment, where high fold data ($F \geq 3$) are obtained, complex analytical tools are required in order to fully extract all the information provided by the experiment. The data are sorted into γ-γ-γ cubes where LEVIT8R is used to inspect them. Furthermore, LEVIT8R offers features that can fit the energies and intensities into a two-dimensional projection or directly to the cube. These γ-γ-γ cubes, like the matrices, can also be mass- and α-gated. Cubes are basically matrices with an additional dimension. In order to examine a cube, gates are taken on two axes with different or similar energies and the spectrum of the third axis is obtained. Having an additional γ ray to gate can significantly enhance the resulting spectrum, especially in a complicated level scheme with energy doublets.

Fig 3.14 demonstrates the gating procedure in LEVIT8R on the mass-gated cube from the Gammasphere experiment. Notice the tremendous improvement and increased selectivity of double gating when compared to single gating. The double-gating procedure produces a well-resolved coincidence spectrum with no contaminant transitions and with low background.

Kinematic Doppler Shift Corrections

In a fusion evaporation reaction, the reaction products travel away from the target position with speeds exceeding 0.01 of β (the ratio of velocity of the recoil to the speed of light). Therefore, Doppler Shift corrections are essential for analyzing our data. In the Gammasphere experiment, for example, the emitted nucleus ^{174}Pt produced in the reaction ^{92}Mo(^{84}Sr,2p2n) at beam energy of 394 MeV was estimated to have a recoil velocity of $\beta \sim 0.04$. This value of β and all β values from two other reactions

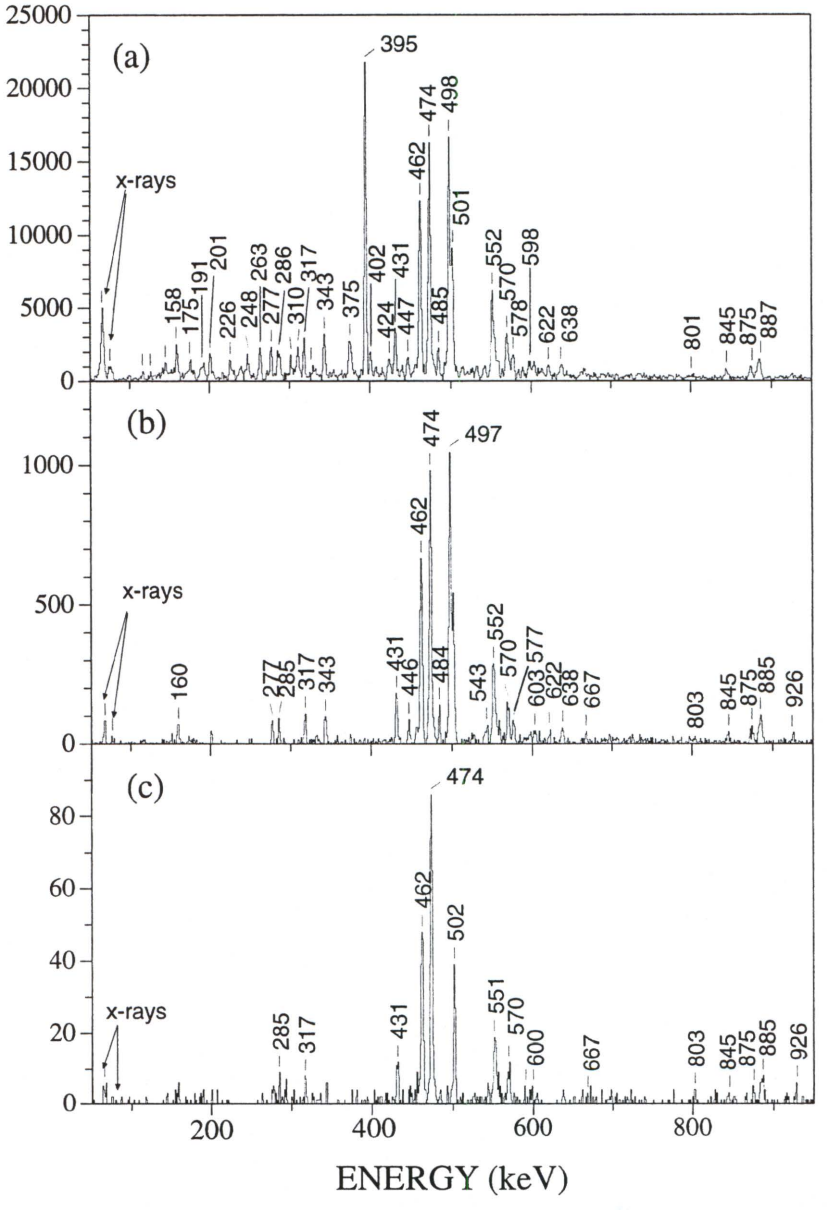

Figure 3.14: Gating on a cube in LEVIT8R. The spectrum in panel (a) shows the total projection generated by LEVIT8R on the $A = 174$ cube from a Gammasphere experiment. Spectrum (b) shows a gate on the 395-keV γ-ray transition which is associated with the ground-state band of ^{174}Pt. Spectrum (c) is the result of simultaneously double gating on the 395- and 498-keV transitions. All the labeled peaks in panel (c) belong to ^{174}Pt.

used in the experiment were inputed to the sorting program which gives Doppler corrected γ-ray energies. The typical Doppler correcting equation is given by,

$$E_\gamma = E_{\gamma[Ge]} \left(1 + \beta \cos\theta\right)^{-1}, \tag{3.63}$$

where $E_{\gamma[Ge]}$ is the energy of a γ ray reported by a Ge detector located at an angle θ relative to the beam axis. One can clearly see that the Doppler correction is proportional to the γ-ray energy. Corrections cannot be made for small angle differences of γ rays detected in different parts of a detector. The Dopler broadening is more severe at higher energies. This limits our ability to identify higher energy transitions due to large broadening in the peaks.

Determination of γ-ray Multipolarity

The discovery of new γ rays and their associated states requires the determination of the spins and parities (I^π) of these states. This has been made easier with the use of a large detector array, due to the different geometrical locations of the Ge detectors. If the transition is found to be stretched $E2$ ($\Delta I = 2$) or $M1$, then there will be no parity change between the two connecting states, however there will be a spin change of two and one units, respectively. If the parity and spin change by a unit between the two connecting states then the transition is likely $E1$.

In order to measure spin and multipolarity, a method based on the observation of Directional Correlations of de-exciting states (DCO ratios) was adopted. The theory behind this method was developed by Krane *et al.* [46]. The experimental method for deducing the DCO ratios can be found in Refs. [47, 48].

In typical fusion-evaporation reactions, produced states are oriented perpendicular to the beam axis and DCO ratios are constructed from a cascade of coincident γ rays originating from those states. The γ-γ coincidence spectra from detectors at different angles are used to determine the DCO ratios. Since the DCO ratios are dependent on the angular distribution of the emitted γ rays, an asymmetric matrix was created where energies of the coincident γ rays observed in detectors located at $\sim 35°$ and $\sim 145°$ were histogramed along one axis and the coincident γ rays at $\sim 90°$

were histogramed along the other axis. The DCO ratios are given by the equation

$$R_{DCO} = \frac{I_{\gamma_1}(\text{at } \sim 35^\circ \text{ or } \sim 145^\circ;\ \text{in coincidence with } \gamma_2 \text{ at } 90^\circ)}{I_{\gamma_1}(\text{at } 90^\circ;\ \text{in coincidence with } \gamma_2 \text{ at } \sim 35^\circ \text{ or } \sim 145^\circ)},$$

where I_{γ_1} and I_{γ_2} are the intensities of the γ ray of interest. For the given geometry of the Gammasphere, an $E1$ or $M1$ transition gives a R_{DCO} value of approximately 0.5, while R_{DCO} of an $E2$ is around 1.0. Stretched $M1$ ($\Delta I = 1$) transitions are expected to have a slightly higher DCO ratio if there is sufficient $M1/E2$ mixing. However, one has to be extremely cautious when a transition has a DCO ratio ≈ 1.0, because it might also be an unstretched dipole ($\Delta I = 0$). There is also a drawback in this method since it cannot distinguish between $M1$ and $E1$ transitions; consequently it cannot determine the difference in parity between the two connected states. However, in many cases, the parities of the low-spin band members have already been determined. Thus, identification of a stretched $E2$ transition allows the parity value of a higher-spin band transitions to be obtained.

CHAPTER 4

Experimental Results and Discussion of ^{174}Pt

4.1 Overview

Nuclei near the $Z = 82$ shell gap have been a source of interest with respect to the phenomenon of shape co-existence. Indeed, evidence for triple shape co-existence (prolate, oblate, and spherical) in $^{186}_{82}$Pb [49], $^{179}_{80}$Hg [50, 51], and $^{177}_{79}$Au [52] has been recently presented. Examples of shape competition have also been observed further away from the $Z = 82$ gap in the Pt, Ir, Os, and Re nuclei (see, for example, Refs. [53, 54, 55]). In particular, studies of non-yrast states in ^{176,178,180,182}Pt demonstrate that two co-existing minima (prolate and near-spherical) lie close in energy, with the prolate minimum being yrast for the three heavier nuclei [53].

Theoretical calculations [56] suggest that the prolate minimum is due to the excitation of two (or more) protons across the $Z = 82$ gap and into $\pi h_{9/2}/f_{7/2}$ and/or $\pi i_{13/2}$ intruder orbitals. Further away from midshell, the near-spherical minimum becomes lower in energy as TRS calculations predict [7, 8] weakly-deformed, γ-soft minima for the ground states of ^{174,176}Pt. The energy spacings of the yrast bands at low spin in ^{174,176}Pt [7, 8] lend support for these suggestions. However, the prolate minimum is low enough in energy that the excited, deformed vacuum sequence crosses the near-spherical ground-state structure at low spin ($I \approx 6\hbar$) in ^{172,174,176}Pt [6, 7, 8]. This interaction manifests itself through irregularities of the energy level spacing in the yrast states below spin 10. Empirical support for this crossing is provided by band-mixing calculations (for example Refs. [6, 7, 53, 55, 57]) which also show the separation between the two minima increases as the neutron number decreases below $N = 98$.

The nucleus ^{174}Pt is perhaps one of the clearest examples of this type of band crossing between two minima. However, the effect of this shape softness at high spin was unknown since the highest spin observed was $I = 14$ [7]. In an experiment designed to populate Au nuclei at and beyond the proton dripline [52], high-spin states in ^{174}Pt were observed to be strongly populated. This chapter focuses on the results from the ^{174}Pt channel, where the ground-state band was extended to a spin of $I = (26)$ and a side band has been clearly established. In addition to confirming the low-spin crossing in the ground-state band, there is evidence to suggest a similar crossing occurs in the side band. An unusual occurrence is seen where the first and second $i_{13/2}$ neutron alignments are observed at nearly the same frequency. This may also be the result of the interplay between competing minima with different deformation.

4.2 Experimental Details

The neutron-deficient ^{174}Pt nucleus was produced in an experiment designed to identify excited states in some of the lightest Au nuclei [52]. Beams of 380 and 385 MeV ^{84}Sr ions from the ATLAS superconducting linear accelerator at the Argonne National Laboratory (ANL) were used to bombard ^{92,94}Mo self-supporting targets. The targets used were isotopically enriched and ≈ 0.7 mg/cm^2 thick. Excited states in ^{174}Pt were populated via the $2p$- and $2p2n$-evaporation channels, respectively.

4.3 Analysis of ^{174}Pt

4.3.1 ^{174}Pt Alpha Decay

In order to study the α decay of this nucleus, a matrix of α decay energies (E_α) versus α decay time (Δt_α) was made. This matrix was further restricted to $A = 174$ recoils in order to enhance the identification of the α line in ^{174}Pt. Energy spectra were produced from this matrix by gating on different regions of the time axis. These spectra were used to deduce the alpha energies and intensities. A time spectrum was generated to measure the half-life of ^{174}Pt by using a least-square fitting routine [60].

After the α decays of ^{174}Pt, its daughter nucleus ^{170}Os [80] subsequently α

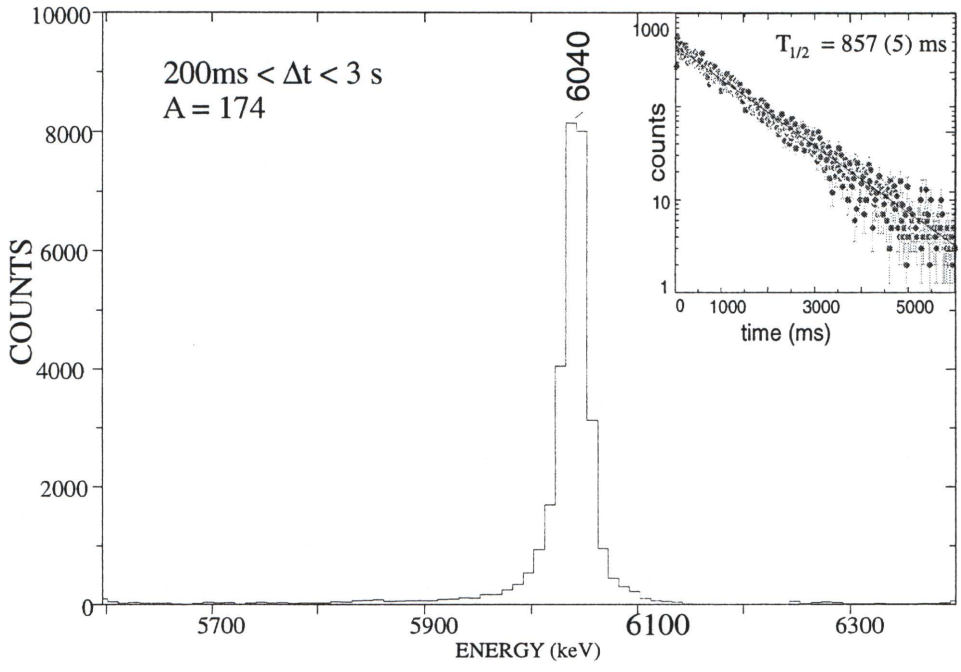

Figure 4.1: Alpha-decay and time spectra for ^{174}Pt. Alpha-decay spectrum measured within a time interval of 200 ms up to three seconds after an implantation of A = 174 recoils in the DSSD. Insert: time spectrum produced by gating on the E_α = 6040 keV. The 6040-keV α line is associated with ^{174}Pt.

decays with known lines. Since all the events in the DSSD were time-stamped, a matrix of first- and second-generation α decays was constructed to ensure the correct identification of the ^{174}Pt α line. First-generation α decays were restricted to A = 174 recoils and detection between the time interval of 200 ms to three seconds after an implantation in the same DSSD pixel. The second generation was defined as any event between two and 15 s of the first decay.

Fig. 4.1 displays the A = 174 α-decay spectrum between a time interval of 200 ms to three seconds following implantation at the DSSD, while Fig. 4.2(b) displays the correlated daughter α-decay line. An energy of E_α = 6040(5) keV and half-live of 857(5) ms were determined for the decay of ^{174}Pt.

The time spectrum of this decay is shown in insert of Fig. 4.1 by gating on the 6040 keV α line. The measured energy and half-life of the α particle decaying from the ground state of ^{174}Pt are in good agreement with the previous work [80].

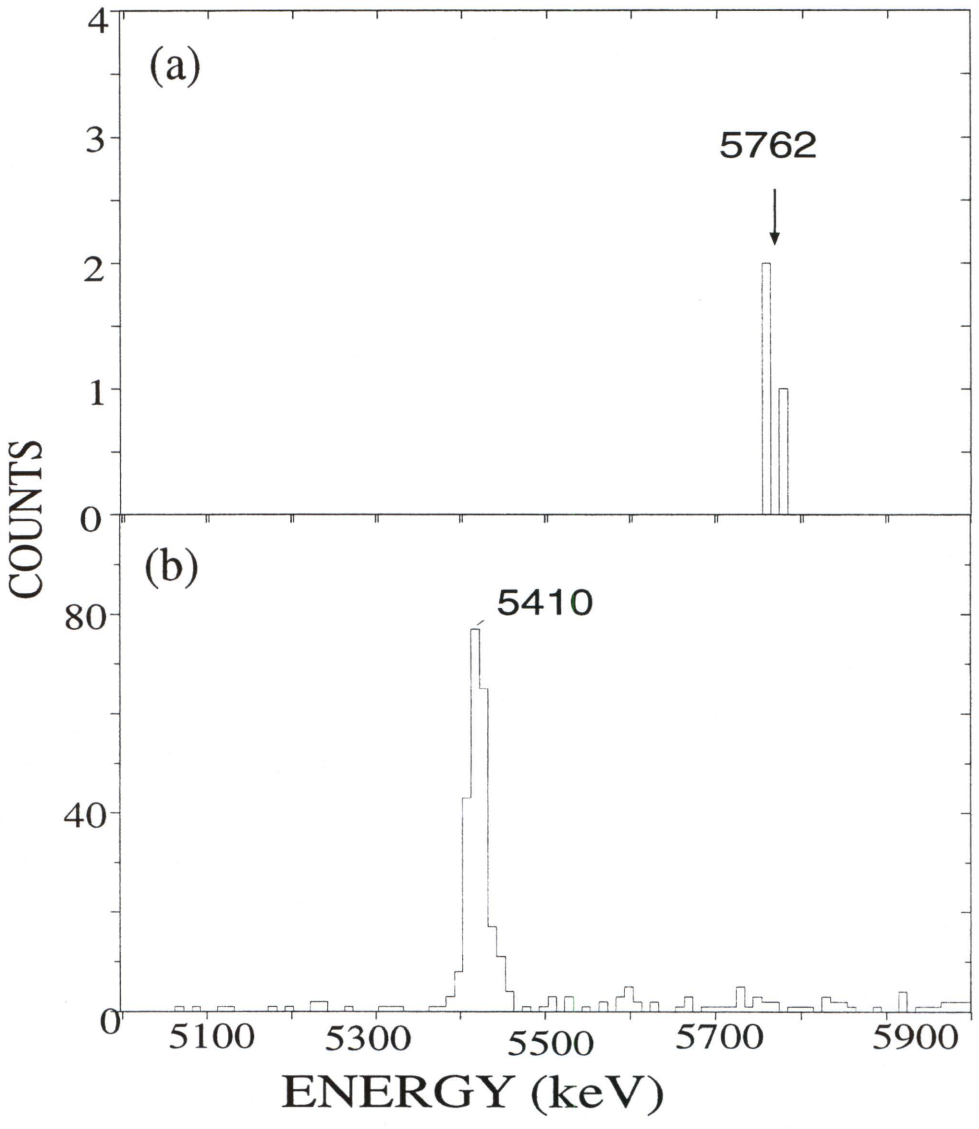

Figure 4.2: Spectra of new parent and daughter α-decay lines of ^{174}Pt. Spectrum of (a) α particles in coincidence with a weak 287-keV γ ray emitted at the focal plane of the FMA. Part (b) corresponds to the second-generation α particles emitted within 15 s after the emission of the first-generation decay, detected within a time interval of 200 ms up to three seconds after an implantation of a $A = 174$ recoil in the DSSD. The 5762- (new) and 5410-keV α lines are associated with ^{174}Pt and daughter ^{170}Os, respectively.

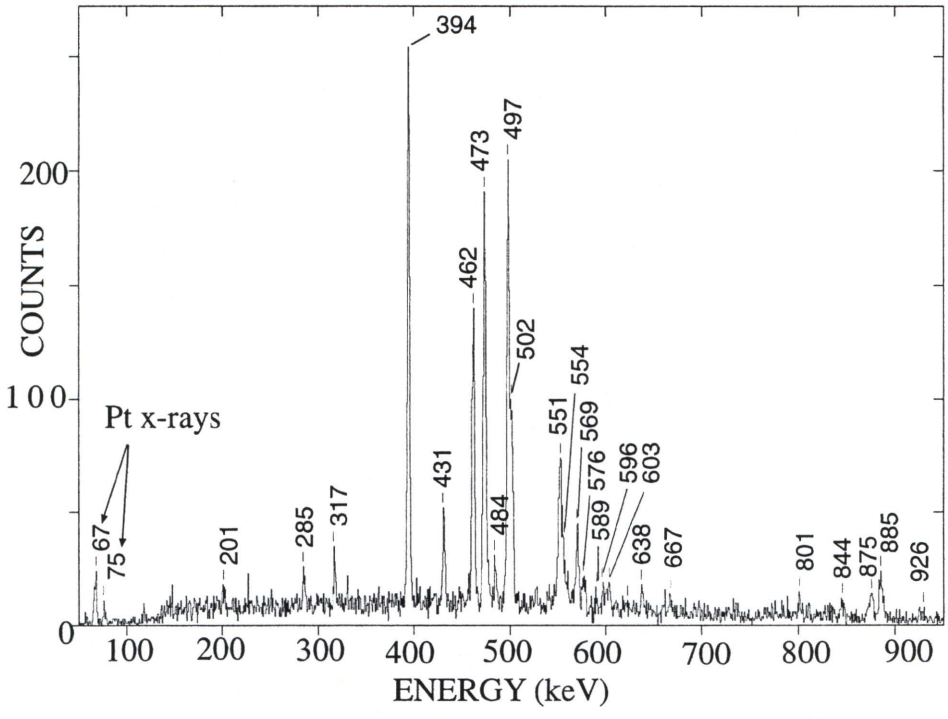

Figure 4.3: Prompt γ rays that are correlated with α-decay line at 6040 keV in ^{174}Pt.

Further supporting evidence is supplied by the RDT method shown in Fig. 4.3. This figure shows all the prompt γ rays in ^{174}Pt which are in coincidence with subsequent α decay at $E_\alpha = 6040$ keV (see also Ref [7]).

The neighboring ^{176,178}Pt nuclei exhibit α-decay fine structure where a weak α decay feeds the first 2^+ state in ^{172,174}Os, respectively. If such a structure exists in ^{174}Pt decay, one would expect the presence of a 5762-keV α particle which feeds the first 2^+ state at 287 keV in ^{170}Os [61]. Utilizing the correlations between the first-generation α decays and γ rays emitted at the focal plane of the FMA, we observed a weak 287-keV γ ray (see Fig. 4.4(b)) in coincidence with a weak 5762-keV α particle (Fig. 4.2(a)). Hence, we tentatively assigned the 5762-keV α particle to ^{174}Pt (see Fig. 4.5).

4.3.2 The Level Scheme and Spin Assignments

Excited states in ^{174}Pt have been previously studied by Dracoulis *et al.* [7], who identified the ground-state band up to spin 14 and observed excited states at (1276),

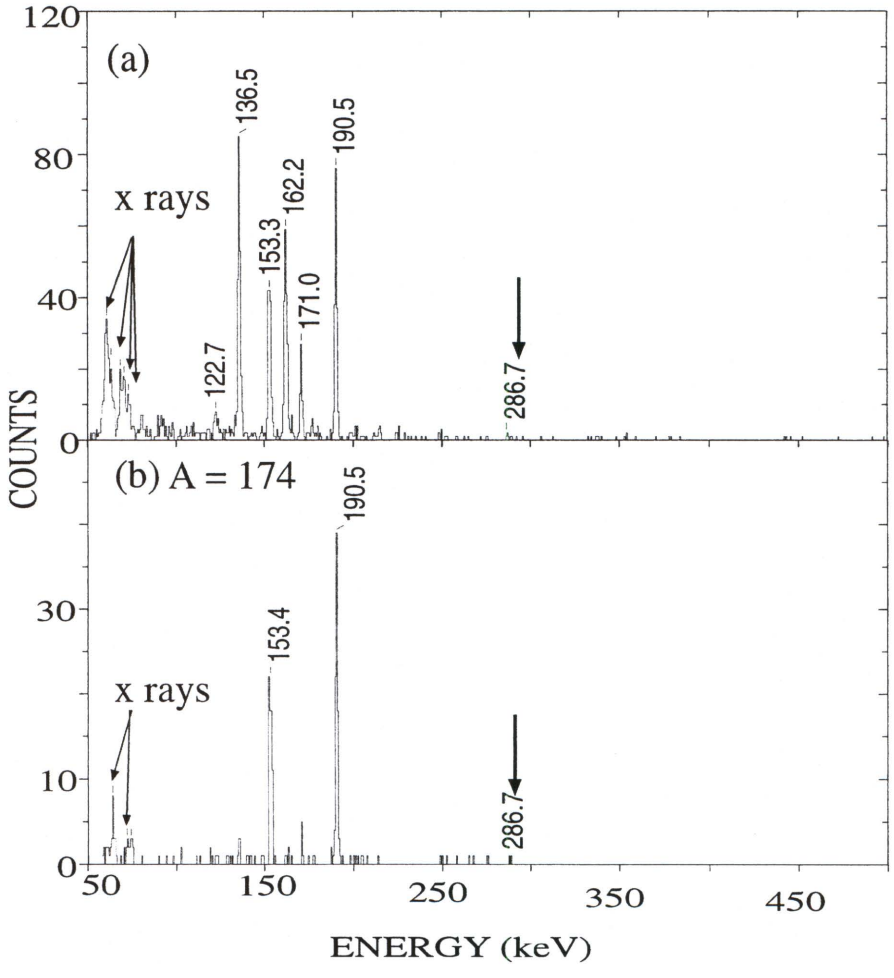

Figure 4.4: Spectra of γ rays observed at the focal plane of the FMA (^{176}Hg compound nucleus). Part (a) corresponds to γ rays of the α-decaying nuclei emitted at the focal plane of the FMA where the compound nucleus was ^{178}Hg. Part (b) corresponds to part (a) gated at $A = 174$.

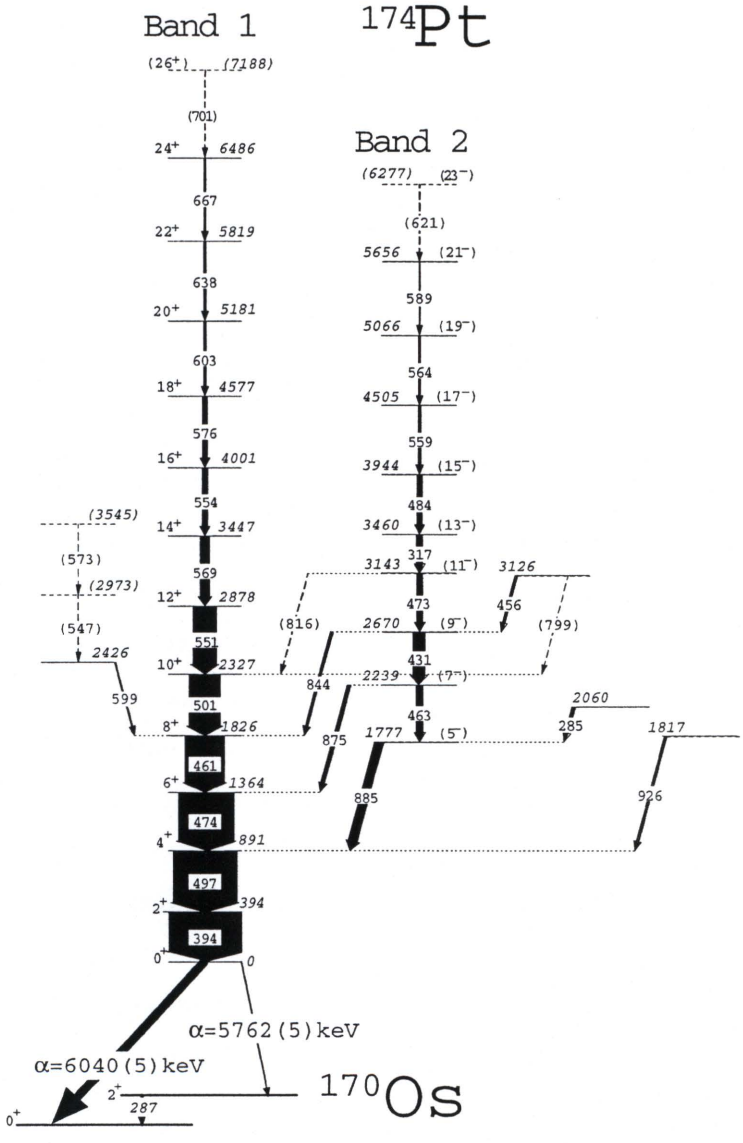

Figure 4.5: The level scheme for ^{174}Pt deduced from the present work. The arrow width is proportional to the relative intensity of the transition. Tentative spin and parity and placement are given in brackets and dashed lines.

1777, 1796 and 2061 keV. The new level scheme based upon the present study is shown in Fig. 4.5, where one may see the ground-state band extended from a spin of 14 to 24 (tentatively 26), and a new side-band is now established on the 1777 keV state, which is now observed up to $I = 21$ (tentatively 23). The (1276) and 1796 keV levels reported in Ref. [7] could not be confirmed.

Fig. 4.6(a) displays a spectrum of the ground-state band (band 1). It was obtained by summing all the combinations of double gates for transitions above $I = 8$ with the transitions below this state. The ordering of the levels above the 14^+ state is based on the measured intensities of the γ rays which are summarized in Table I. The spin assignment of these new levels must be regarded as tentative at this time. The γ-ray angular distributions were measured to be nearly isotropic for all transitions. This is likely due to the de-orientation of ions when recoiling in the vacuum [52]. It is assumed that normal rotational behavior persists above the 14^+ level, and therefore all newly placed γ transitions in band 1 are considered to be stretched $E2$ transitions. A coincidence spectrum displaying all γ transitions associated with the new side band (band 2) is shown in Fig. 4.6(b). The lowest level observed in band 2 is assumed to be the 1777 keV state. Dracoulis *et al.* [7] suggested that a 431-keV transition fed this level. However, using our coincidence cube, it was determined that a 463-keV transition (whose energy is close to the 461-keV ground-state band transition) must feed the 1777 keV level. The 431-keV transition is assigned as feeding the resultant 2239 keV state. This ordering is confirmed by the observation of the 875- and 844-keV linking transitions (see Fig. 4.5). However due to the non-rotational behavior of the 463-keV γ ray in this sequence, it is possible that the 1777 keV state belongs to another structure and the 463-keV transition may be a linking, rather than inband, transition.

The lowest state observed in band 2 could have a spin of 3, 4, 5, or 6. A spin assignment of 6 is unlikely as this would make band 2 yrast for all observed states above the 3460 keV level. In the neighboring even-even W, Os, and Pt nuclei [4, 5, 8, 62, 63, 64, 65, 66, 67, 68, 69, 70], the lowest sidebands are consistently found to have negative-parity and odd-spin. Since the experimental limitations of our data do not allow a firm spin assignment, we assume band 2 follows these systematics and

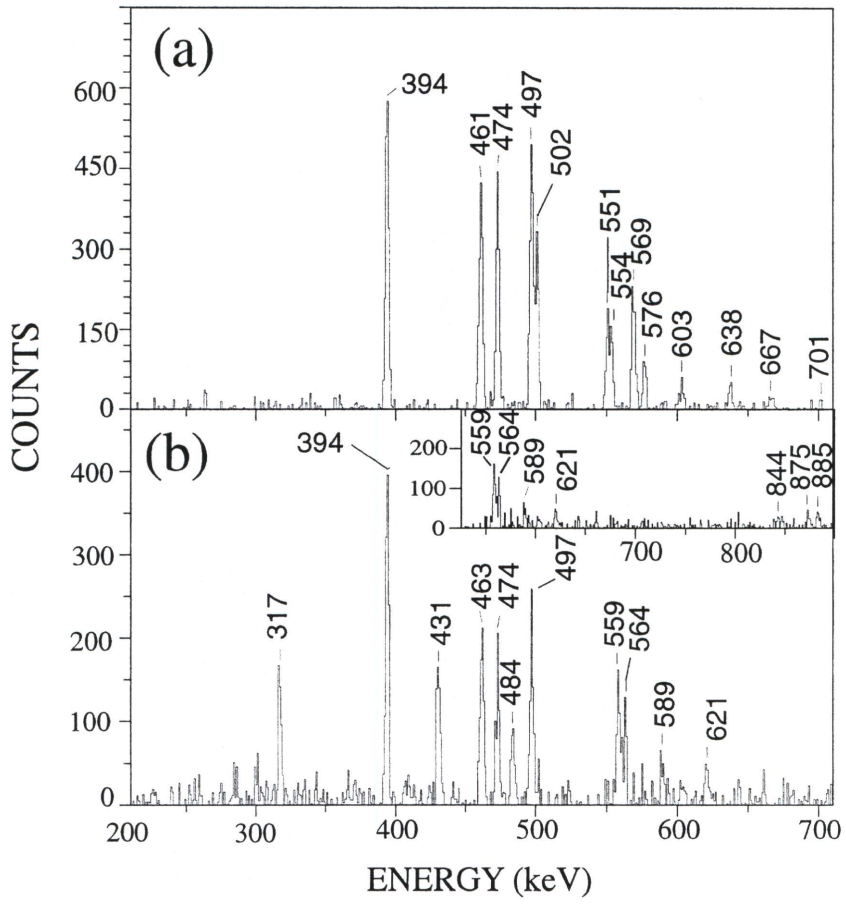

Figure 4.6: Spectra of the band 1 and 2 in ^{174}Pt. (a) Spectrum of band 1 where all the combinations of double gates were set between the 394, 497, 473 and 461 keV transitions with transitions located above the $I = 8$ state in band 1. (b) Spectrum for band 2 in which all the combinations of double gates between the 394, 497, 463 lines with the 317, 484, 559, 564, 885 keV lines were added together. All of these transitions are found in ^{174}Pt.

has odd parity and spin, thus leaving $I = 3$ and 5 as possibilities. From inspecting Fig. 4.6, one may notice band 2 is observed nearly as high in energy as band 1. Therefore, it is most likely that band 2 lies near the yrast line at higher spins. Only a spin assignment of $I = 5$ is consistent with this observation and therefore this spin is given for the state at 1777 keV. However, since this assignment is based solely on systematics, a spin assignment of $I = 4$ cannot be excluded.

It is somewhat surprising that only one linking transition is observed from each of the lower states in band 2 as two transitions are normally seen linking the lowest side-band to the ground-state band in the heavier Pt and Os nuclei [4, 5, 8, 62, 63, 64, 65, 66, 67, 68]. The $I \rightarrow I{+}1$ dipole transitions are generally found to be more intense than the $I \rightarrow I{-}1$ transitions for the lowest odd-spin sidebands. Dracoulis *et al.* [71] suggested that the enhanced $I \rightarrow I{+}1$ transition strength in these heavier Os nuclei can be explained by a phase difference in the coupling coefficient of bands with $\Delta K = 0$ and $\Delta K = 1$. However, the $I \rightarrow I + 1$ transitions are apparently missing in ^{174}Pt. De Boer *et al.* [72] stated that in the Interacting Boson Approximation model (IBA), when a nucleus approaches the vibrational limit, the $B(E1; I \rightarrow I{+}1)$ transition rate vanishes from negative-parity sidebands. This may explain the absence of the $I \rightarrow I{+}1$ transition in ^{174}Pt, because at low spin the ground-state band is more characteristic of a vibrator than a rotor, with an energy ratio of $E_4/E_2 = 2.26$ (where $E_4/E_2 = 2$ for a perfect vibrator). The placement of a relatively low-energy (317 keV) transition at high spin (13) is unusual compared with the systematics of heavier Pt nuclei. However, this γ ray was found in coincidence with the 885-, 875-, and 845-keV interband transitions in band 2. Therefore, the 317-keV transition must be placed above the 2670 keV level and from the efficiency corrected intensities, we determined the γ ray feeds the 3143 keV state. Furthermore, similar low-energy γ transitions are found at high spin in the sidebands of ^{170,172}Os [69, 70]. A new state at 3126 keV which feeds the 2670-keV state by the 456-keV transition is also established; however no further structure was observed based on this level. The placement of the 285-keV γ transition is in agreement with the previous work [7]. Surprisingly, even though the 285-keV transition is rather strong, no γ rays feeding the 2060-keV state could be confidently identified. In this work, we also established new levels at 1817

and 2426 keV. The 1817-keV state feeds the 891-keV state of the ground-state band through the 926-keV γ ray while the 2424-keV level feeds the 8^+ state via the 599-keV interband transition. Table 4.1 displays the properties of the γ-ray transitions.

4.4 Discussion

4.4.1 Ground-State Band

In order to discuss the properties of the sequences in ^{174}Pt, the alignment of bands 1 and 2 are plotted versus rotational frequency in Fig. 4.7. The choice of the Harris parameters, $J_0 = 25$ MeV$^{-1}\hbar^2$ and $J_1 = 120$ MeV$^{-3}\hbar^4$, will be addressed below. A sharp gain in alignment is observed at a frequency of 0.24 MeV in band 1. As this interaction occurs at low spin ($I = 6$), it is not likely the result of a quasiparticle alignment. A similar low-spin perturbation in the ground-state band has been observed in many of the light Os-Pt-Hg-Pb nuclei. Dracoulis *et al.* [7] interpreted this interaction as the crossing of a near-spherical ground-state sequence (g band) by a more-deformed vacuum configuration (d band) in the framework of a two band mixing model. The d band is created when a pair of nonaligned quasi-protons scatter from one orbital into a deformation-driving $\pi h_{9/2}/f_{7/2}$ intruder orbital. Therefore, the Harris parameters of the alignment plot were chosen to make the more deformed portion of band 1 have zero alignment. These parameters are consistent with values for neighboring Pt nuclei [4, 64, 68].

The band-mixing models show the moment of inertia of the d band remains nearly constant for Pt nuclei with $N \geq 96$ [62, 63]. However, recent observations of excited states in ^{173,175,177}Au [52] indicate a decreasing trend in moment of inertia of $\pi i_{13/2}$ band for $N \leq 98$ nuclei. Recent work by Danchev *et al.* [6] has shown that the d band in even-even Pt in this region has a structure similar to the deformation driving $\pi i_{13/2}$ band. Therefore it is likely that d band begins to decrease in moment of inertia and the separation between the d band the g band increases when N decreases below the $N = 98$.

At higher frequency, another crossing at 0.28 MeV is observed in band 1

Table 4.1: Data for levels and γ rays in ^{174}Pt.

$I_i^{\pi\,a}$	E_{level} (keV)	E_γ (keV)^b	$I_\gamma{}^c$	Multipolarity
		BAND 1		
2^+	393.9	393.9	$\equiv$1000	$(E2)$
4^+	891.1	497.2	857(26)	$(E2)$
6^+	1364.2	473.7	758(55)	$(E2)$
8^+	1825.6	461.4	515(33)	$(E2)$
10^+	2326.8	501.2	416(20)	$(E2)$
12^+	2877.9	551.1	319(26)	$(E2)$
14^+	3447.2	569.3	126(7)	$(E2)$
16^+	4001.1	553.9	71(10)	$(E2)$
18^+	4577.2	576.1	67(5)	$(E2)$
20^+	5180.6	603.4	33(5)	$(E2)$
22^+	5818.6	638.0	30(5)	$(E2)$
24^+	6485.6	667.0	28(4)	$(E2)$
26^+	7187.6	701.0	< 10	$(E2)$
		BAND 2		
(5^-)	1776.5	885.4	153(12)	$(M1/E2)$
$(7^-$	2239.2	462.7	106(17)	$(E2)$
		875.2	51(10)	$(M1/E2)$
(9^-)	2670	430.8	161(16)	$(E2)$
		844.3	38(6)	$(M1/E2)$
(11^-)	3143	473.2	92(30)	$(E2)$
(13^-)	3459.9	316.7	78(7)	$(E2)$
(15^-)	3943.6	483.7	68(9)	$(E2)$

Table 4.1 (continued).

$I_i^{\pi\,a}$	E_{level} (keV)	E_γ (keV)^b	$I_\gamma{}^c$	Multipolarity
(17^-)	4502.5	558.9	37(6)	$(E2)$
(19^-)	5066.4	563.9	24(5)	$(E2)$
(21^-)	5655.8	589.4	12(6)	$(E2)$
(23^-)	6277.2	621.4	11(6)	$(E2)$
		Others		
(7^-)	2060.0	284.5	47(7)	
	3125.6	455.6	3.5(2)	
	3664.6	539.0	< 5	
	2423.8	598.6	42(9)	
	1817.4	926.3	40(24)	

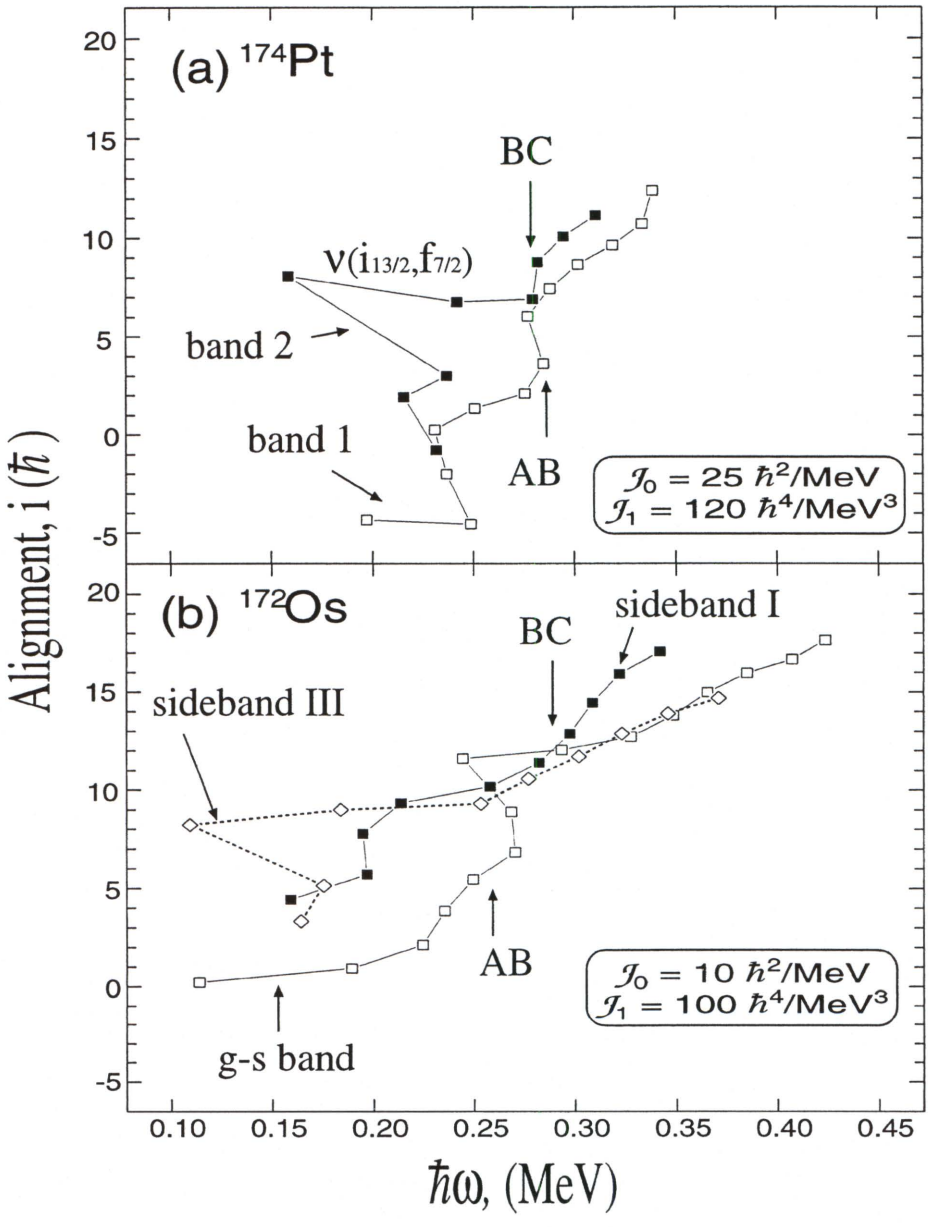

Figure 4.7: Quasiparticle alignment plots for ^{174}Pt and ^{174}Os. It is plotted as a function of frequency $\hbar\omega$ for (a) bands 1 and 2 in ^{174}Pt and (b) the ground-state and negative-parity sidebands in ^{172}Os.

with a large gain in alignment. Similar crossings have been observed in bands of the neighboring even-N nuclei; ^{172}Os (0.26 MeV) [70], ^{173}Ir (0.26 MeV) [73], ^{175}Au (0.32 MeV) [52], and ^{176}Pt (0.30 MeV) [8]. These crossings have been consistently interpreted as an alignment of $i_{13/2}$ neutrons, which is often referred to as the AB crossing in cranked shell model (CSM) nomenclature [25]. Therefore, the crossing at 0.28 MeV in the ground-state band of ^{174}Pt is also assigned as the AB alignment. However, the experimental crossing frequency is much higher than a predicted value of 0.22 MeV by CSM calculations assuming $\gamma \leq |30°|$, which will be discussed in sec. 4.4.2.

4.4.2 TRS and CSM Calculations

In order to investigate the nature of the AB delay, the systematics of the AB neutron crossing frequencies found in even-even Pt nuclei is shown in Fig. 4.8. Predicted crossing frequencies are obtained from CSM calculations using deformation parameters from TRS calculations [28, 29]. The deformation parameters are obtained from a calculated frequency ($\hbar\omega \approx 0.21$ MeV for the Pt nuclei shown in Fig. 4.8) just below the experimental observed crossing frequency. CSM calculations were then performed to predict the AB crossings and the results are compared with experimental values in Fig. 4.8. In this manner, the calculations are able to reproduce the general trend of the experimental crossings; however, the calculated values are generally smaller than the experimental values. It is possible that the difference in magnitude may be due to shape variations between the ground and s-band. The agreement with the data becomes increasingly worse as the neutron number decreases. It becomes evident that this method may not be the best method for predicting crossing frequencies in the lightest Pt nuclei.

Figure 4.9 displays the total Routhian surfaces for four frequencies of the ground-state configuration in ^{174}Pt. At $\hbar\omega \approx 0.21$ MeV [Fig. 4.9(b)], one can see the complexity of this nucleus as a multi-minimum surface is observed. The lowest calculated minimum [labeled as I in Fig. 4.9(b)] has $\beta_2 \approx 0.15$ and $\gamma \approx$ -25°, while a second minimum (II) exists with $\beta_2 \approx 0.15$ and $\gamma \approx +15°$ and a third (III) occurs

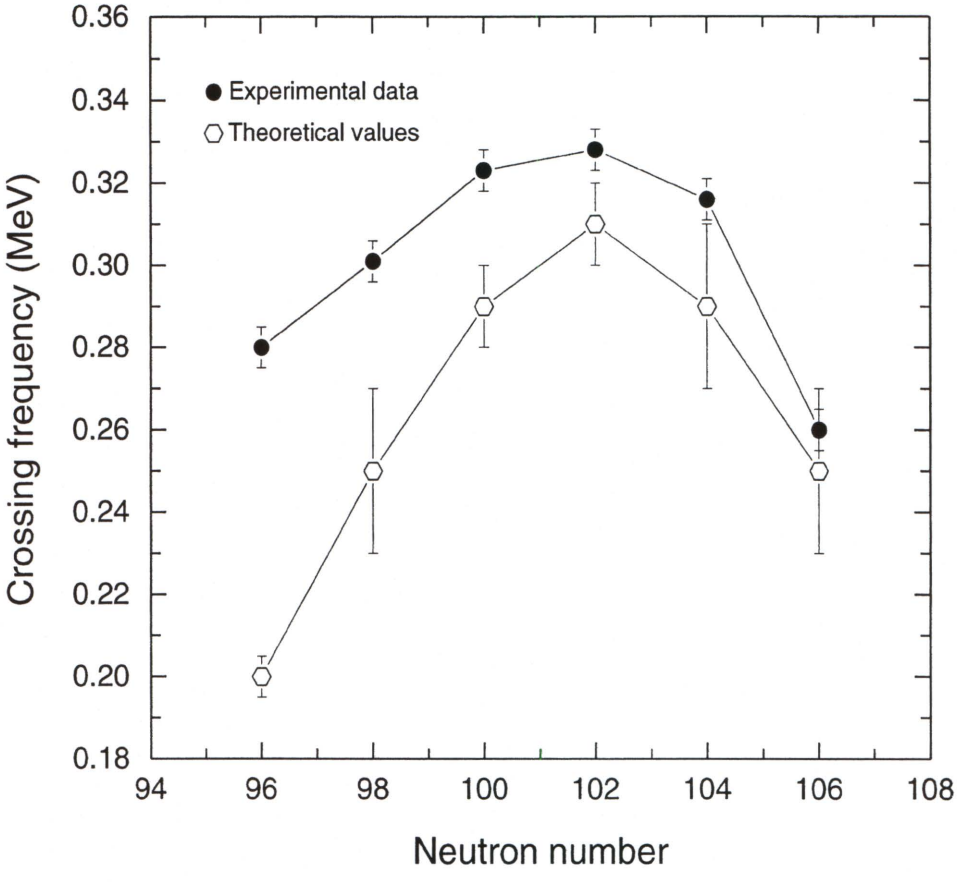

Figure 4.8: Predicted crossing frequencies for $^{174-184}$Pt. Crossing frequencies in Pt nuclei ground-state bands for experimental data and theoretical values obtained from the Cranked Shell Model where parameters are obtained from TRS plots at $\hbar\omega \approx$ 0.21 MeV (denoted by open hexagons). The error-bar associated with the theoretical calculations are due to the interaction strength suggested by the CSM.

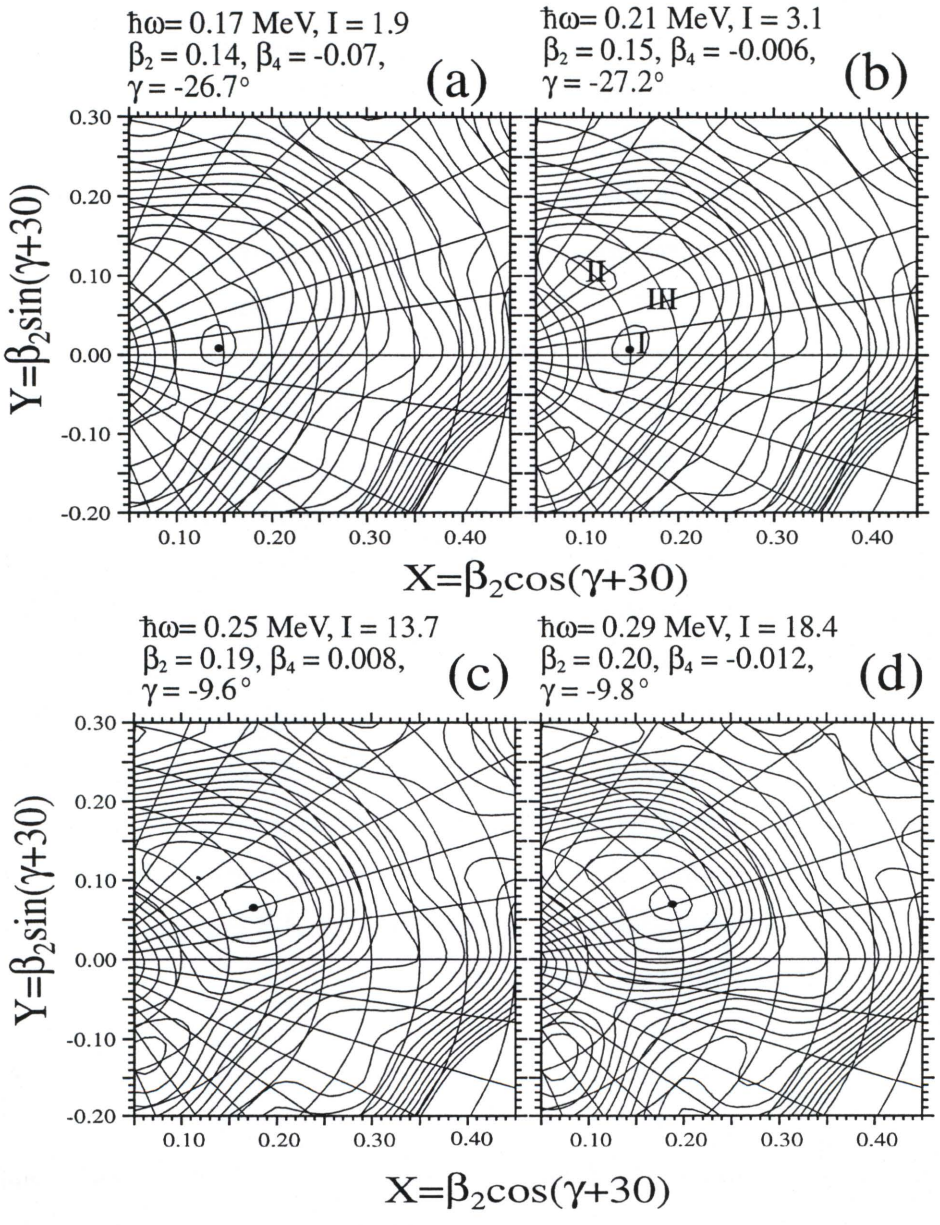

Figure 4.9: Total Routhian Surfaces plots for the yrast configuration (band 1) in ^{174}Pt.

with $\beta_2 \approx 0.19$ and $\gamma \approx$ -10°. This third minimum becomes lowest at the next highest frequency [Fig. 4.9(c)], but the large jump in spin ($\Delta I = 10.6\ \hbar$) indicates the surface at $\hbar\omega \approx 0.25$ MeV is either in a crossing region or follows a crossing. Thus, there are no stable minima from which to deduce deformation parameters for CSM calculations that are dependent on a stable deformation. Since the CSM is not able to predict the alignment of AB neutrons in a soft nucleus such as ^{174}Pt, the TRS calculations were inspected for possible crossing frequency predictions.

Figs. 4.9(b)-(d) shows spin gains of 10.6 and 4.7 $\hbar$ from $\hbar\omega \approx 0.21$ MeV to 0.25 MeV and 0.25 MeV to 0.29 MeV, respectively, which imply alignment gains. In the first alignment gain, structural evolution occurs from a multi-minimum surface ($\hbar\omega \approx 0.21$ MeV) to a surface with a more stable minimum ($\hbar\omega \approx 0.25$ MeV). We interpret the first alignment gain as a result of a shape change with some components of an aligned AB neutron state, at a frequency near 0.23 MeV. This interpretation is consistent with observed data (see Fig. 4.7), where the low-frequency crossing at $\approx$ 0.24 MeV is associated with a change in shape. The latter crossing predicted by the TRS is interpreted as the AB alignment at a frequency near 0.27 MeV. In addition, TRS calculations for band 2 (not shown) predict a crossing near 0.27 MeV. Once again this is in good agreement with experimental data. Since the TRS calculations (where deformation changes are considered) can better describe the observed crossings in ^{174}Pt than the CSM (where stable deformation is required), it appears that the interaction of the multiple shape minima influences the AB crossing frequency such that it is delayed and occurs near the BC crossing.

4.4.3 Octupole Vibration

In addition to the phenomenon of shape co-existence, many even-even nuclei also exhibit various collective and quasiparticle excitations. Examples of these collective structures are low-lying negative-parity bands which are associated with cascading stretched quadrupole transitions. These bands are widely observed in the Os-Pt-Hg nuclei [4, 5, 8, 64, 65, 66, 71]. At low spin, their configurations are usually associated with a single-phonon octupole vibration, although a different interpretation

has been proposed [65, 66]. At higher frequency, the octupole bands are crossed by two-quasiparticle configurations.

In this region, the existence of low-spin octupole states can be attributed to the overlaping high-j intruder orbitals ($i_{13/2}$ neutrons, $h_{11/2}$ protons) with low-j ($f_{7/2}$ neutrons, $d_{5/2}$ protons). The $I^{\pi} = 3^{-}$ octupole states in nuclei occur when two different orbitals near the Fermi with $\Delta j = \Delta l = 3$ interact. The 3^{-} octupole phonon can be separated into quadruplets, $K^{\pi} = 0^{-}$, 1^{-}, 2^{-}, and 3^{-}. Neergard *et al.* [5] suggested that these octupole quadruplets can be associated with well defined rotational bands but are highly perturbed by the Coriolis interaction at high spin. Therefore, it is likely that band 2 is an octupole vibration at low spins ($I \leq 11$). The fact that band 2 has an alignment of 2-3 $\hbar$ more than the ground-state band (see Fig. 4.7) for the first three frequencies is consistent with this interpretation.

In this region [4, 5, 8, 64, 65, 66, 71], negative-parity odd-spin states are favored over even-spin states and this suggests that band 2 has odd-spin and negative parity. For odd-spin states that have higher components of K that dominate, $I \rightarrow I + 1$ transitions are favored over $I \rightarrow I$ - 1 . This behavior is observed in heavier Os and W nuclei in the 180 region, where the $K = 2$ and $K = 3$ components are predominant. But in light Sm and Gd nuclei, the odd-spin bands have larger $K = 0$ components at low spin. Hence $I \rightarrow I$ - 1 transitions are observed to be dominant. Further detail can be found in Ref. [71, 74].

The absence of $I \rightarrow I + 1$ transitions from band 2 of ^{174}Pt is further indication that the $K = 0$ octupole component is highly favored. One may also note that the light $^{166-172}$Os nuclei [67, 69, 70], which are less deformed than heavier Os nuclei, exhibit a stronger $I \rightarrow I$-1 transition than $I \rightarrow I$+1 from the 5^{-} state of the odd-spin sideband. This would also indicate a predominant $K = 0$ octupole component for the 5^{-} state in these light Os nuclei.

In Fig. 4.7, one may notice an alignment occurs in band 2 at $\hbar\omega = 0.23$ MeV that is similar to the low-spin crossing displayed in band 1. This assumes that the 463-keV γ ray is indeed an inband transition. Following the argument for band 1, it is possible that band 2 begins as an octupole vibration based on the near-spherical ground-state sequence. This structure may then be crossed by an octupole

vibrational band based on the more-deformed vacuum configuration which accounts for the crossing at 0.23 MeV. Such a crossing has also been observed in the negative-parity sideband of ^{178}Hg [75].

Band 2 experiences another sharp gain in alignment following the crossing at 0.23 MeV, likely resulting from a change in configuration. After this second crossing in band 2, the sequence likely has the $\nu(i_{13/2}, f_{7/2})$ configuration. This interpretation was suggested by Voigt *et al.* [5] and has been used to describe similar crossings in sidebands of neighboring ^{174}Os [71], ^{178}Pt [4], and ^{178}Hg [75] nuclei. Following this crossing, band 2 has an additional $\sim$6 $\hbar$ of alignment as compared with band 1. This is consistent with the suggested change in configuration as the $i_{13/2}$ and $f_{7/2}$ neutrons are associated with $\approx$4 $\hbar$ and $\approx$2 $\hbar$ of alignment, respectively. The sharp backbend implies that the interaction strength between the octupole band and the two-quasiparticle configuration is very weak, as is found in ^{168,170,172}Os [67, 69, 70]. However, heavier Os and Pt nuclei do not exhibit this phenomenon. The appearance of this backbend at $N \leq 96$ for both Os and Pt (see Fig. 4.8) suggests that the octupole band in both Os and Pt nuclei have similar $\Delta l = \Delta j = 3$ orbitals coupling and are likely neutron orbitals.

At higher frequency, a third crossing at 0.29 MeV is observed in band 2. The AB neutron crossing is Pauli blocked in band 2 because the configuration already involves a $i_{13/2}$ neutron. The next available predicted crossing results from an alignment of a second pair of $i_{13/2}$ neutrons, namely the BC crossing. One may notice that this implies that the BC crossing is very close to the AB crossing (0.28 MeV) in band 1. The small difference between those two neutron crossings is unusual, as normally a frequency difference of approximately 50 keV is observed. For example, in Fig. 4.7(b) the ground-state band and two sidebands which involve the $i_{13/2}$ neutron are plotted for ^{172}Os [70]. The perturbation in the alignment for the ground-state band below 0.25 MeV is once again due to the interaction between the g and d bands. The AB alignment is then observed at 0.26 MeV, while the BC crossing is found near 0.30 MeV in the sidebands. Since the sidebands in both ^{174}Pt and ^{172}Os display the BC crossing near 0.30 MeV, it appears that the AB crossing is delayed in the ground-state band of ^{174}Pt.

4.4.4 Fractional Filling of the Shell

As mentioned in the previous section, low-lying negative-parity states in even-even nuclei have been associated with single-phonon octupole vibrations. In the rare-earth region, bandheads of the $K^\pi = 0^-$, 1^-, 2^-, and 3^- octupole bands have been observed. For the lighter nuclei, the $K^\pi = 0^-$ bandhead is observed to have the lowest excitation energy. As the neutron or proton number increases, the $K^\pi = 1^-$ component becomes the lowest and $K^\pi = 0^-$ goes up in energy. In the region of heavier isotopes, $K^\pi = 3^-$ becomes the lowest octupole state while $K^\pi = 0^-$ the highest. This phenomenon was first identified by Neergard and Vogel [74].

Similarly, Cottle *et al.* [76, 77] investigated the systematics of low-lying ocutpole states in the rare-earth region using the Interacting Boson Approximation (IBA) [78]. In that work, the systematical trend of the octupole centroid energies from the lighter to the heavier nuclei (N = 82-126) was reproduced theoretically.

In order to understand systematics of excitation energy of the octupole states, a method correlating the location of the unique orbitals with respect to Fermi surfaces and excitation energy of the octupole states were suggested by Cottle *et al.* [76, 77] and others [79]. It is called the fractional filling of the shell method (FFS). It is a schematical approach of mapping known experimental octupole vibration states with fractional filling of the shell. In this method, a ratio of excess protons and neutrons beyond the shell gap called F ("fractional shell filling") interpreted as an empirical analog mimicking the Fermi surface. F is given by the equation

$$F = \frac{1}{2}\left(\frac{p}{32} + \frac{n}{44}\right) \tag{4.64}$$

where p/n is the number of valence proton/neutron particles or holes counted from the nearest magical shell gap. This equation is valid for nucleus with $50 \leq p \leq 82$ and $82 \leq n \leq 126$. When K= 0^-, 1^-, and 2^- octupole bandhead are plotted with respect to F, a systematic trend is observed. In the begining of the deformed region, the lowest excitation is K= 0^-, followed by 1^- and 2^-. As the Fermi level increases, band ordering changes to K= 1^-, 0^-, 2^-, and to K= 1^-, 2^-, 0^- as the nucleus approaches mid-shell (see Fig. 4.10).

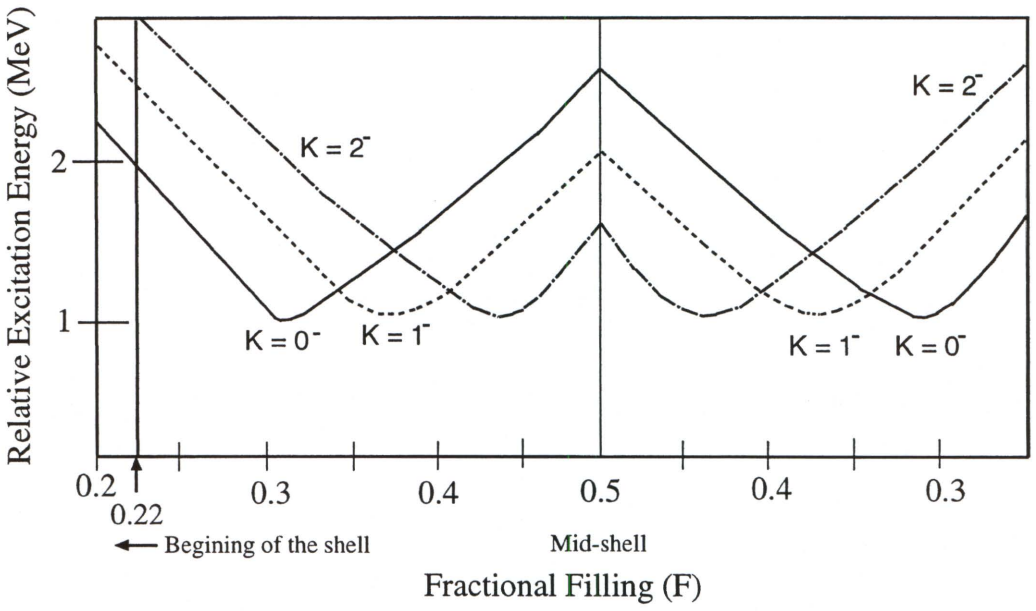

Figure 4.10: The fractional filling of the shell plot. It is for the octupole states in the rare earth nuclei. This figure is reproduced and modified from Fig.2 in Ref. [76]. The vertical line at 0.22 corresponds to ^{174}Pt.

Fig. 4.10 summarizes the evolving trend for octupole band ordering with the addition or subtraction of nucleons from the nearest shell gap for deformed rare-earth nuclei. Assuming that it is possible to use this plot to describe nuclei ($^{172-180}$Pt) far from the valley of stability, FFS is applied to ^{174}Pt. For ^{174}Pt where $F = 0.22$, the lowest octupole band should be $K= 0^-$ according to Fig. 4.10. Therefore, it is also consistent with our interpretation that our lowest negative-parity band is likely $K= 0^-$, which has odd spins.

CHAPTER 5

Experimental Results in ^{173}Pt and ^{175}Ir

5.1 Overview

The α-decay process has long been known as easy to understand in principle but difficult to interpret precisely. The α-decay rates are dependent on the tunneling probability through the Coulomb barrier as well as energies and angular momenta of the emitted particles and configurations of the parent and daughter states. Alpha decays are likely to populate low-lying states in daughter nuclei and provide valuable information on their single-particle structure. Fine structure intensity patterns are interesting in their own right. The most intense alpha emissions tend to occur between parent and daughter states of similar spin and parity.

The α-decay properties of neutron-deficient $^{171-175}$Ir [13], $^{172-178}$Pt [80, 81], and $^{168-174}$Os [81] have been studied previously; α emission is the primary mode of decay for the lighter of these nuclei. From these studies decay information such as the Q value is used to determine the location of the proton dripline, hence the experimental limits to nuclear existence.

The α decays of the odd-A ^{173}Pt and ^{175}Ir have been studied by a number of investigators [13, 80, 81, 82, 83, 84]. Previous work on ^{173}Pt identified one α-decay line. However, in ^{175}Pt [18, 81] α-decay fine structure was observed where the strongest line feeds an excited state at 77 keV in the daughter nucleus. Hence, this dissertation investigated similar structure in ^{173}Pt. In odd-A Au and Ir nuclei, the phenomenon of isomerism is a frequent occurrence. For $^{171-177}$Au and $^{167-173}$Ir, the α-decaying states are usually associated with low-spin $d_{3/2}/s_{1/2}$ and high-spin $h_{11/2}$ orbitals. However in heavier Au and Ir nuclei, the π $h_{9/2}$ [541]1/2 plays a dominant role.

5.2 Experimental Details

Alpha particles and γ rays of neutron-deficient ^{173}Pt, ^{175}Ir, and ^{177}Hg nuclei were produced via the ^{92}Mo(^{84}Sr,2pn), ^{94}Mo(^{84}Sr,3p), and ^{96}Mo(^{84}Sr,3n) reactions, respectively. In order to analyze α decay of these nuclei, histograms of $E_{\alpha 1}$ - Δt, E_f - $E_{\alpha 1}$, E_γ - $E_{\alpha 1}$, and $E_{\alpha 1}$ - $E_{\alpha 2}$ were made. The notations γ, f, Δt, $\alpha 1$, and $\alpha 1$, correspond to the prompt γ ray, γ ray detected at the focal plane of the FMA, time interval between implantation and decay, first-, and second-generation α particle, respectively. All these histograms were further restricted to the recoil of interest. Data from these histograms are analyzed using the "DAMM" and *GF*3 software. Further experimental details can be found in sec. 3.2.

5.3 Experimental Results

5.3.1 ^{173}Pt Alpha Decay

Fig. 5.1(a) displays the α-decay spectrum associated with $A = 173$ recoils in which an α particle was observed less than one second after an implantation in the same pixel of the DSSD. The strongly populated α-decay line at 6232 keV with the half-life of 382(2) ms is associated with ^{173}Pt because it is correlated with the previously identified daughter ^{169}Os decay at $E_\alpha = 5581$ keV. Furthermore, its RDT spectrum shows prompt γ rays associated with ^{173}Pt [86]. Three new α-decay lines are observed at 6128, 6100, and 6067 keV. Their RDT spectra (Fig. 5.2) are similar to each other and also to that of the ^{173}Pt α line at 6232 keV, indicating that all these α particles originate from the same state in ^{173}Pt. The presence Pt x-rays in the RDT spectra indicates that these new α-decay lines are associated with Pt.

The α lines at 5418, 5672, and 5737 keV are associated with ^{173}Ir decay because their RDT spectra (Figs. 5.3(a,c,d)) exhibit γ-ray transitions observed in ^{173}Ir [86, 73]. As stated above, the 5581-keV α-decay line is associated with ^{169}Os decay, and our measured half-life of 4100(400) ms is in agreement with the previous work [12]. The presence of $A = 169$ α decays in the $A = 173$ spectrum (Fig. 5.1(a)) is due to the mis-detection of the parent decay by the DSSD when the parent α-

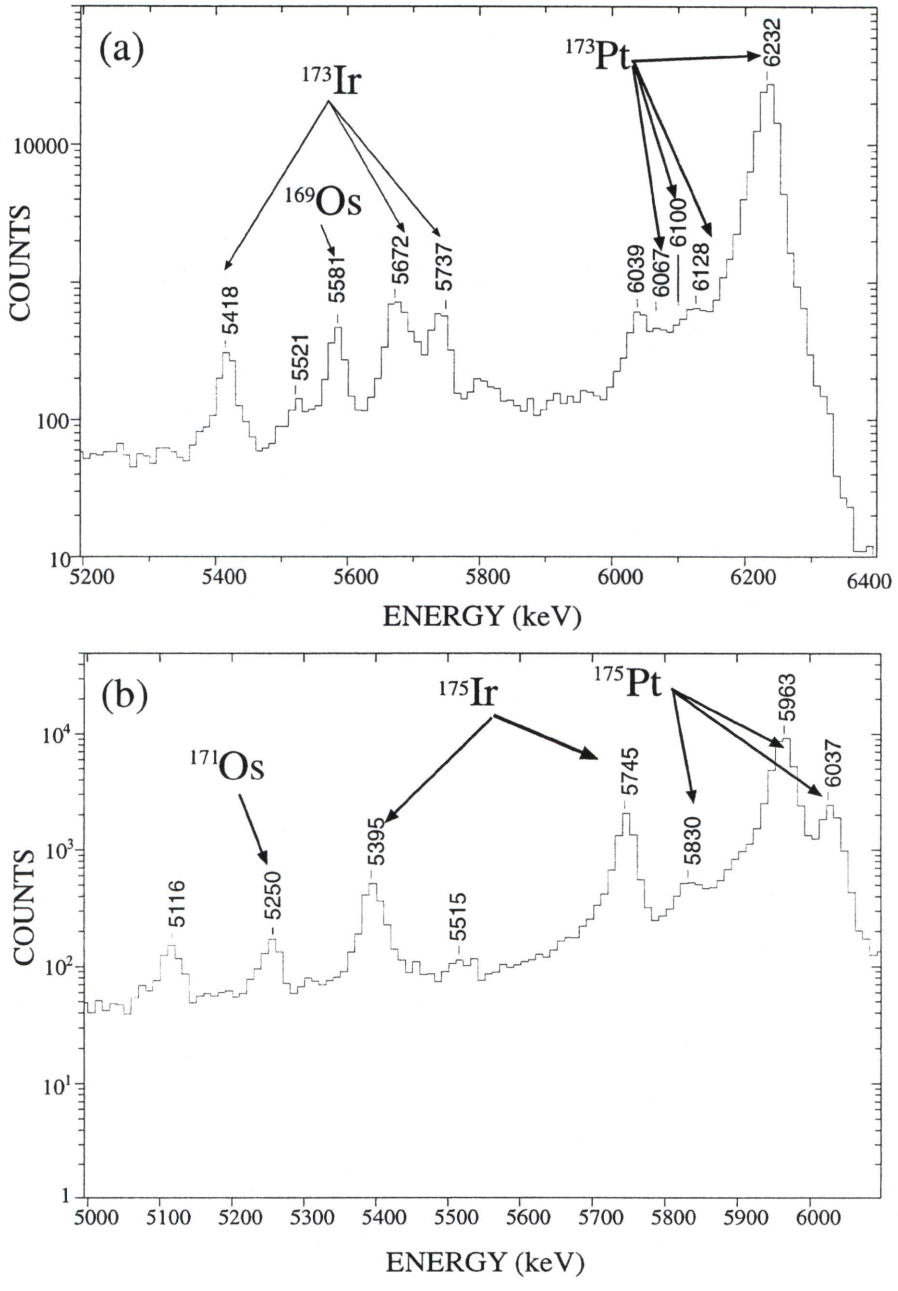

Figure 5.1: Alpha-decay spectra of $A = 173$ and 175 recoils. (a) Mass-gated α-decay lines detected within one second following an implantation of $A = 173$ recoils in the DSSD. (b) α-decay spectrum detected within a time window of one to five seconds after implantation of $A = 175$ recoils in the DSSD.

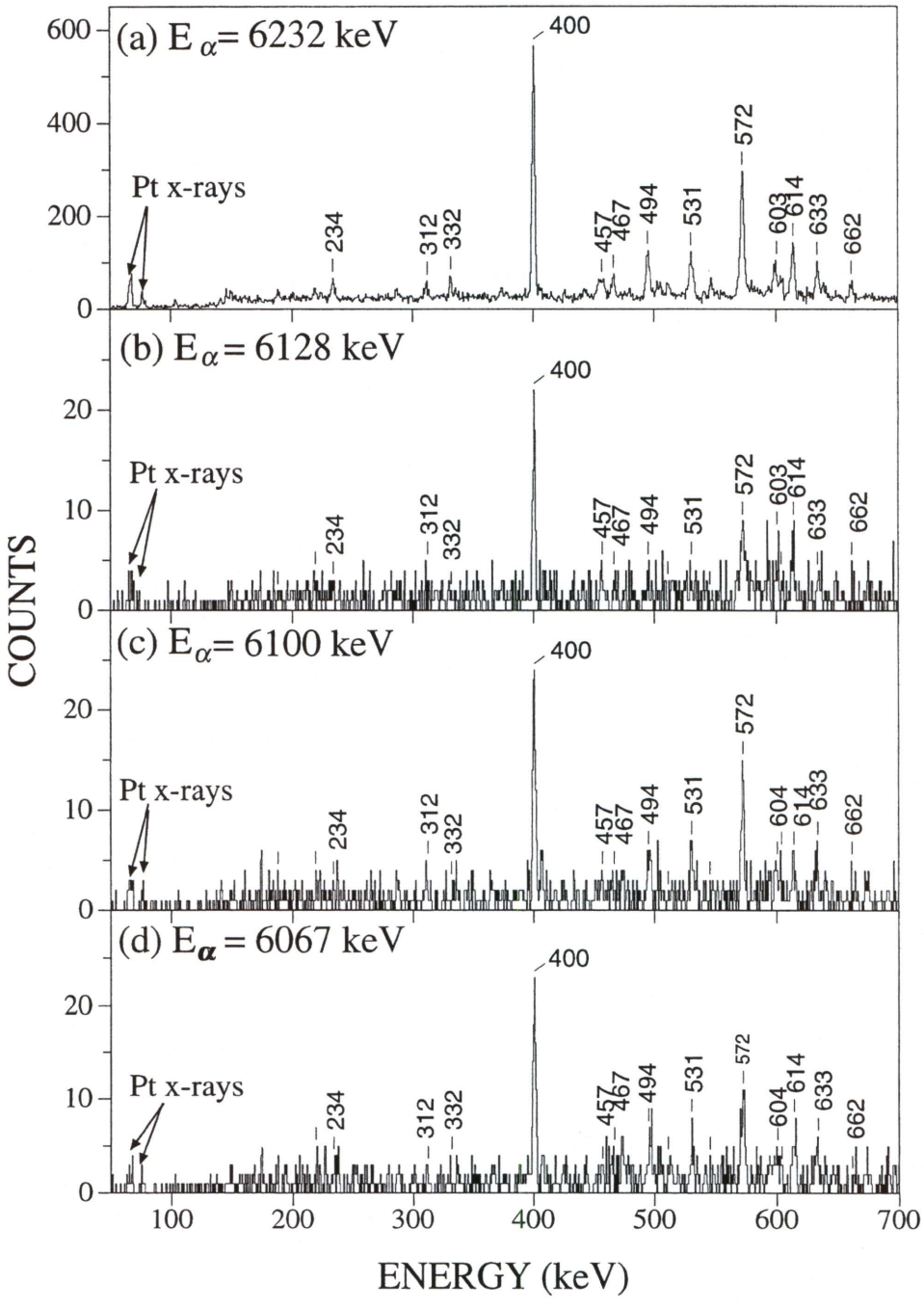

Figure 5.2: RDT spectra of γ rays associated with ^{173}Pt. Prompt γ rays emitted by $A = 173$ nuclides which subsequently emitted the (a) 6232-, (b) 6128-, (c) 6100-, and (d) 6067-keV α particles. These γ rays are associated with ^{173}Pt [86].

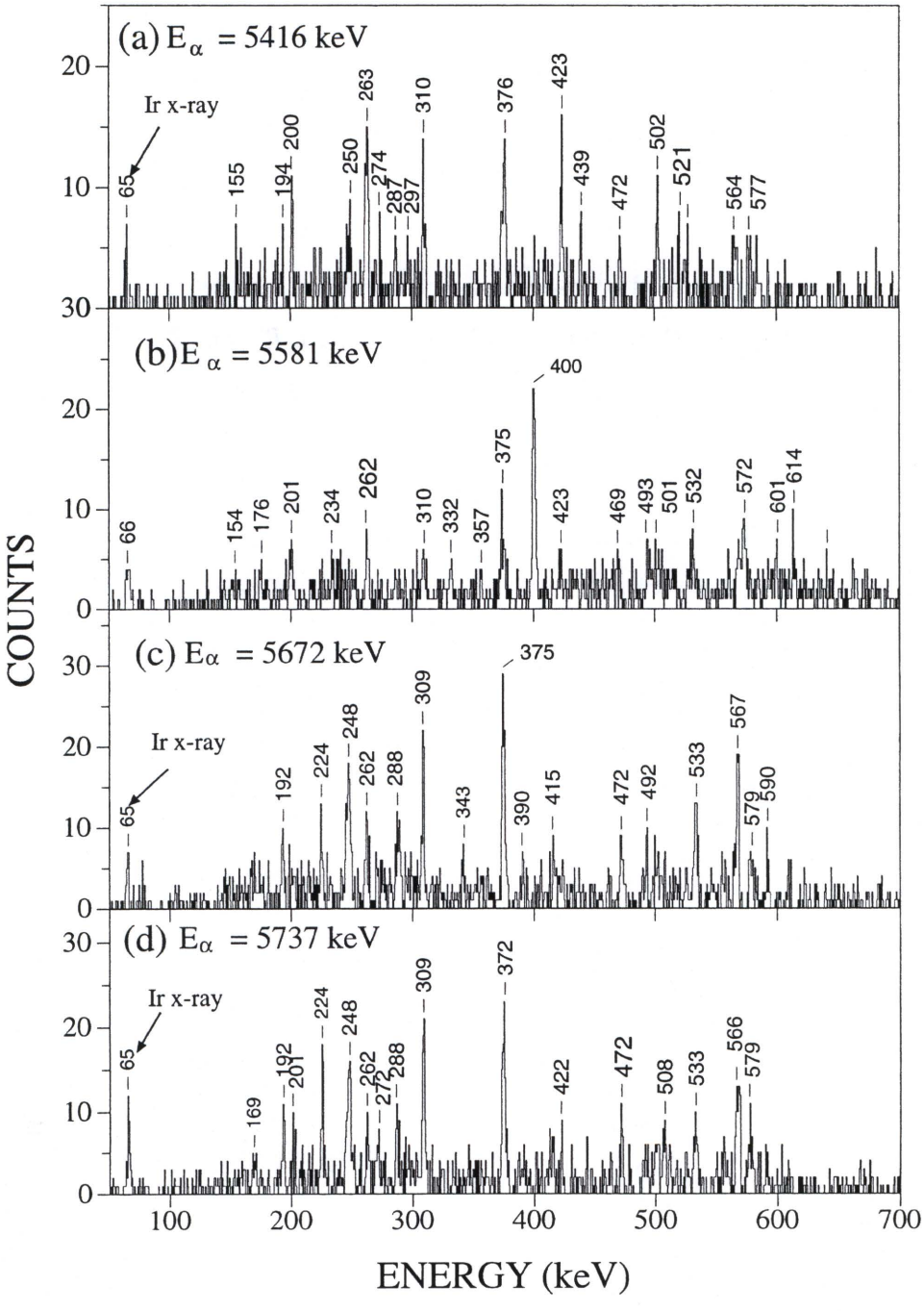

Figure 5.3: RDT spectra associated with $A = 173$ recoils. Prompt γ rays emitted by $A = 173$ nuclides which subsequently emitted the (a) 5416-, (b) 5581-, (c) 5672, and (d) 5737-keV α particles. The γ rays in (a), (c), and (d) are associated with ^{173}Ir [73].

decay particle is emitted through the front surface of the DSSD. The subsequent α particle from the daugther decay will be tagged as a parent decay. Tagging on these mis-identified α particle results in the RDT spectrum of the parent nucleus.

Inspecting the coincidence relationship between these alphas and subsequent γ rays observed at the focal plane of the FMA (see Fig. 5.4), no γ ray was found to be in coincidence with the 6232- or the 6128-keV α-decay lines. However, the 136-keV γ ray is found in coincidence with α-decay lines at 5672 and 6100 keV, while the 171-keV γ ray is correlated with the 6067-keV α particle. Re K_α and K_β x-rays are found to be in coincidence with the 5737-keV α-decay line. The coincidence between the 5672-keV α particle and the 136-keV γ ray was previously reported by Schmidt-Ott *et al.* [13] and they assigned this decay to ^{173}Ir. The presence of Re x-rays in coincidence with the 5737-keV α decay indicates that this α-decay line is a "fake" peak. This "fake" line is due to the summing contribution of the K-conversion electrons from the 136-keV state in ^{169}Re and its correlated α-decay line at 5672 keV.

In order to sum the energy of the α-decay line and its correlated γ-ray energy (a transition in the daughter nucleus), the energy of the α-decay line has to be converted into its Q-value. The Q-value conversion formula is given by

$$Q \sim (\frac{4 + A_d}{A_d})E_\alpha \tag{5.65}$$

where A_d, E_α, and Q are mass of the daughter nucleus, α energy, and Q value of the parent nucleus, respectively. The Q-value conversion calculations for ^{173}Pt α-decay energies are shown below.

$$E_\alpha = 6067 \text{ keV} \rightarrow Q_\alpha = 6210 \text{ keV} \rightarrow (6210 + 171) \text{ keV} = 6381 \text{ keV}$$
$$E_\alpha = 6100 \text{ keV} \rightarrow Q_\alpha = 6244 \text{ keV} \rightarrow (6244 + 136) \text{ keV} = 6380 \text{ keV}$$
$$E_\alpha = 6232 \text{ keV} \rightarrow Q_\alpha = 6380 \text{ keV}$$

The sum of the Q-value of α-decay lines at 6067 and 6100 keV and their correlated γ-rays approximately equals the Q-value of the 6232-keV α peak. This is the energy of the previously reported ^{173}Pt α decay. This would indicate that the α lines at 6067 and 6101 keV are associated with ^{173}Pt and the 6232-keV alpha feeds the α-decaying ground state of ^{169}Os.

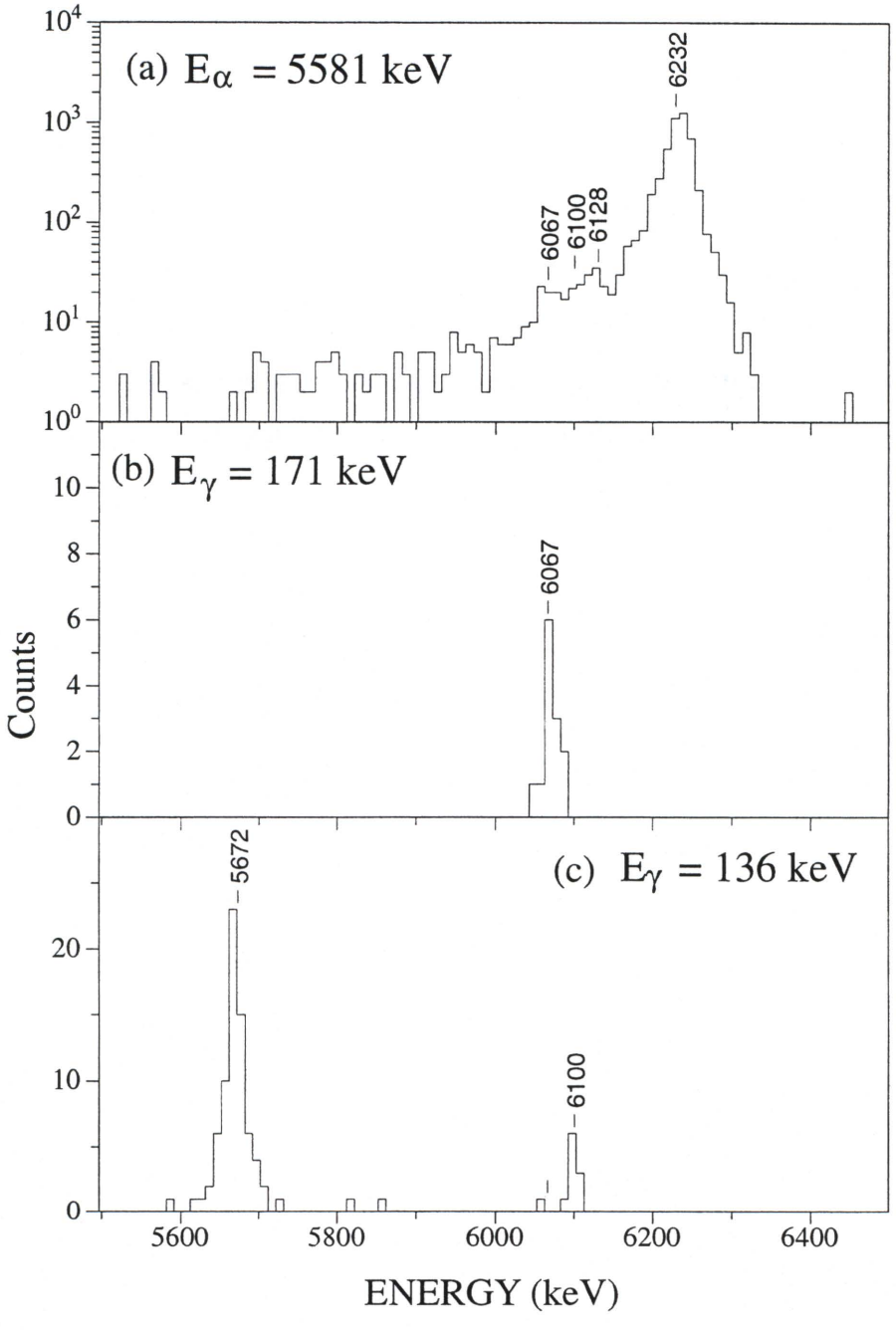

Figure 5.4: Spectra displaying α-decay properties of ^{173}Pt. (a) Spectrum of first-generation α-decay lines of $A = 173$ recoils when gated on the daughter (^{169}Os) decay line at 5581 keV. Parts (b) and (c) correspond to $A = 173$ α-decay lines in coincidence with focal-plane γ rays at energies of 171 and 136 keV, respectively. The 5672-keV line in spectrum (c) is associated with ^{173}Ir [13].

The correlation of these α-decay lines with second-generation decay of ^{169}Os verifies that these three α lines come from ^{173}Pt. Hild *et al.* [12] observed three α-decay lines at energies of 5585 (this work gives 5581), 5537, and 5510 keV in ^{169}Os feeding the ground state of ^{165}W. In order to view α-α correlations, a matrix of correlated first- and second-generation α decays was created.

First-generation α decay was defined as the first α decay in a pixel after the implantation of an $A = 173$ recoil and restricted to those decays occurring within one second after the implant. The second-generation decay was constrained to a time window of ten seconds after the first-generation α decay was detected. A gate was placed on the second-generation α decay at energy of 5581 keV and the α lines at 6067, 6101, 6128, and 6232 keV in the parent nucleus can be clearly seen (Fig. 5.4(a)). This gives further assurance that all the new α lines observed in $A = 173$ recoils belong to ^{173}Pt. Further supporting evidence is provided by their similar half-lives. A detailed decay scheme (Fig 5.5) was constructed using the relationship between these alphas and their subsequent γ rays observed at the DSSD. The reader should refer to Table 5.1 for further information. Since no γ ray is detected in coincidence with the 6128-keV alpha, the 108-keV state likely feeds the α-decaying state ^{169}Os via an $E1$ transition.

5.3.2 ^{175}Ir Alpha Decays

Fig. 5.1(b) displays the α spectrum associated with $A = 175$ recoils and is constrained for α particles emitted within a time window of one to five sec following an implantation of a recoil in the same pixel of the DSSD. The α-decay lines at 6037, 5963 and 5830 keV are identified with ^{175}Pt because they are correlated with their daughter ^{171}Os α decay at 5250 keV, and because the 5963- and 5830-keV alphas feed excited states in the daughter nucleus at 77 and 211 keV, respectively [18, 81]. These states were previously observed in ^{171}Os [85]. Our measurement of ^{175}Pt α-decay energies and half-lives are consistent with previous measurements [80] (see Table 5.1). Furthermore, their RDT spectra, which display in-beam structures of ^{175}Pt [88], also support this assignment.

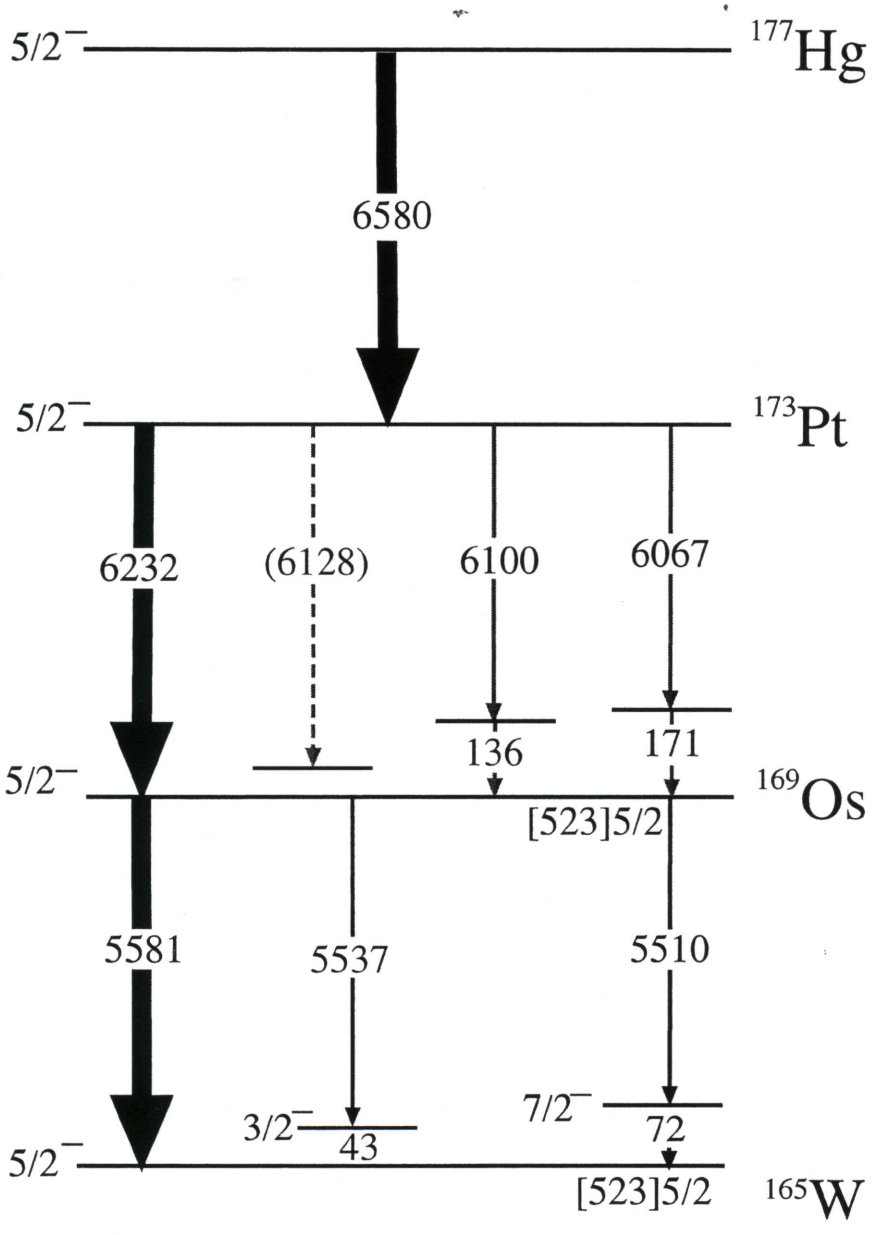

Figure 5.5: The α-decay scheme for ^{177}Hg. All energies in keV; energies less than 300 keV are those of γ rays in coincidence with α particles. All energy values shown are from this work.

Table 5.1: Alpha-decay measurements of Hg to Os nuclei obtained from the present work.

Nucl.	I^π	$E_{\alpha 1}$ (keV)	$T_{1/2}$ (s)	I^a_{rel} (%)	E^b_γ (keV)	$E_{\alpha 2}$ (keV)	b_α	δ^2 (keV)	F_α
^{178}Hg	0^+	6429	284(23)			6040	97(3)[1]	88(9)	1
^{177}Hg	$(\frac{5}{2}^-)$	6580	128(23)			6232,6128 6100,6067	(85)[2]	49(10)	1.7(4)
^{176}Hg	0^+	6755	22(1)			6317	98(2)[1]	81(5)	1
^{175}Hg		6879	15(1)			6455	100[c]	49(6)	1.7(5)
^{174}Hg	0^+	7071	2(1)[4]			6545	100[c]	85(40)	1
^{177}Au	$\frac{11}{2}^-$	6121	1180(30)			5672			
	$(\frac{1}{2}^+,\frac{3}{2}^+)$	6158	1462(32)			5418			
^{176}Au	(9^+)	6080*	1376(26)	26(2)	212.0	5830			
	(9^+)	6117*	1362(25)	49(3)	175.0	5830			
	(9^+)	6220[c]	1333(31)	21(2)	Irx	5830			
	(9^+)	6287[d]		<4		5830			
	(3^-)	6282	1046(11)	(100)		5520			
^{175}Au	$\frac{11}{2}^-$	6431	143(8)			5950	94(6)[1]	68(18)	

Table 5.1 (continued).

Nucl.	I^π	$E_{\alpha 1}$ (keV)	$T_{1/2}$ (ms)	I^b_{rel} (%)	E^c_γ (keV)	$E_{\alpha 2}$ (keV)	b_α	δ^2 (keV)	F_α
^{174}Au	(9^+)	6433*	162(4)	29(2)	191.2	6088			
	(9^+)	6471*	171(7)	32(3)	153.2	6088			
	(9^+)	6548[d]	160(5)	35(3)		6088			
	(9^+)	6618[d]	163(2)	<4		6088			
	(3^-)	6547[d]				5815			
^{173}Au	$\frac{11}{2}^-$	6742	14(1)			6119	92(13)[4]	56(9)	
	$(\frac{1}{2}^+)$	6690	25(1)			6005	94(19)[4]	48(10)	
^{177}Pt	$\frac{5}{2}^-$	5521	9(1)s						
^{176}Pt	0^+	5747	5.8(3)s	98(7)		5109			
	0^+	5519		< 2	227.1	5109			
^{175}Pt	$\frac{7}{2}^-$	6037	2277(17)	23(1)		5252			
	$\frac{7}{2}^-$	5693	2211(7)	75(1)	76.8	5252			
	$\frac{7}{2}^-$	5830	2272(34)	2(1)	76.8,134.1 221.4	5252			
^{174}Pt	0^+	6040	857(5)	99(1)		5410	74(3)	108(5)	
	0^+	5762*		< 1	286.7				

Table 5.1 (continued).

Nucl.	I^π	$E_{\alpha 1}$ (keV)	$T_{1/2}$ (ms)	I^b_{rel} (%)	E^c_γ (keV)	$E_{\alpha 2}$ (keV)	b_α	δ^2 (keV)	F_α
^{173}Pt	$(\frac{5}{2}^-)$	6232	382(2)	96(1)		5581,5537	82(6)	47(2)	2.3(2)
	$(\frac{5}{2}^-)$	6128*	400(11)	~2		5581,5537	<2	2.9(4)	37(7)
	$(\frac{5}{2}^-)$	6100*	392(15)	~1	136.2	5581,5537	<1	1.9(4)	56(18)
	$(\frac{5}{2}^-)$	6067*	411(19)	~1	171.2	5581,5537	<1	2.4(3)	45(12)
^{172}Pt	0^+	6317				5676	94(6)	107(5)	1
^{171}Pt		6455					96(5)	64(7)	1.5(1)
^{170}Pt	0^+	6545					98(4)	84(4)	1
^{175}Ir	$\frac{9}{2}^-$	5395	8(1)s				0.9(3)[5]	29(10)	
	$(\frac{5}{2}^-)$	5745*	4.9(4)s						
^{173}Ir	$\frac{11}{2}^-$	5672	2105(47)		136.4		14(3)	75(20)	
	$(\frac{1}{2}^+,\frac{3}{2}^+)$	5418	10(1)s			5060	4(2)	92(47)	
^{172}Ir	(8^+)	5830	2264(47)		136.3		22(6)	35(10)	
	(3^-)	5520			122.7		< 2	36(19)	
^{171}Ir	$\frac{11}{2}^-$	5950	8.1(9)		92.1		85(2)	52(5)	
^{170}Ir	(8^+)	6088	818(31)				39(6)	15(3)	
	(3^-)	5815							

Table 5.1 (continued).

Nucl.	I^π	$E_{\alpha 1}$ (keV)	$T_{1/2}$ (ms)	I^b_{rel} (%)	E^c_γ (keV)	$E_{\alpha 2}$ (keV)	b_α	δ^2 (keV)	F_α
^{169}Ir	$\frac{11}{2}^-$	6118	295(7)				74(3)	64(4)	
	$(\frac{1}{2}^+,\frac{3}{2}^+)$	6008	0.8(3)s				50(7)	43(17)	
^{172}Os	0^+	5109	20(2)s				1.4(3)	173(43)	1
^{171}Os		5252	9.1(8)s				2(1)	107(24)	1.3(6)
^{170}Os	0^+	5410	7.2(2)				10(3)	113(34)	1
^{169}Os	$(\frac{5}{2}^-)$	5581	4.1(4)s				12(3)	43(11)	2.2(9)
	$(\frac{5}{2}^-)$	5537							
^{168}Os	0^+	5681	2.6(2)s				36(4)	80(11)	1

* New α-decay line.

$E_{\alpha 1}$ and $E_{\alpha 1}$ correspond to first- and second generation alphas, respectively and are accurate within 5 keV except [d] within 10 keV.

b_α and δ^2 correspond to α-decay branching ratio and reduced width, respectively.

[a] The intensities are obtained from Fig. 1.

[b] γ rays that are in coincidence with first-generation alphas and accurate within 0.5 keV.

[c] "Sum" α line; summing contribution due to K-conversion electrons from the 175- and 212-keV transitions in ^{172}Ir.

[d] "Sum" α line; summing contribution due to K-conversion electrons from the 153-keV transition in ^{170}Ir.

Previous α-decay measurements can be obtained from Refs. [13, 18, 80, 81, 82].

[1,2,3,4,5] from Refs. [13, 80, 82, 86, 106].

One could assume that the α line at 5745-keV may belong to ^{176}Pt because of similar energy. The presence of $A = 176$ recoils in the $A = 175$ spectrum may be due a small overlap of adjacent mass peaks. However, the measured half-life of 5.1 (3) s for the 5745-keV α is slightly smaller than the half-life of ^{176}Pt (current work gives $T_{1/2} = 5.8$ (3) ms). This may indicate that the 5745-keV α belongs to some other $A = 175$ nucleus. In order to correctly identify this α line, a RDT spectrum of this α was taken and is shown in Fig. 5.6(b). In order to verify that these γ rays are not random coincidences, a background spectrum is taken, shown in Fig. 5.6(c). Comparison of the two spectra indicates that some of the peaks in part (b) result from real coincidences. The background-subtracted RDT spectrum shown in Fig. 5.7(a) contains γ rays identified with in-beam structures of ^{175}Ir (Fig. 5.8). Thus, this new α line is associated with ^{175}Ir decay. The α line at 5395 keV is also associated with ^{175}Ir because of its RDT spectrum. This α line was previously observed by Schmidt-Ott [13] and our measured half-life of 8.1(5) s is in agreement with that work.

The RDT spectrum of the 5250-keV α shows transitions in ^{175}Pt and this would indicate that it belongs to ^{175}Pt. However, this assignment is unlikely, based on the systematics of α energies. Also if this α particle decays from the ground state of ^{175}Pt, one would expect a fine-structure γ ray at $\sim$724 keV in the daughter nucleus, but no such transition is found. This α is likely the daughter decay line because it matches ^{171}Os energy and half-life. The presence of $A = 171$ daughter α line in the mass 175 α spectrum is likely due to the non-detection of the parent α decay by the DSSD. At the moment, the α-decay lines at 5116 and 5515 keV cannot be identified. It is likely that these lines are associated with $A = 175$ or 171 recoils.

5.4 Discussion

5.4.1 ^{177}Hg Alpha-Decay Chain

Previous work by Kondev *et al.* [9] observed only one α-decay line in ^{179}Hg at an energy of 6286 keV. These authors observed the correlation between this α-decay line with daughter (^{175}Pt) lines at 5830, 5963, and 6037 keV. The strongest α line at 5963

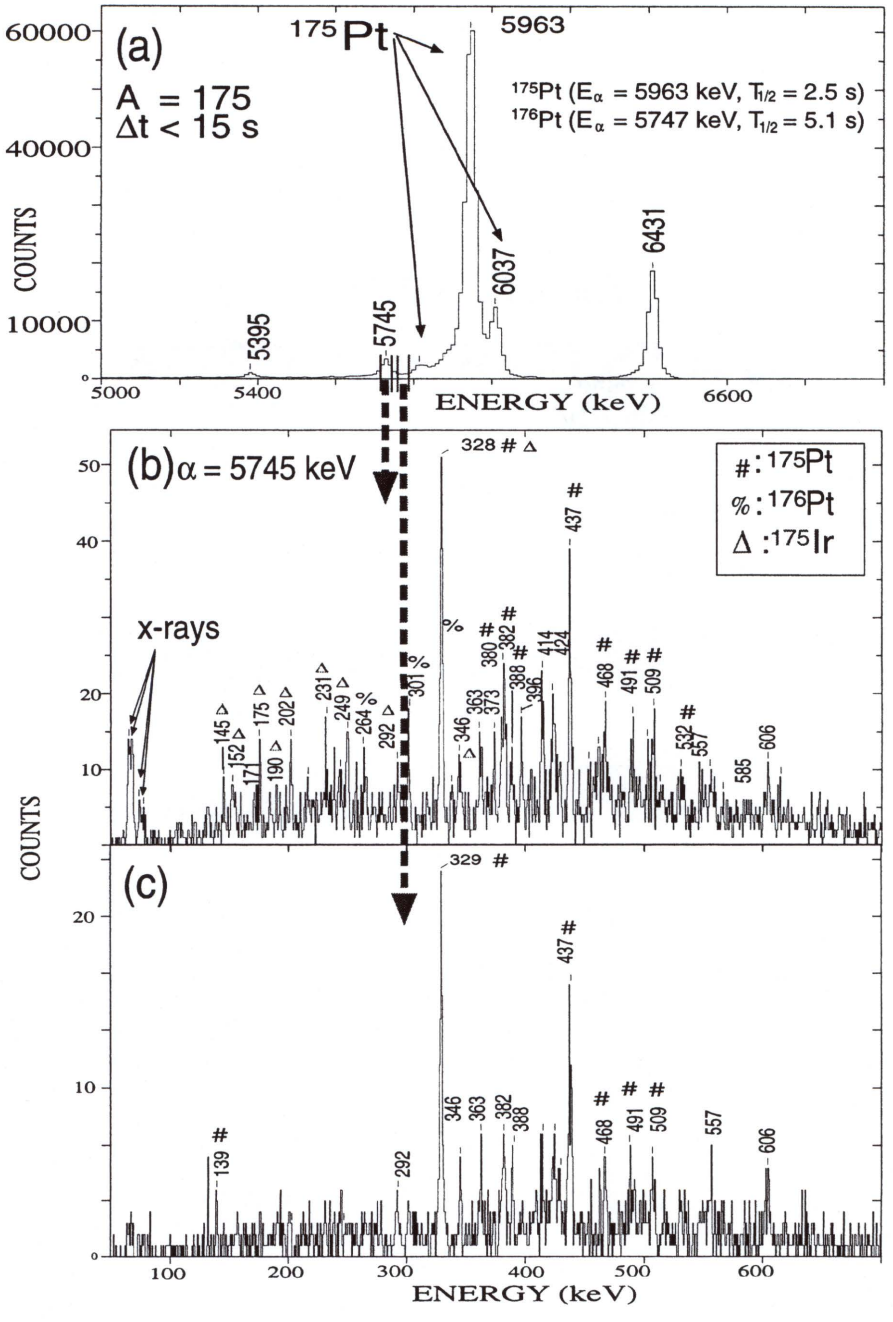

Figure 5.6: Taking RDT gate on the $A = 175$ α-decay line at 5745 keV. Part (a) shows the $A = 175$ α spectrum time-cut from 0 to 15 s. The arrows indicate the RDT gates placed on the (b) 5745-keV α-decay line and (c) background to generate γ-ray spectra.

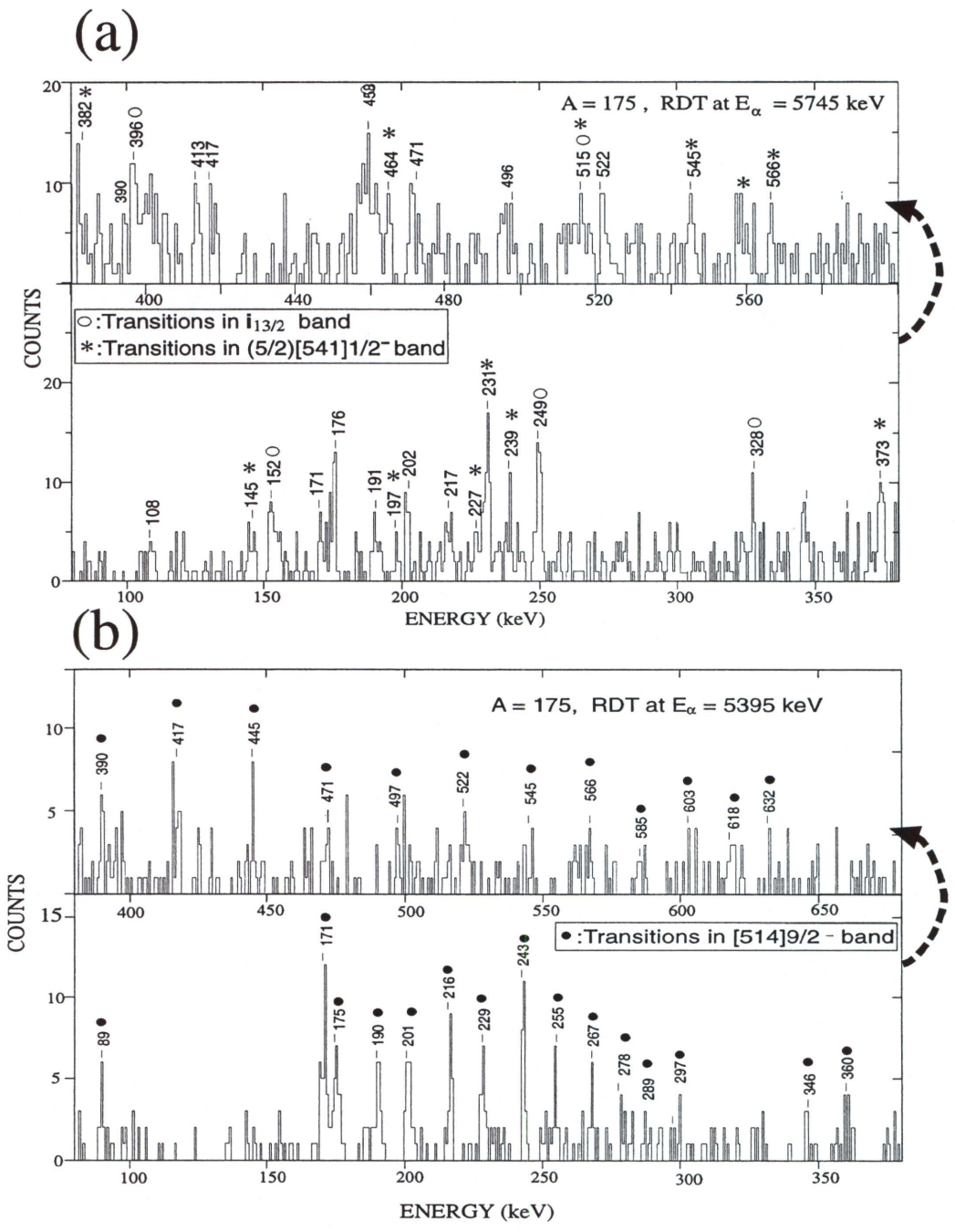

Figure 5.7: Background-subtracted prompt γ rays emitted by ^{175}Ir which subsequently emitted the (a) 5745- and (b) 5395-keV α particles.

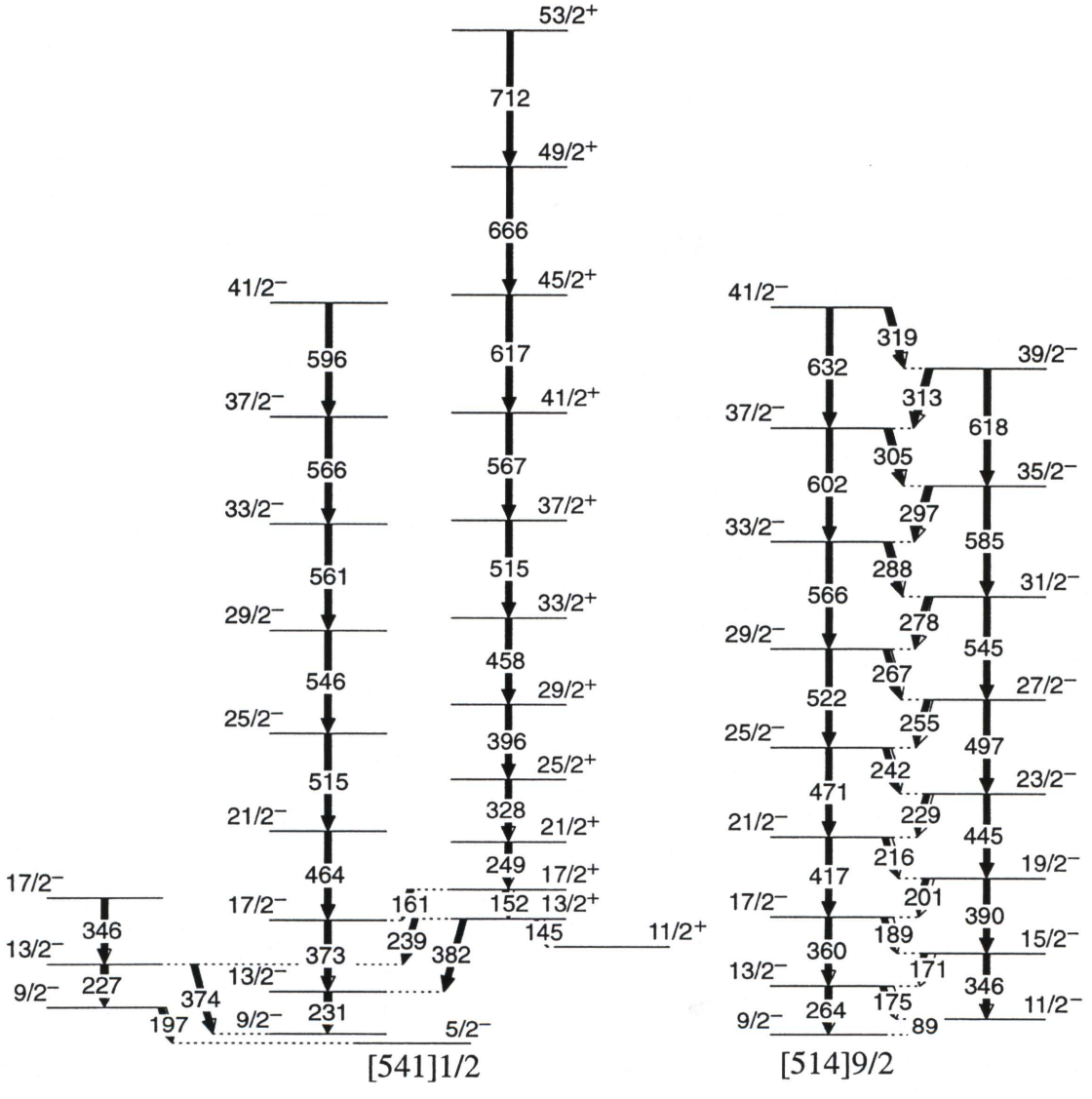

Figure 5.8: The level scheme of ^{175}Ir. All energies are in keV; reproduced from Ref. [95, 96] (See also Table 5.2).

Table 5.2: Possible configuration assignments for the α-decaying states in odd-A nuclei.

$\downarrow P \mid N \rightarrow$						
$^{172}_{80}Hg_{92}$	$^{173}_{80}Hg_{93}$	$^{174}_{80}Hg_{94}$	$^{175}_{80}Hg_{95}$	$^{176}_{80}Hg_{96}$	$^{177}_{80}Hg_{97}$ $[512]\frac{5}{2}$	$^{178}_{80}Hg_{98}$
$^{171}_{79}Au_{92}$ $[505]\frac{11}{2}$ $[400]\frac{1}{2}$	$^{172}_{79}Au_{93}$	$^{173}_{79}Au_{94}$ $[505]\frac{11}{2}$ $[400]\frac{1}{2}$	$^{174}_{79}Au_{95}$	$^{175}_{79}Au_{96}$ $[505]\frac{11}{2}$ $([411]\frac{1}{2})$	$^{176}_{79}Au_{97}$	$^{177}_{79}Au_{98}$ $[505]\frac{11}{2}$ $d_{3/2}$
$^{170}_{78}Pt_{92}$	$^{171}_{78}Pt_{93}$	$^{172}_{78}Pt_{94}$	$^{173}_{78}Pt_{95}$ $[512]\frac{5}{2}$	$^{174}_{78}Pt_{96}$	$^{175}_{78}Pt_{97}$ $[503]\frac{7}{2}([514]\frac{7}{2})$	$^{176}_{78}Pt_{98}$
$^{169}_{77}Ir_{92}$ $[505]\frac{11}{2}$ $([411]\frac{1}{2})$	$^{170}_{77}Ir_{93}$	$^{171}_{77}Ir_{94}$ $[505]\frac{11}{2}$	$^{172}_{77}Ir_{95}$	$^{173}_{77}Ir_{96}$ $[505]\frac{11}{2}$ $d_{3/2}$	$^{174}_{77}Ir_{97}$	$^{175}_{77}Ir_{98}$ $[514]\frac{9}{2}$
$^{168}_{76}Os_{92}$	$^{169}_{76}Os_{93}$ $[523]\frac{5}{2}$	$^{170}_{76}Os_{94}$	$^{171}_{76}Os_{95}$ $[523]\frac{5}{2}$	$^{172}_{76}Os_{96}$	$^{173}_{76}Os_{97}$ $[523]\frac{5}{2}$	$^{174}_{76}Os_{98}$
$^{167}_{75}Re_{92}$ $[514]\frac{9}{2}$ $([411]\frac{1}{2})$	$^{168}_{75}Re_{93}$	$^{169}_{75}Re_{94}$ $[514]\frac{9}{2}$ $d_{3/2}$	$^{170}_{75}Re_{95}$	$^{171}_{75}Re_{96}$ $[514]\frac{9}{2}$	$^{172}_{75}Re_{97}$	$^{173}_{75}Re_{98}$ $[514]\frac{9}{2}$
$^{166}_{74}W_{92}$	$^{167}_{74}W_{93}$ $[523]\frac{5}{2}$	$^{168}_{74}W_{94}$	$^{169}_{74}W_{95}$ $[523]\frac{5}{2}$	$^{170}_{74}W_{96}$	$^{171}_{74}W_{97}$ $[523]\frac{5}{2}$	$^{172}_{74}W_{98}$

keV in ^{175}Pt feeds an excited $7/2^-$ state at 77 keV in ^{171}Os. Based on the α decay and in-beam studies by Hild *et al.* [12] and Bark *et al.* [85], the ground state of ^{171}Os was assigned the Nilsson configuration of [523]5/2 (see also Table 5.2).

Since the most intense α-decay line of ^{175}Pt feeds an excited $7/2^-$ state, the ground state of ^{175}Pt is assigned the spin and parity of $7/2^-$. Therefore, the ground-state assignment of ^{179}Hg is likely $I^\pi = 7/2^-$ since the 6286-keV α particle feeds the ground state of ^{175}Pt. Kondev *et al.* [9] postulated that the $7/2^-$ ground state in ^{175}Pt and ^{179}Hg are likely mixed Nilsson levels $\nu h_{9/2}$ [514]7/2 and $\nu f_{7/2}$ [503]7/2. The decay chain of ^{179}Hg is shown in Fig. 5.9.

A search for similar structure in ^{177}Hg was performed. In order to study this decay chain, two reactions, ^{96}Mo(^{84}Sr, 2n) at 390 and 395 MeV and ^{94}Mo(^{84}Sr, 2pn) at 380 and 385 MeV, were used. The first reaction was used to populate ^{177}Hg while the later one to create ^{173}Pt. The creation and α decay study of ^{173}Pt was discussed in the earlier section. Fig. 5.10(a) displays the $A = 177$ α-decay spectrum within a time window of less than 500 ms following an implantation of the recoiling nucleus in the same pixel of the DSSD. The α peaks at 6121 and 6158 keV are associated with ^{177}Au because they are correlated with the previously observed daughter decay in ^{173}Ir [13] and their RDT spectra display γ-ray structures observed in ^{177}Au [11]. The 6580-keV α-decay line is assigned to ^{177}Hg and the measured half-life of 128(4) ms is in good agreement with previous measurements [89, 90].

To have further verification that this 6580-keV α-decay line belongs to ^{177}Hg, the correlation with the daughter ^{173}Pt decay was studied. A matrix of first- and second-generation α decays was made. Time windows of 500 ms and 1.5 s were required for the first- and second-generation α decays in order to reduce accidental coincidences. From this matrix, the 6580-keV α line was found to be correlated with four daughter α-decay lines at 6232, 6128, 6100, and 6067 keV (see Fig. 5.10(b)). These α lines belong to ^{173}Pt. The correlation of the 6128-, 6100-, and 6067-keV α peaks with the 6580-keV ^{177}Hg α line gives further assurance that these α peaks, which are new, do indeed belong to ^{173}Pt.

From our current data, we observed only one α-decay line associated with ^{177}Hg. No γ ray was found in coincidence with this ^{177}Hg α at the focal plane of the

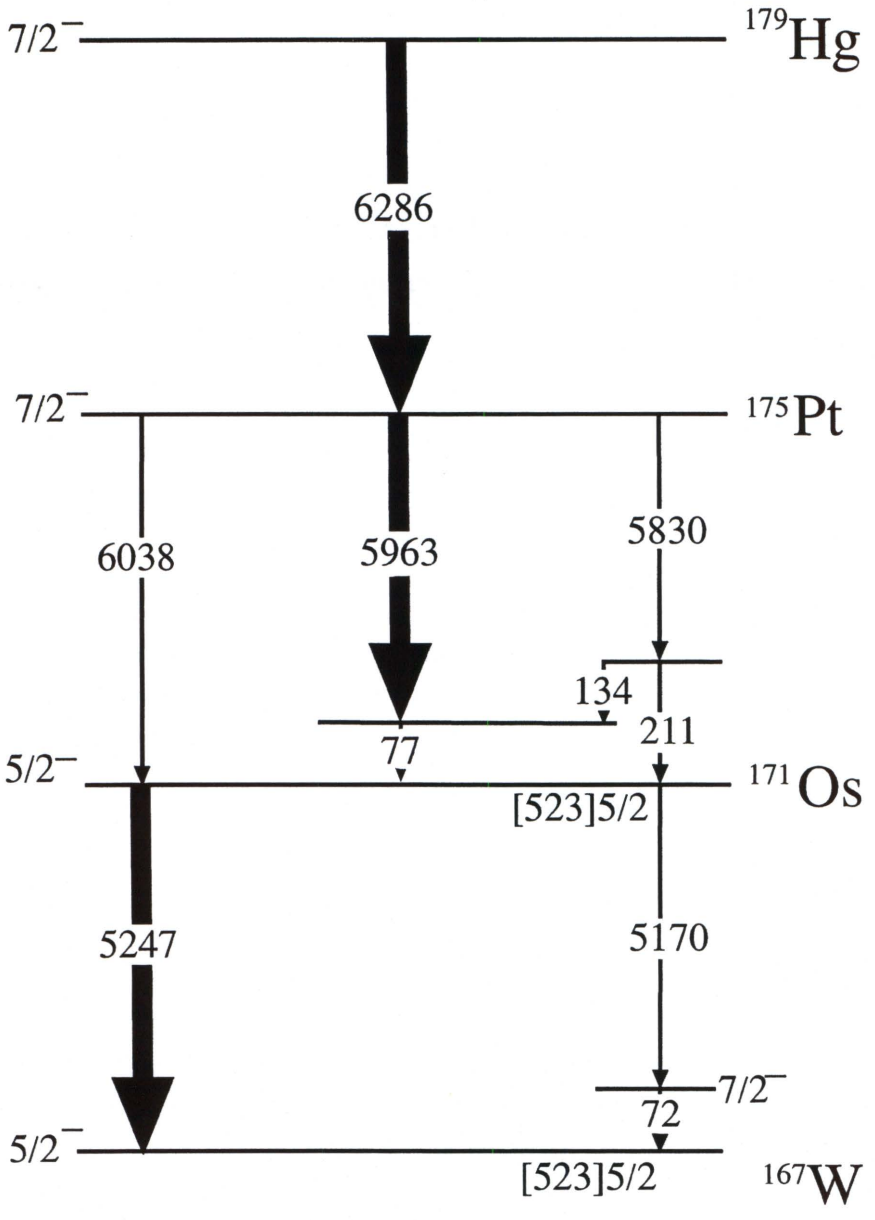

Figure 5.9: The α-decay scheme for ^{179}Hg. All energies in keV; energies less than 300 keV are those of γ rays in coincidence with α particles. All energy values shown here are from this work.

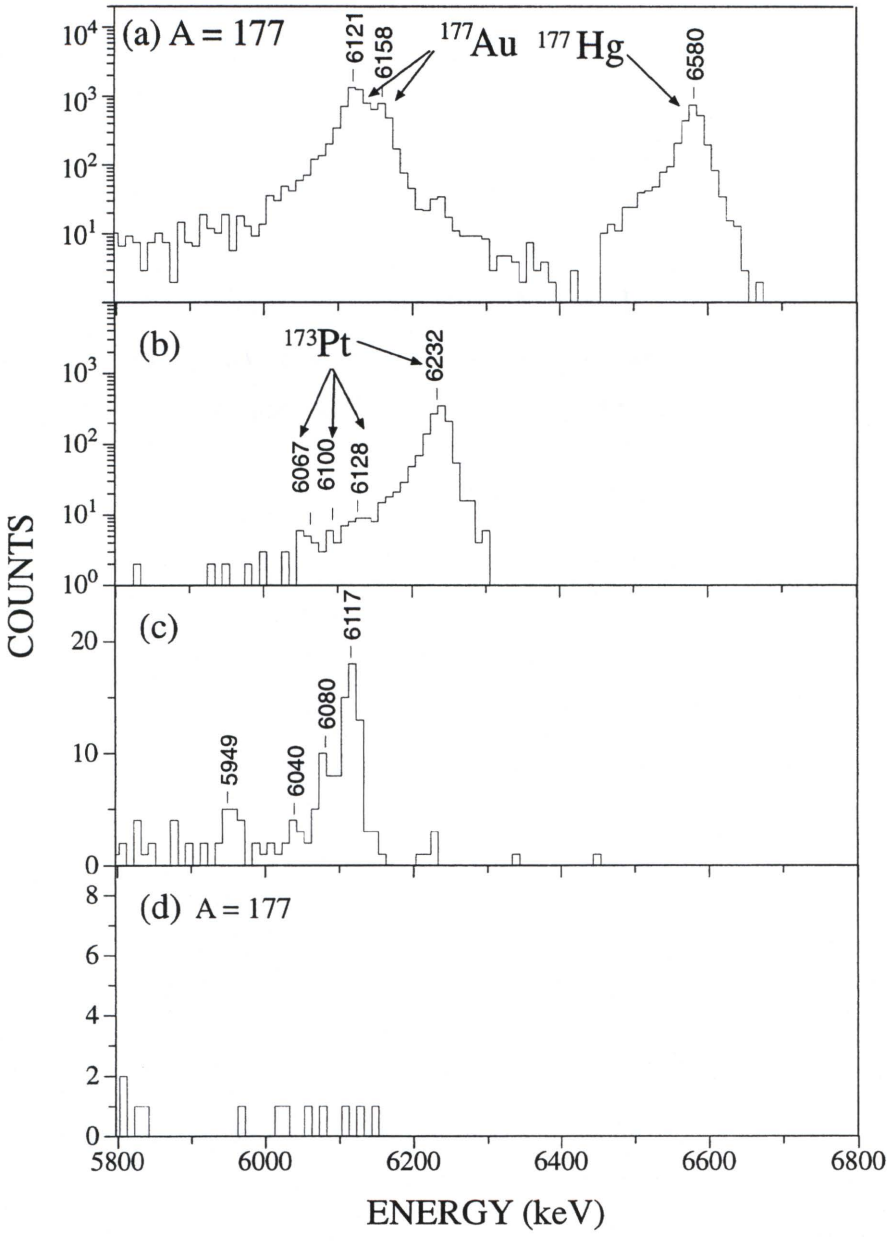

Figure 5.10: Spectra displaying ^{177}Hg α-decay properties. (a) $A = 177$ α-decay lines detected within 500 ms following an implantations at the DSSD. (b) Daughter decay lines which are in coincidence with the 6580-keV ^{177}Hg α-decay line. (c) Spectrum of all α particles emitted in the DSSD in coincidence with γ rays. (d) Same as part (c), except mass-gated at $A = 177$. All α-decay lines are produced in the ^{96}Mo + ^{84}Sr $\rightarrow$ ^{180}Hg reaction.

FMA as shown in Fig. 5.10(c) and (d). These spectra show that there is no α-decay line above 6500 keV which is in coincidence with γ rays detected at the focal plane of the FMA. This would indicate that the ^{177}Hg α-decay line at 6580 keV populates the ground state in the daughter nucleus.

With this new α-decay information, an α-decay scheme for ^{177}Hg was built and is illustrated in Fig. 5.5. However, there are some inconsistencies between α-decay work and high-spin studies of the nuclei shown in the decay chain. The ground-state of ^{165}W was assigned the Nilsson configuration of [523]5/2 by Hild *et al.* [12] based on α and β studies. From high-spin studies of ^{165}W, Simpson *et al.* [91] found that the lowest observed state in ^{165}W has $I^{\pi} = 13/2^{+}$.

In ^{169}Os, a $9/2^{-}$ state was observed by Carpenter *et al.* [92] to be lowest in energy. The difference in energy between this state and the $13/2^{+}$ isomeric state is 81 keV [92]. The γ-ray structure of this nucleus is similar to ^{167}W [18]. In the γ-ray study of ^{167}W, J. Gerl *et al.* [93] observed that the lowest energy state has a spin and parity of $7/2^{-}$. These authors indicated that the $7/2^{-}$ state is not likely the ground state. A ground state spin and parity of $5/2^{-}$ were suggested for ^{167}W. They proposed the ν[523]5/2 configuration. The same assignment for the ground state of ^{167}W was also proposed by Hild *et al.* [12] based on α- and β-decay studies. Therefore, it is likely that the ground states in ^{169}Os and ^{165}W have a spin and parity of $5/2^{-}$ based on the ν[523]5/2 configuration. The transition between the $9/2^{-}$ level and the $5/2^{-}$ ground state in ^{169}Os may not be observable and the same goes for ^{165}W.

Consequently, the ground states of both ^{173}Pt and ^{177}Hg are assigned $5/2^{-}$ since the strongest α line from these nuclei depopulates the daughter's ground state. However, in a recent γ-ray spectroscopy study of ^{173}Pt, the only in-beam structure observed was the $i_{13/2}$ band [86]. To further complicate matters, the in-beam study of ^{177}Hg by Melerangi *et al.* [94] showed a $E3$ γ transition decaying out of an $13/2^{+}$ state. Those authors proposed an $I^{\pi} = 7/2^{-}$ ground state for ^{177}Hg and suggested the configuration mixture of ν[503]7/2 and ν[514]7/2. As a result of the observation of this $E3$ transition coupled with the fact that the α decay of ^{177}Hg feeds the ground state of ^{173}Pt, the spin and parity of the ground state in ^{173}Pt is not $13/2^{+}$; it likely has negative parity. Assuming that $I^{\pi} = 5/2^{-}$ and the assignment of ν[523]5/2 for

the ground state in ^{165}W is correct, then all the ground states in the ^{177}Hg decay chain must be $5/2^-$. The $I^\pi = 5/2^-$ assignment for ^{173}Pt and ^{177}Hg ground state is reasonable because the $7/2^-$ ν orbitals are far from the Fermi surface in ^{165}W and ^{169}Os. The $I^\pi = 5/2^-$ ground state for both of these nuclei is likely attributed to the $\nu[512]5/2$. The possible configuration for ground states of ^{177}Hg, ^{173}Pt, ^{169}Os, and ^{165}W nuclei can be found in Table 5.2.

5.4.2 New ^{175}Ir α Line

In ^{173,177,179}Ir nuclei two alpha decaying states were known, one associated with a high-spin isomer and the other a low-spin state. Previous work on ^{175}Ir [13] identified only one α-decaying state that decays via a 5395-keV α particle. The previous authors [13] assigned a spin and parity of $5/2^-$ and a configuration of [541]1/2 to this state. This assignment was based on the β-decay feeding pattern of this nucleus. In that study, the authors reported a strong β feeding to the 105-keV state (73%) in ^{169}Os, which was assigned the orbital $\nu[633]7/2$, and also to a new state at 504 keV (22%). However, our RDT spectra for the 5395-keV and 5745-keV α-decay lines indicate otherwise.

From previous in-beam γ spectroscopy, Cederwall *et al.* [95] and Dracoulis *et al.* [96] identified the γ-ray sequences built upon the $\pi h_{9/2}$ [541]1/2 and $\pi h_{11/2}$ configurations (see Fig. 5.8). The RDT spectrum for the 5395-keV α particle displays only the transitions from the $\pi h_{11/2}$ [514]9/2 band while the 5745-keV α shows all the transitions associated with the $\pi h_{9/2}$ [541]1/2 and the $\pi i_{13/2}$ bands in ^{175}Ir. This would indicate that these α particles decay from two different states. The 5395-keV and 5745-keV α are reassigned in this work as decaying from the $\pi h_{11/2}$ [514]9/2 and the $\pi h_{9/2}$ [541]1/2 band heads, respectively. This distinction is clearly shown in Figs. 5.7(a) and (b). With this new information, an α decay scheme for ^{175}Ir shown in Fig. 5.11(d) was created.

5.4.3 ^{173,175,177}Au Alpha-Decay Chains

In this region, odd-A Au nuclei exhibit two α-decaying states, one associated with a low-spin and the other high-spin states. The high-spin states are usually associated

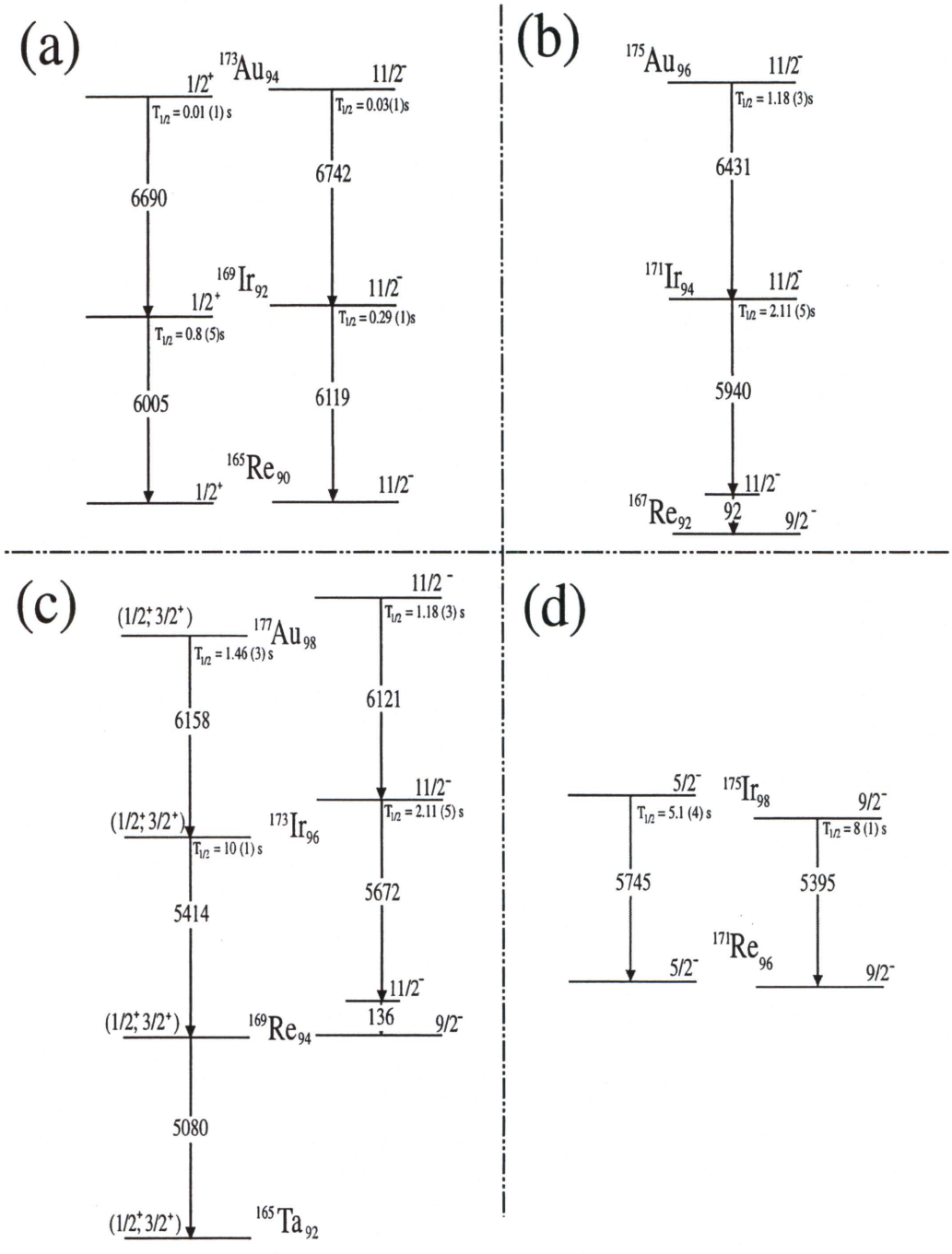

Figure 5.11: The α-decay schemes for ^{173,175,177}Au and ^{175}Ir. All energies in keV; energies less than 300 keV are those of γ rays in coincidence with α particles. All energy values shown here are from this work.

with orbitals originating from the $h_{11/2}$ sub-shell. It was pointed out by Kondev *et al.* [11] that the shape associated with the $h_{11/2}$ [505]11/2 evolves gradually from a triaxial shape in heavier ^{185}Au [97] to a near-spherical shape in ^{171}Au [98] as the neutron number decreases. However, in ^{171,173}Ir [73, 87] and ^{175}Ir [95], those authors proposed that the shapes associated with the $h_{11/2}$ [505]11/2 and $h_{11/2}$ [514]9/2 bands are trixial and "prolate," respectively.

Two α-decay lines that are observed at $E_\alpha = 6121$ and 6158 keV are associated with ^{177}Au. Kondev *et al* assigned the $I^\pi = 11/2^-$ and $(1/2^+,3/2^+)$ to states associated with the 6121 and 6158 keV α lines. These assignments [11] were based on the in-beam structures which are correlated with these respective α particles, and also from the limited decay work on ^{173}Ir [13] and parent ^{181}Tl [99].

In our data, the 6158-keV α line is observed to be correlated with daughter ^{173}Ir and granddaughter ^{169}Re at 5414 and 5083 keV, respectively. Previous work on ^{169}Re [104] identified two α peaks at 5060 and 4070 keV. Our value of 5083 keV is clearly about 20 keV higher than previously reported values. In the data, we observed two α peaks (at 5040 and 5083 keV) which are very close to each other. The previously reported 5060-keV line is likely a doublet. The current data seem to indicate that the 5040-keV line is likely random coincidences of some other long life nucleus. Therefore we reassigned the alpha at 5083-keV to ^{169}Re and assigned the spin of $(1/2^+,3/2^+)$ to this state. The 6158-keV alpha in ^{177}Au is observed to be correlated with the daughter line at 5672 keV. The 5672-keV alpha is in coincidence with an $M1$ 136-keV γ transition in ^{169}Re. The 136-keV γ ray is observed in the in-beam structure of ^{169}Re where it populates a $9/2^-$ bandhead. Thus, a spin of $11/2^-$ is assigned to the high-spin isomer in ^{173}Ir. This assignment also agrees with previous work. The decay chains of ^{173,175,177}Au are shown in Fig. 5.11.

However in ^{175}Au, only one α-decaying state was observed, which was assigned an 11/2 state. Our data show its α decay at 6430 keV is correlated with a 5940-keV alpha in daughter ^{171}Ir. The 5940-keV α particle feeds an excited 11/2 state at 91 keV above the 9/2- isomer in ^{167}Re. Recently, Rowe *et al.* [89] observed a weak 5720 keV α in ^{171}Ir that correlated with a 6420 keV α in ^{175}Au. From the first- and second-generation correlation, we did not see any evidence for the correlated 5720

keV alpha.

5.4.4 Reduced Width and Hindrance Factor

The dependence of the α-decay rates on nuclear structure is contained in the reduced width (δ^2). It is defined as the ratio of the α-decay transition probability to the potential penetration barrier factor. In order to obtain this quantity, the α-decay energy, half-life, and the branching ratio are required. The δ^2 values of nuclei studied in this experiment can be found in the eighth column of Table 5.1 and were deduced using the Rasmussen [35] formalism. From this table, one can see that the δ^2 of the odd-A Pt and Os nuclei are approximately a factor of two smaller than the neighboring even-even isotopes, while for odd-odd ^{170,172}Ir nuclei, they are approximately 30% of the value of even-even neighbors. This trend was observed by previous investigators [4, 101] and they attributed this to the differences in pairing correlations between even-even-nuclei and odd-A isotopes.

As discussed in sec. 2.10.3, the hindrance factor of α decays from even-even nuclei are set to unity. The hindrance factor for an odd-A nucleus such as Pt or Os is defined as the ratio of the average value of δ^2 for its even-even neighbors over its δ^2 value. The values obtained for the dominant α transitions from these odd-A Pt and Os agree with the results of $F_\alpha \sim$ 1.2-3.0 for favored transitions of the deformed odd-A nuclei in the $A = 240$ region [101].

5.4.5 Systematics of Odd-A Alpha-Decaying Nuclei

Fig. 5.12 displays the α-decay energy of Ir and Au nuclei as a function neutron number. From this plot, one can see that the Q values for the decay of the $h_{11/2}$ shell in Au and Ir differ by approximately 1 MeV. The figure also shows the difference in Q values for low-spin decay and high-spin decay is larger in Ir than in Au nuclei. The reassignment of the 5395-keV α in ^{175}Ir from $\pi h_{9/2}$ [541]1/2 to π $h_{11/2}$ [514]11/2 gives an improved agreement with these systematic trends. This plot, it indicates that the α-decay line at 5011 keV in ^{177}Ir should be reassigned to the $h_{11/2}$ shell configuration rather than $\pi h_{9/2}$ [541]1/2 [18]. This reassignment should be verified

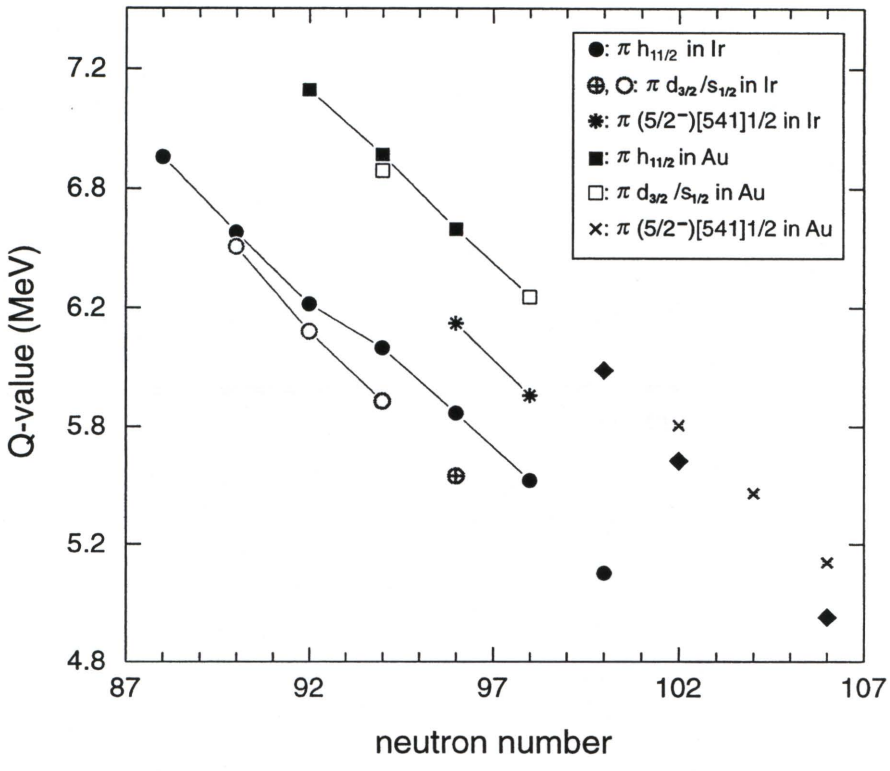

Figure 5.12: Systematics of Q value in Ir and Au nuclei as a function of neutron number. The data for $N > 99$ can be obtained from Refs. [18, 80], while their configuration assignments are tentative.

in a future experiment. This plot can also be used to predict the proximity of the α-decay energies yet to be observed.

5.4.6 Unknown α Decays

From this experiment, we found a number of α particles which could not be identified. Many of these α-decay lines are weak and some are in coincidence with γ rays observed at the focal plane of the FMA. Therefore we put them in Table 5.3 for future investigations.

Table 5.3: Unidentified Alpha-decay lines obtained from the present work.

Compound nucleus	Mass	$E_{\alpha 1}$ (keV)	E_{γ}^{b} (keV)
^{178}Hg		5527	510
^{178}Hg		5649	391
^{178}Hg		5657	314
^{178}Hg		5829	131
^{178}Hg		5833	196
^{178}Hg		5959	83,510
^{178}Hg		6093	196
^{178}Hg	175	5116	
^{178}Hg	175	5515	
^{178}Hg	175	6627	
^{176}Hg	173	5170	
^{176}Hg	173	5100	
^{176}Hg	173	5806	
^{176}Hg	173	5958	
^{176}Hg	173	6038	

CHAPTER 6

Experimental Results in ^{174,176}Au and ^{172}Ir

6.1 Overview

The α-decay properties of the neutron-deficient nuclei ^{174,176}Au have been previously studied by a number of investigators. However, there are inconsistencies in the identification and measurement of the alpha energies and half-lives. In ^{174}Au, two α lines were observed by Schneider *et al.* [82] and confirmed by Page *et al.* [81]. However, Rowe *et al.* [89] assigned a different α line to ^{174}Au based on the decay of ^{178}Tl. Cabot *et al.* [18, 102] identified two α lines in ^{176}Au and assigned them to a single decaying state. The β decay of ^{176}Au [103] and isomeric nature of its daughter ^{172}Ir seems to give a hint of isomerism in ^{176}Au. This work provides new data on the α lines and the properties of the decaying states which are associated with these odd-odd gold nuclei, settles the inconsistencies of previous measurements, and proposes quasiparticle configurations for the observed states.

6.2 Experimental Details

The odd-odd ^{174,176}Au nuclei were produced in the ^{92}Mo(^{84}Sr,pn) reaction at 390 and 395 MeV and ^{94}Mo(^{84}Sr,pn) at 380 and 385 MeV, respectively. The anaylzing methods used in ^{173}Pt and ^{175}Ir are applied for these odd-odd nuclei (see sec. 5.2).

6.3 Analysis of ^{174,176}Au and ^{172}Ir

6.3.1 ^{176}Au Alpha Decay

Fig. 6.1(a) displays the α-decay spectrum associated with $A = 176$ recoils in which a time window of less than 4 s following an implantation of the recoiling nucleus in the

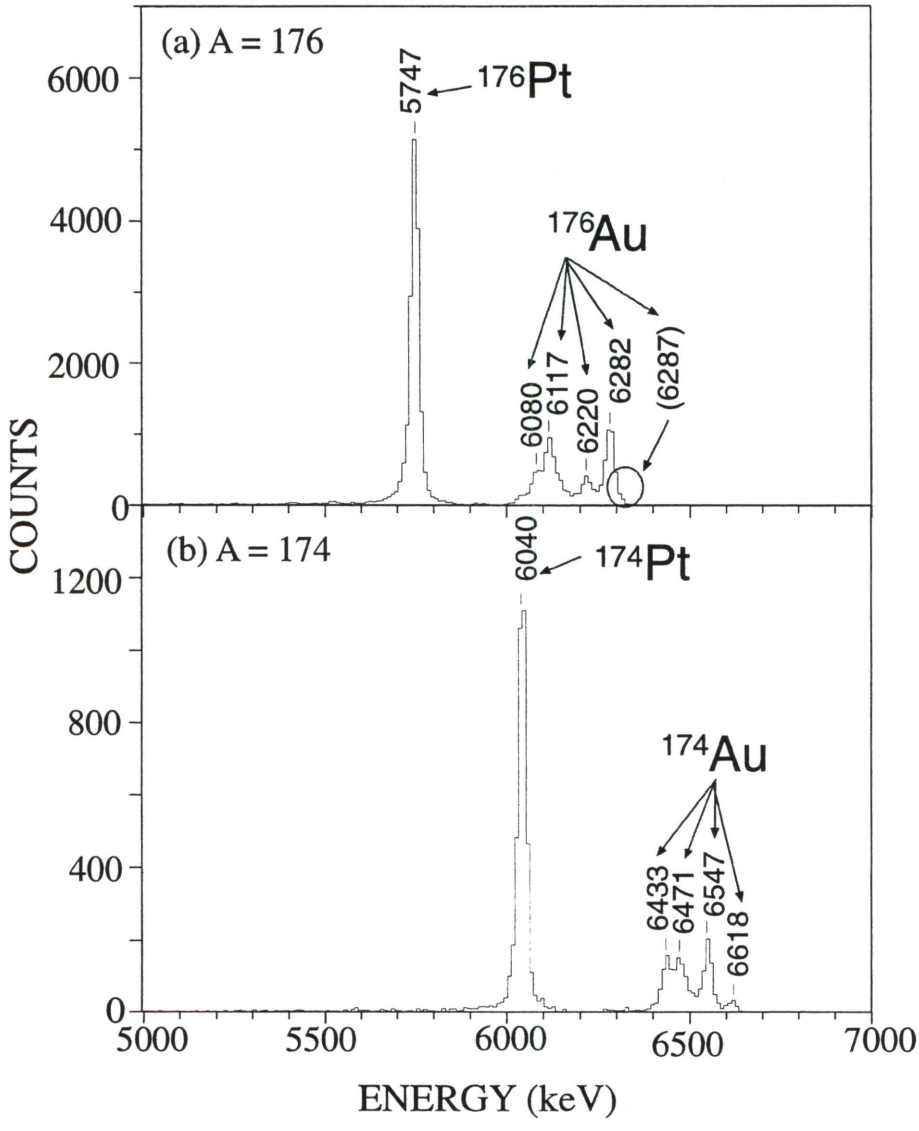

Figure 6.1: Spectra of $A = 176$ and $A = 174$ α-decay lines. Mass-gated α-decay lines from (a) $A = 176$ recoils detected within four seconds following an implantation of a recoiling reaction product into the DSSD and (b) $A = 174$ recoils detected within a time interval of one second following an implantation at the DSSD.

same pixel of the DSSD was imposed. The largest peak in Fig. 6.1 has an energy of 5747(5) keV and is associated with the decay of ^{176}Pt [81]. Our measured energies and half-lives of these Pt α decay lines are consistent with previously published results, as summarized in Table 5.1. Two α decay lines at energies of 6228(5) and 6286(5) keV were previously assigned to ^{176}Au [18, 82, 102]; the intensity of the 6228-keV alpha was reported to be much larger than that of the 6286-keV α line. Inspecting Fig. 6.1, if our 6220(5) and 6282(5) keV α are the same lines, one observes a clear difference with the previous results, since the 6282-keV line is clearly more intense than the 6220-keV peak in the present experiment. Furthermore, Cabot *et al.* [18, 102] reported that the 6228- and 6286-keV α peaks originate from the same state, but our measured half-lives do not support their conclusion (see below).

After the α decays of ^{176}Au, its daughter nucleus ^{172}Ir [13] subsequently α decays with known lines (these are called the second-generation α decays). Since each of the DSSD events was time stamped and the half-lives of ^{176}Au and ^{172}Ir are known, a matrix of correlated first- and second-generation α decays was made. This matrix was used to verify the placement of the remaining α-decay lines. First-generation α decays were restricted to $A = 176$ recoils and detection within five seconds following a recoil implantation at the DSSD. Alpha particles detected in a pixel within ten seconds of first-generation α decay were identified as second-generation alphas.

Previous work [13] on the daughter, ^{172}Ir, identified two α-decay lines; where each is associated with a different state. Our new measurement of these α lines give their energies at 5830(5) and 5520(10) keV (see Table 5.1). These new values are consistent with the previous work [13]. The 5520-keV α peak is associated with the ground state while the α-decay line at 5830 keV is identified with a high-spin isomeric state. Because of an observed correlation with the 5830-keV α in ^{172}Ir, we associate the α-decay lines at 6080(5), 6117(5), and 6220(5) keV with the decay of ^{176}Au. The correlated spectra are shown in Figs. 6.2(a)-(c) where gates were placed on these three alphas and the ^{172}Ir decay can be clearly observed. Furthermore, we observed an α line at 5830 keV that is correlated with the 6282-keV α. While the 6282-keV α is associated with the ground-state decay (see below), we have tentatively assigned another line at 6287 keV to the decay of the high-spin isomer of ^{176}Au.

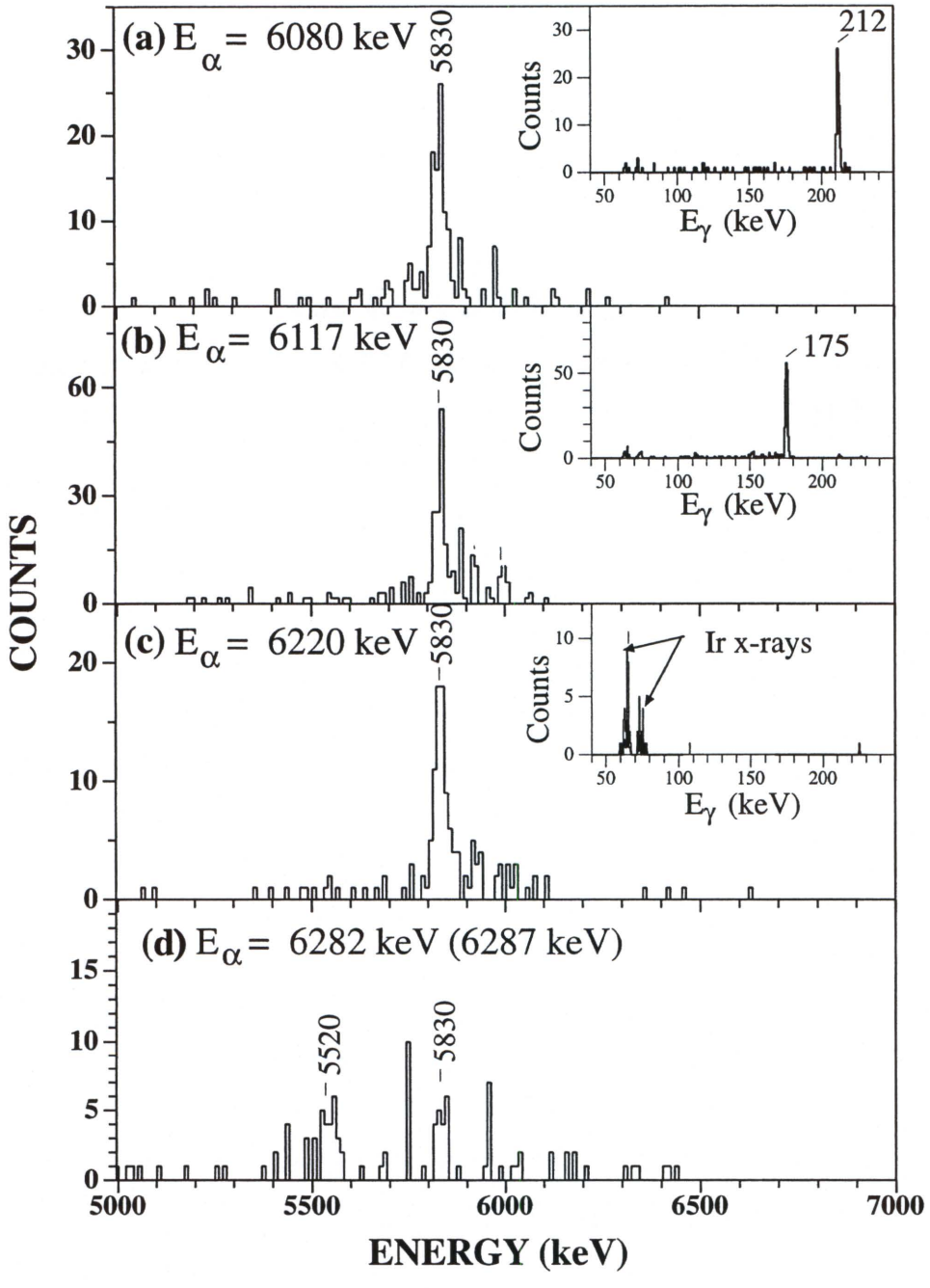

Figure 6.2: Spectra of second-generation alphas emitted within 10 seconds after emission of four lines detected within four seconds after an implantation of $A = 176$ recoils. The inserts show γ rays detected at the focal plane of the FMA which are in coincidence with the respective first-generation alphas. The 5830- and 5520-keV lines are assigned as depopulating the high and low spin isomers in ^{172}Ir, respectively.

The 6282-keV α is correlated with the other ^{172}Ir decay of 5520 keV, as shown in Fig. 6.2(d). The 4.4 s state in ^{172}Ir, from which the 5520-keV originates, decays predominantly by β emission (98%) [13]. The half-lives of the three lowest energy alphas are approximately 1.36(2) s, indicating that they originate from the same state in ^{176}Au. A different half-life of 1.05(1) s is found for the 6282-keV α and suggests that it originates from another state (see Table 5.1). Indeed, we are proposing an alternate interpretation of the previously observed 6220- and 6282-keV alphas, which is discussed below.

Further evidence for our ^{176}Au α-decay scheme may be substantiated by observing the γ rays emitted before the α decay (and observed in Gammasphere) through the RDT method, as shown in Fig 6.3. The analysis shows a different γ-ray spectrum preceding the 6282-keV alpha (Fig. 6.3(d)) compared with the other three spectra associated with the 6080-, 6117-, and 6220-keV alpha peaks (Fig. 6.3(a)-(c)). Note the different relative strengths of the 133-, 180-, 205-, 210-, and 296-keV γ rays in Fig. 6.3(a)-(c) compared to 6.3(d). If all the alphas decayed from the same state in ^{176}Au, the RDT γ spectra would be essentially identical. This is not the case, and thus we conclude that the 6282-keV α originates from a different state in ^{176}Au. We note also that these spectra display the Au x-rays at 69 and 78 keV, which provides further assurance that these α particles and γ rays are associated with Au.

A detailed decay scheme can be constructed by inspecting the coincidence relationship between these alphas and subsequent γ rays observed at the DSSD. We find no γ ray in coincidence with the 6282- or 6287-keV α peaks, which indicates they directly feed α-decaying states in ^{172}Ir. However, 175- and 212-keV γ rays are found to be in coincidence with α-decay lines at 6117 and 6080 keV, respectively. The γ spectra are shown in the inserts of Figs. 6.2(a)-(c), where a gate was placed on the corresponding α lines. The sum of the latter two α-decay lines and their correlated γ rays approximately equals the value of 6287 keV. The resulting level scheme is shown in Fig. 6.4; the spin and configuration assignments will be discussed below.

As stated previously, we observe inconsistencies with the previously reported α-decay line at 6220 keV [18, 82, 102]. The 6220-keV peak in Fig. 6.1(a) is believed to result from the summing of K-conversion electrons of the 212- and 175-keV transitions

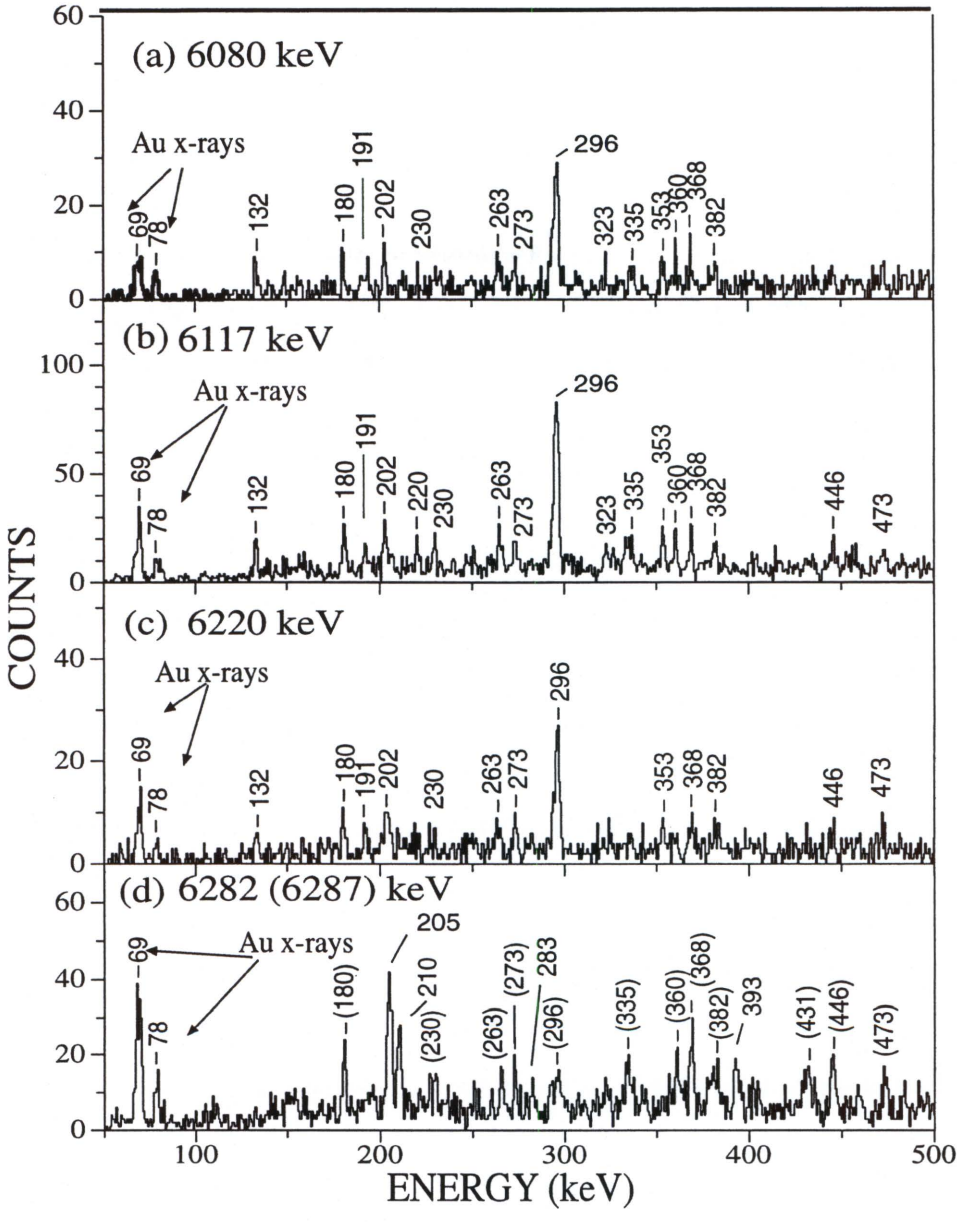

Figure 6.3: RDT spectra of γ rays associated with ^{176}Au. Prompt γ rays emitted by $A = 176$ nuclides which subsequently emitted the (a) 6080-, (b) 6117-, (c) 6220-, and (d) 6282-keV α particles. In spectrum d the lines marked with energies in parentheses are probably associated with the 6287-kev α, the others with 6282 keV.

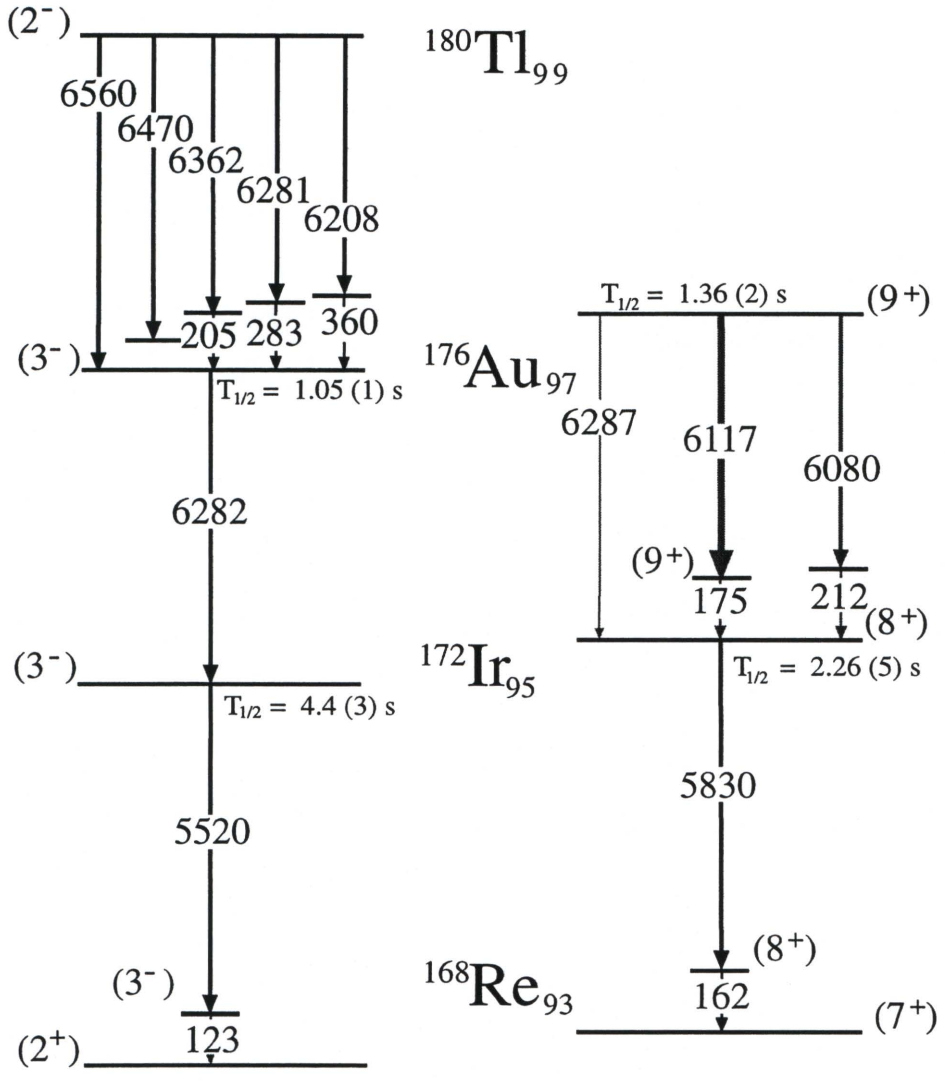

Figure 6.4: The α-decay scheme for ^{176}Au. All energies in keV; those less than 400 keV correspond to γ rays in coincidence with α transitions. The ^{180}Tl α-decay lines were reported by Toth *et al.* [105]. The 205-, 283- and 360-keV γ rays in ^{176}Au are obtained from the RDT spectrum shown in Fig. 6.3(d), since no α-γ correlations were performed in the previous work. The half-life of the (9^+) state in ^{176}Au is the weighted average of the half-lives of the 6080- and 6117-keV α transitions and the sum line at 6220 keV.

with their correlated α lines (6080+212-K, 6117+175-K; where K ($\approx$ 76.1 keV) is the K shell electron binding energy of Ir), giving rise to a "fake" α peak near 6216 keV in the α-decay spectrum. This summing effect is strong since the source is implanted at a few micrometers depth in the DSSD and typically occurs with fine-structure α-decay. The presence of the K x-rays, which are a signature of K conversion, in coincidence with the 6220-keV line seems to substantiate this scenario.

6.3.2 ^{174}Au Alpha Decay

Fig. 6.1(b) displays the α-decay lines associated with $A = 174$ recoils under the condition that the α was observed less than one second following an implantation in the same pixel. The α peak at 6040(5) keV is identified with ^{174}Pt [80] decay, and the two α decay lines at 6547(5) and 6618(15) keV were previously assigned to ^{174}Au [81, 82]. Page *et al.* [81] reported the correlation of the 6547-kev α with the daughter ^{170}Ir α-decay line at 6088(5) keV, but could not correlate the 6618-keV alpha due to the low number of events.

A matrix with correlated first and second generation α decays was made in order to determine the placement of the remaining α lines. First-generation α decays were restricted to $A = 174$ recoils and detection within one second following implantation. The second-generation α decay was defined as any decay event within five seconds of the first decay. Alpha decay lines at 6433(5), 6471(5), 6547(5), and 6618(15) keV were found to precede the 6088-keV peak, which is associated with ^{170}Ir [102] decay. The correlated spectra are shown in Fig. 6.5(a)-(d), and all four α-decay lines are positively identified with ^{174}Au. The latter two α energies are in good agreement with previously published values of 6544(10) [81] and 6626(10) [82]. The half-lives of the four α-decay lines are similar (see Table 5.1), and lead to a weighted average of $T_{1/2} = 162(3)$ ms for the state in ^{174}Au. The RDT method showed that all four alphas were correlated with similar γ-ray spectra observed at the target position indicating that all four emerge from a single level. The RDT spectra that are correlated with the four alphas are presented in Fig. 6.6(a)-(d). A detailed decay scheme was produced by inspecting the coincidence relationship between these

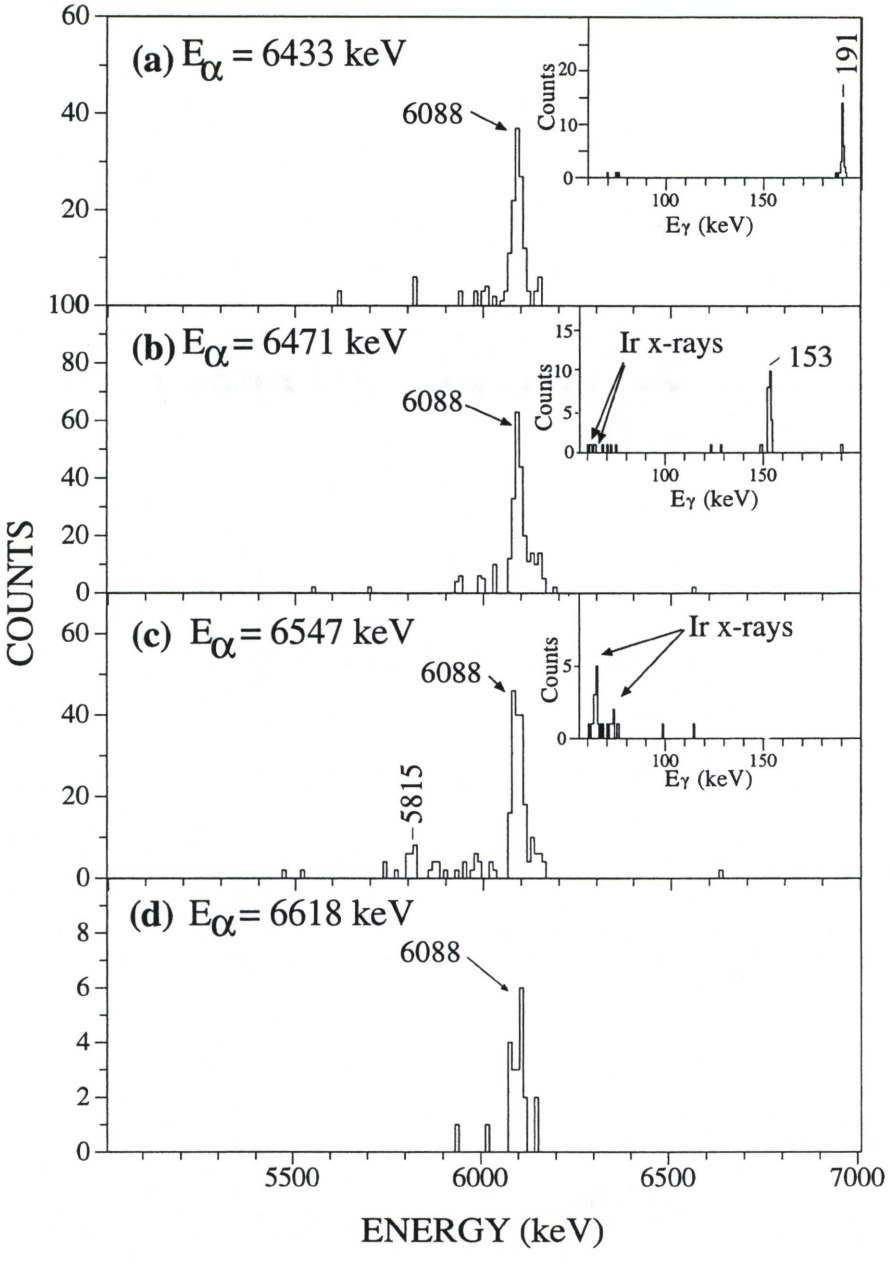

Figure 6.5: Spectra of second-generation alphas of ^{174}Au. These are emitted within five seconds after emission of four lines detected within one seconds after an implantation of $A = 174$ recoils. The inserts shows γ rays observed at the focal plane of the FMA which are in coincidence with the respective first-generation alphas. The 6088- and 5815-keV lines are assigned as depopulating the high and low spin isomers in ^{170}Ir, respectively.

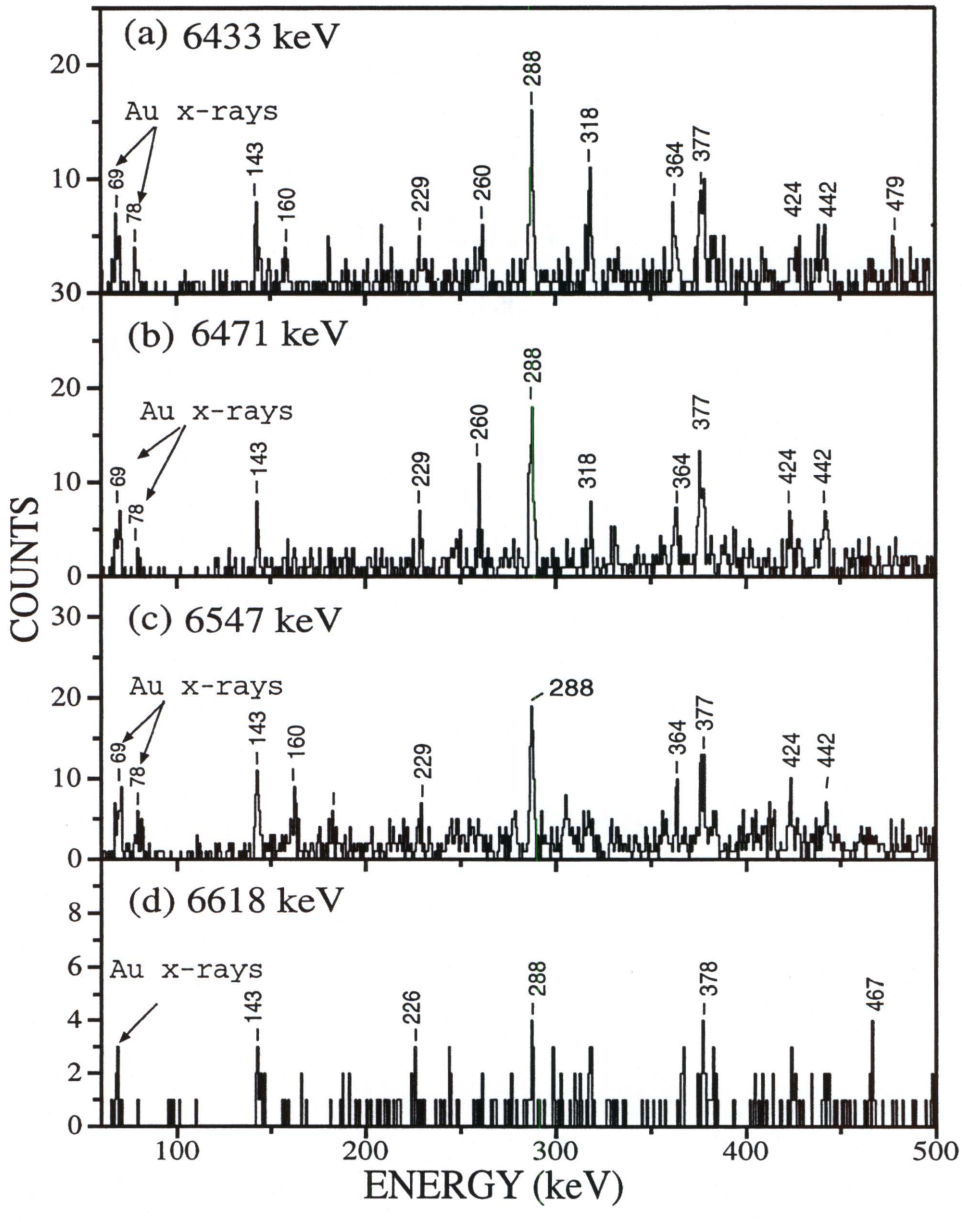

Figure 6.6: RDT spectra of γ rays associated with ^{174}Au. Prompt γ rays emitted by $A = 174$ nuclides which subsequently emitted the (a) 6433-, (b) 6471-, (c) 6547-, and (d) 6618-keV α particles.

α lines and the γ-ray transitions observed at the DSSD. No subsequent γ line was found in coincidence with the 6618-keV alpha. However, γ rays with energies of 153 and 191 keV were found in coincidence with the α lines at 6471 and 6433 keV, respectively (see inserts of Fig. 6.5(a)-(b)). No K_α x-rays were seen in the spectrum containing the 191-keV transition, implying an $E1$ multipolarity. Similar to the 6080- and 6117-keV α peaks in ^{176}Au, the summing contribution of K-conversion electrons from the 153-keV transition and its correlated alpha gives rise to a "sum" α peak at approximately 6548 keV(6471+153-K). This is substantiated by the coincidence of the 6547-keV α with only Ir x-rays. However, in Fig. 6.5(c), one may note a weak α line at 5815 keV, indicating that a component of the 6547-keV peak feeds a different state in ^{170}Ir. Indeed this decay chain was previously observed by Rowe *et al.* [89] to follow the decay of ^{178}Tl. The larger coincidence rate of the 6547-keV alpha with K x-rays compared to that of the 153-keV γ with the 6471-keV α implies a large conversion coefficient for the 153-keV transition. This implies a possible $M1$ character for the 153-keV transition. The sum of the γ rays and their correlated α energies approximately equals 6618 keV, thus suggesting that the two lowest energy alphas feed excited states above one of the α-decaying states in ^{170}Ir. The deduced decay scheme is presented in Fig. 6.7.

6.3.3 New Excited States in ^{176,174}Au

Information on the γ rays preceding α emission has led to the tentative level schemes for ^{176,174}Au shown. The placement of the levels in these nuclei are based on the intensities of the γ-rays shown in Figs. 6.3 and 6.6, and the $\gamma - \gamma$ coincidences that were mass gated at $A = 176$ and $A = 174$.

Toth *et al.* [105] observed five alphas decaying from a (2^-) state in ^{180}Tl. Assuming the 6560-keV α populates the 3^- state in ^{176}Au, the Q-value differences between this α and the 6362-, 6281- and 6208-keV lines would be $\approx$ 205, 283, and 360 keV (see Fig. 6.4). In Fig. 6.3(d), the 205-, 283-, and 360-keV γ rays are observed as well as a line at 210 keV; hence, excited states were placed at E_γ = 205, 283, and 360 keV above the 3^- state. Furthermore, based on $\gamma - \gamma$ coincidences of the

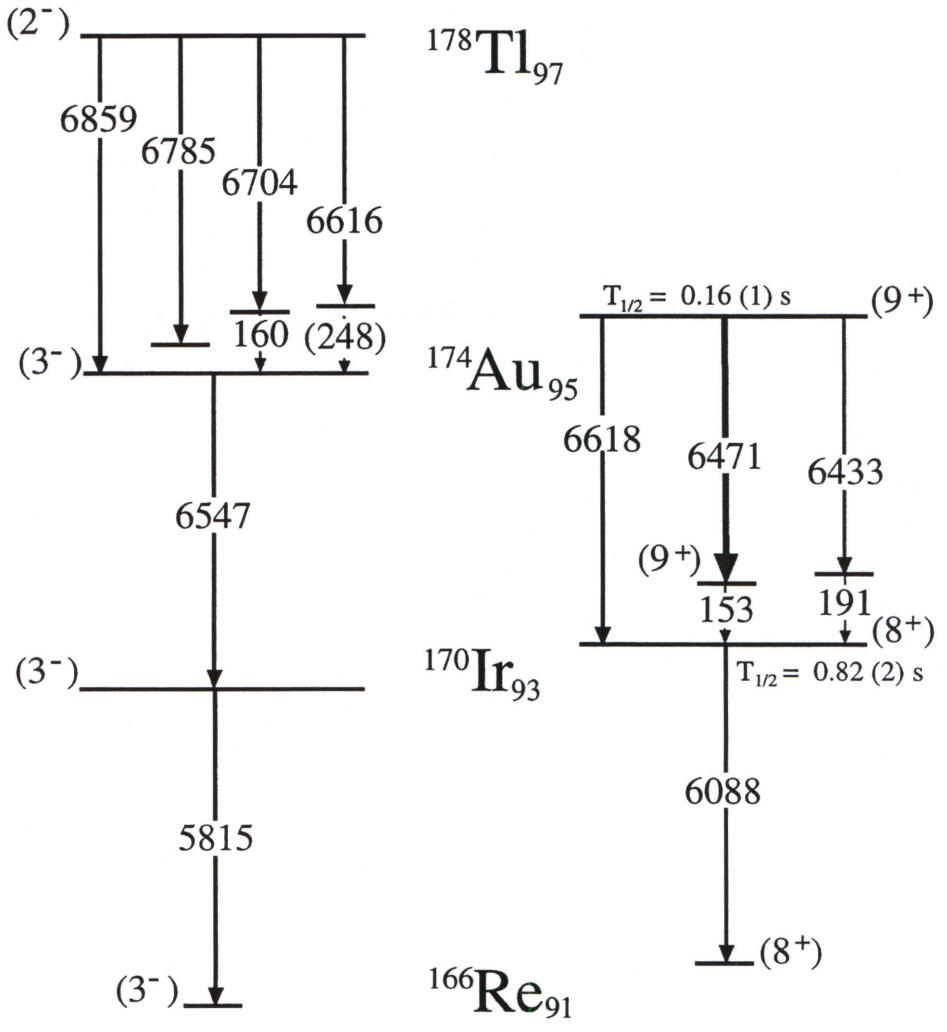

Figure 6.7: The α-decay scheme for ^{174}Au. All energies in keV; energies less than 300 keV are those of γ rays in coincidence with α particles. The ^{178}Tl α-decay lines were reported by Rowe *et al.* [89]. The 160-keV transition above the (3^-) state in ^{174}Au is obtained directly from Fig. 6.6(c) since no α-γ correlations were performed in previous work. The half-life of the (9^+) state in ^{174}Au is the weighted average of the half-lives of the 6433-, 6471-, and 6618-keV transitions. It is not clear if the (3^-) and (8^+) levels in ^{166}Re are excited or ground and isomeric states.

$A = 176$ recoils, it was found that the 210-keV transition is not in coincidence with the 205-, 283-, and 360-keV transitions. Therefore, we place another level at 210 keV above the 3^- state. The 296-keV transition apparently feeds the 9^+ state in ^{176}Au (see Fig. 6.3(a)-(b)) because of its intensity. From the RDT and $A = 176$ $\gamma-\gamma$ coincidences, we observe two distinct structures built upon the 9^+ state, one associated with the 133-, 296-, 323-, 336-, 353-, 369- and 381-keV transitions (Fig. 6.8(b)) and the other with the 180-, 202-, 229-, 273-, 368-, 473-, and 511-keV transitions (Fig. 6.8(c)). Because of the complexity of the second structure, we tentatively assign the 273-keV transition as feeding the 9^+ state (see also Fig. 6.9(top) and Tables 6.1).

Rowe *et al.* [89] observed ^{178}Tl alpha decays with energies of 6616, 6704, 6785, and 6859 keV. If the 6859-keV α is assumed to feed the 3^- state in ^{174}Au, the differences in Q-values between this α and the 6704- and 6616-keV lines are $\approx$ 160 and 248 keV. We observe a strong 160-keV γ ray in Fig. 6.6(c) and place an excited state 160 keV above the 3^- state in ^{174}Au. We did not see any evidence for a $\sim$248-keV γ ray in our RDT spectra or $A = 174$ $\gamma - \gamma$ matrix, but nevertheless we place a tentative state at 248 keV above the 3^- state. Similar to the 296-keV transition in ^{176}Au, the 288-keV transition is placed above the 9^+ state in ^{174}Au because it is the most intense γ ray observed in Fig. 6.6(a)-(b). Another transition is placed 377 keV above this state because the 377-keV γ ray was found to be not in coincidence with the 288-keV transition. At this moment we could not place the 363-, 143-, 441- and 261-keV transitions in the level scheme because they feed both the 288- and 377-keV γ rays(see Fig.6.10 and Table 6.2). We would like to note that all the levels in ^{176,174}Au must be considered as tentative since these levels were based on limited γ-ray data .

6.3.4 New Excited States in ^{172}Ir

Excited states have been observed for the first time in the neutron-deficient ^{172}Ir. The excited states in ^{172}Ir were populated via the ^{92}Mo(^{84}Sr,3pn) reaction at 390 and 395 MeV. A γ-γ matrix associated with $A = 172$ recoils was created. RDT was performed to find transitions in ^{172}Ir by gating on the 5830-keV α, as displayed in Fig. 6.11(a). A tentative level scheme of ^{172}Ir was obtained (see Fig. 6.9(bottom)), using the α decay

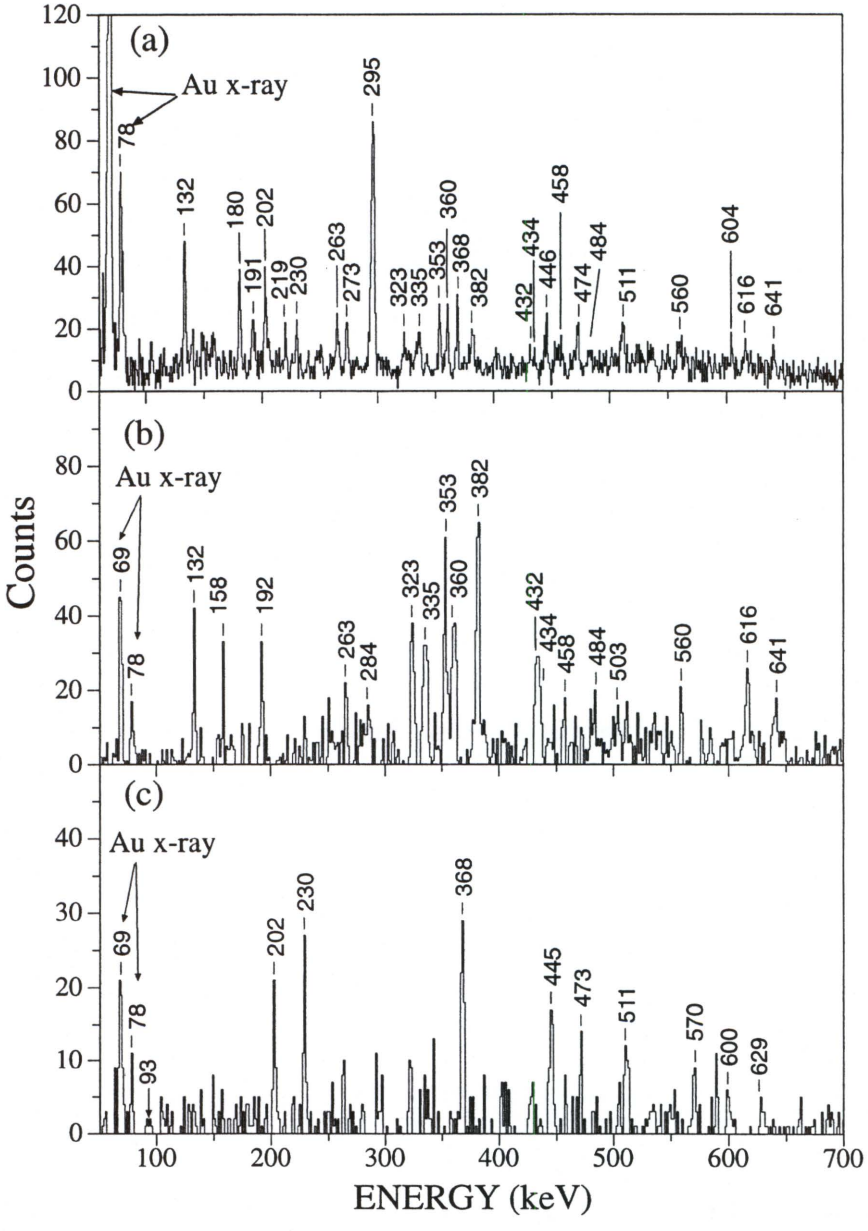

Figure 6.8: Spectra of coincident γ rays associated with the high-spin state in ^{176}Au. (a) Efficiency corrected prompt γ rays emitted by ^{176}Au which subsequently emitted the 6080- and 6117-keV α particles. The other two parts show γ rays in coincidence with the (b) 295- and (c) 180-keV γ-ray transitions. All energies are in keV.

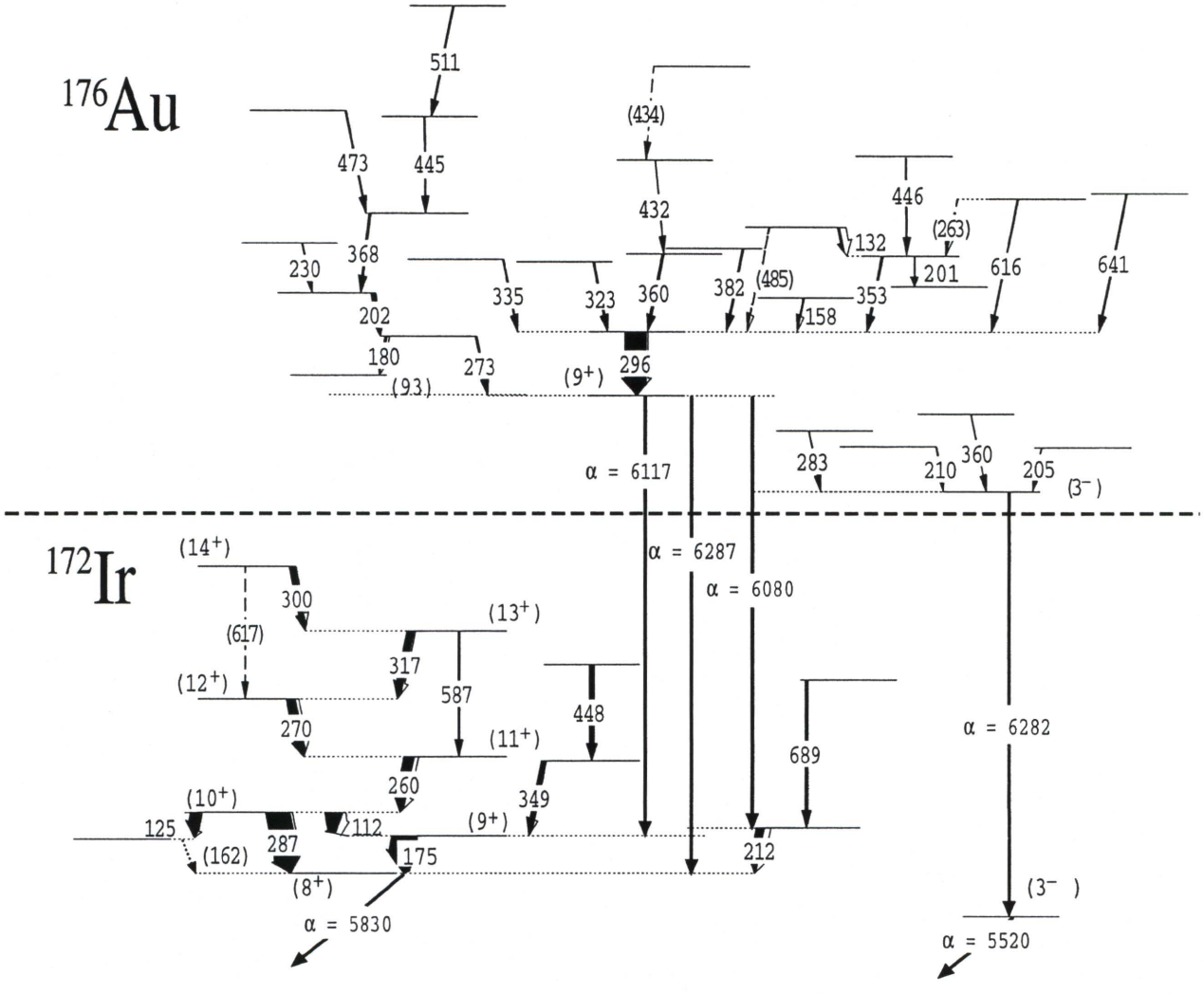

Figure 6.9: Tentative level schemes for ^{176}Au and ^{172}Ir. The width of the arrow is proportional to the relative intensity of the transition.

Table 6.1: RDT data for levels and γ rays in ^{176}Au.

E_{level} (keV)	E_γ (keV)[a]	$I_\gamma(rel.)$	Coincidence γ rays
x+295.6	295.6	450(23)	132, 158, 191, 323, 335, 353, 360
			382, 432, 434, 446, 485, 616, 641
x+618.8	323.2	50 (12)	296
x+630.9	335.3	66(11)	296
x+655.8	360.2	85(11)	296, 432, (434)
x+1037.7	381.9	62(11)	296
x+1087.4	431.6	15(6)	296, 360, (434)
x+648.2	352.6	78(11)	132, 296
x+780.0	132.2	90(6)	201, 296,353
x+911.4	263.6	72(11)	296, 353, (201)
x+911.6	616.0	49(10)	296
x+936.4	640.8	57(10)	296
x+453.9	158.3	30(10)	296
x+780.3	484.7	20(10)	296
x+272.9	180.5	88(11)	(93), 202, 230, 368, 445, 473, 511
x+272.9	272.9	63(10)	202, 230, 368, 445, 473, 511
x+475	202.1[b]	105(15)	(93), 132,180, 273, 230, 368, 445, 473, 511
x+843.1	368.1	80(11)	(93), 180, 202, 273, 445, 473, 511
x+1288.4	445.3[b]	63(11)	(93), 180, 202, 273, 368, 511
x+1799.2	510.8	57(11)	(93), 180, 202, 273, 368, 445
x+1761.5	473.1	55(12)	(93), 180, 202, 273, 368
	191	70(10)	296

*These transitions are correlated with subsequently emitted α-decay lines at 6080, 6117, and 6220 keV.

[a]Uncertainties in E_γ are 0.2 keV for most transitions except for relatively weak transition which are 0.5 keV.

[b]These transitions are doublet.

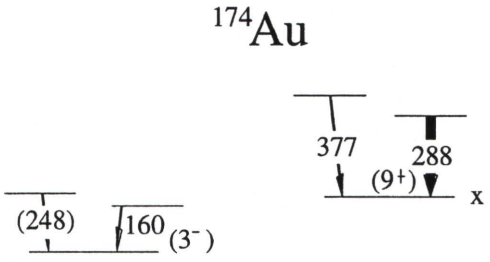

Figure 6.10: Tentative level scheme for ^{174}Au. All energies are in keV. The width of the arrow is proportional to the relative intensity of the transition.

Table 6.2: RDT data for levels and γ rays in ^{174}Au.

E_{level} (keV)	E_γ (keV)[a]	$I_\gamma(rel.)$	Coincidence γ rays
x+287.6	287.6	89(9)	143, 261, 363, (441)
x+377.4	377.4	73(9)	143, 261, 363
	143.1	60(21)	288, 363, 377
	260.7	30(6)	288, 318, 377, 441
	363.3	40(6)	143, 288, 377
	229.1	30(6)	288, (377), 441
	441.2[b]	40(6)	229, 261, (288)
	317.7	14(5)	261

*These transitions are correlated with subsequently emitted α-decay lines at 6433 and 6471 keV.

[a]Uncertainties in E_γ are 0.2 keV for most transitions except for relatively weak transition which are 0.5 keV.

[b]These transitions are doublet.

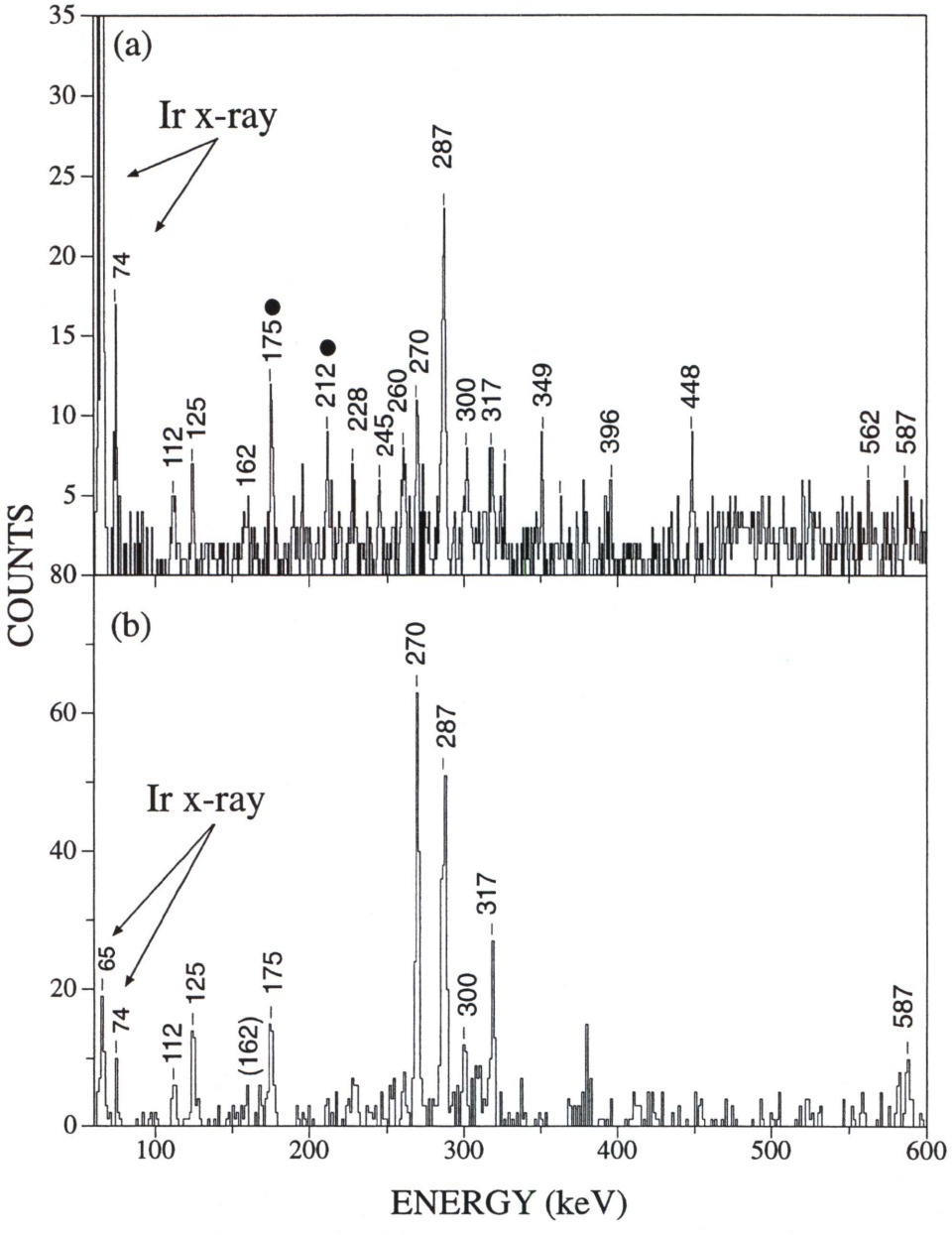

Figure 6.11: Spectra of coincident γ rays associated with the high-spin state in ^{172}Ir. (a) Efficiency corrected prompt γ rays emitted by nuclei which subsequently emitted a 5830-keV ^{172}Ir α. The 175- and 212-keV γ rays (denoted by filled dots) were observed in coincidence with the 6117- and 6080-keV alphas from ^{176}Au, respectively. (b) Prompt γ rays in coincidence with the 260-keV γ-ray transition. All energies are in keV.

scheme of ^{176}Au and the prompt γ-ray spectrum generated by the RDT method. The placements of the γ transitions are based on the coincidence relations (see Fig. 6.11) and the measured intensities of the γ rays (see Table 6.3). From the γ-γ coincidence relation, the 175-keV transition is not correlated with the 212-keV γ ray, which is consistent with the observed α-decay properties of ^{176}Au. We believe that all the γ rays that are in coincidence with the 287- and 175-keV γ rays are associated with a rotational band built on the (8^+) state. Furthermore, we suspect the (9^+) state, which is 212 keV above the (8^+) state, is the bandhead of another rotational band and has the same configuration as the (9^+) state in ^{176}Au, since there is a strong α transition linking the two states. The γ rays at 448 and 689 keV are likely part of this rotational band. The (8^+) state and (9^+) state in ^{172}Ir are discussed below.

6.4 Discussion

6.4.1 ^{176}Au Alpha-Decay Chain

The α and β decays of two states in ^{172}Ir with half-lives of 4.4 s and 2.26 (5) s were first reported by Schmidt-Ott *et al.* [13]. The 2.26 s isomer was assigned a spin of (7^+) because it was observed to have a strong feeding to the 6^+ and 8^+ states of the yrast band in ^{172}Os via β decay. Schmidt-Ott *et al.* suggested that the strong β feeding to these states is mediated by higher-lying excited states with $K > 0$ because direct feeding of the $K = 0$ band is highly forbidden. They assigned even parity and suggested a configuration of $\pi h_{11/2}$ [505]11/2 $\otimes$ $\nu h_{9/2}$ [521]3/2 for the 2.26 s state. However this neutron assignment seems unlikely because the $\nu h_{9/2}$ [521]3/2 band is not seen in the neighboring nuclei, ^{171}Os [85] and ^{173}Pt [59]. The 2.26 s isomer emits a 5830-keV α to an excited state that decays via a 162-keV γ ray to an isomer in ^{168}Re (see Fig. 6.12(b)). This isomer was assigned a spin of (6^+); however it should be noted that the (6^+) state in ^{168}Re is tentative because direct β feeding to the ^{168}W nucleus was not observed [104].

Davidson *et al.* [103] observed spin states as high as $I = 10$ in ^{176}Pt resulting from the β decay of ^{176}Au. Furthermore, the $I = 8$ state was observed to be the most

Table 6.3: RDT data for levels and γ rays in ^{172}Ir.

E_{level} (keV)	I_i^π	E_γ (keV)[a]	$I_\gamma(rel.)$
x+287.1	(10^+)	287.1	50(9)
x+175.0	(9^+)	175.0	22(6)
x+287.1	(10^+)	112.1	13(4)
x+547.6	(11^+)	260.5	20(6)
x+817.2	(12^+)	269.6	19(6)
x+1134.6	(13^+)	317.4	14(5)
x+1134.6	(13^+)	587.0	9(3)
x+1435.0	(14^+)	300.4	11(4)
x+212.0	(9^+)	212.0	17(5)
x+560.2	(10^+)	348.6	9(2)
x+1006.6	(12^+)	447.6	6(2)
x+287.1		124.8	13(4)
		162.3	<5
		689.2	<5

*These transitions are correlated with subsequently emitted α-decay lines at 5830 keV.

[a]Uncertainties in E_γ are 0.2 keV for most transitions except for relatively weak transition which are 0.5 keV.

[b]These transitions are doublet.

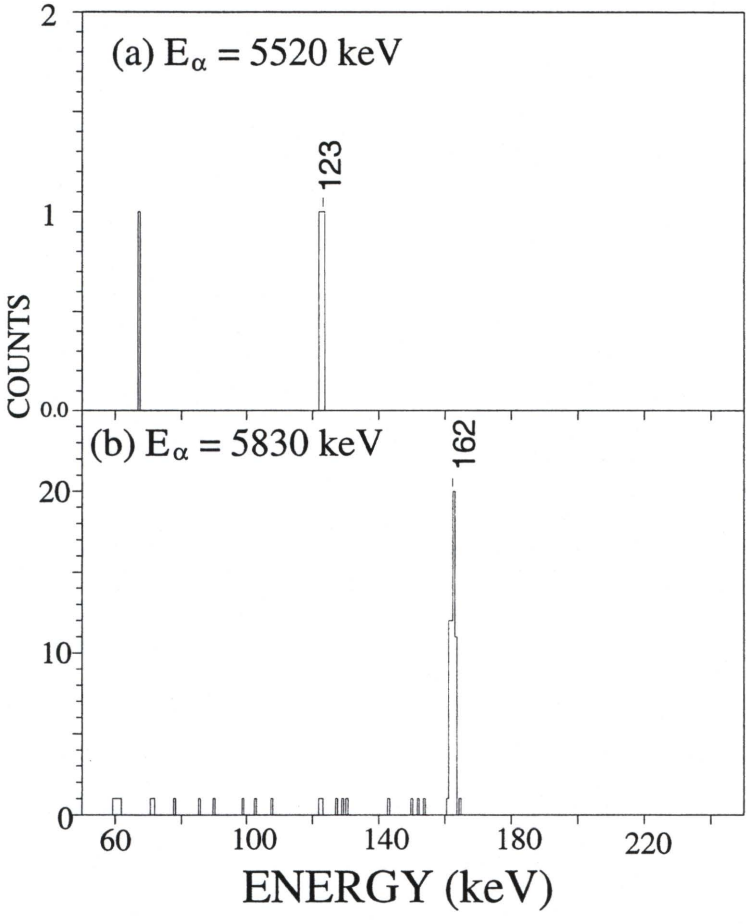

Figure 6.12: Spectra of γ rays emitted at the focal plane of the FMA which are mass-gated at $A = 172$. They are also in coincidence with the (a) 5520- and (b) 5830-keV α particles in ^{172}Ir.

strongly populated from a high-spin parent state in ^{176}Au. This would indicate that the 1.36 s state in ^{176}Au has a spin of 9, in order to satisfy the β selection rule of $\Delta I = 1$. Hence, the 2.26 s state in ^{172}Ir is reassigned a spin of 8, because the most intense α line from the 1.36 s state in ^{176}Au populates an excited state (which presumably would also have $I = 9$) in ^{172}Ir that γ decays ($E_\gamma = 175$ keV) to the bandhead (see Fig. 6.4). A similar argument can be made to suggest that the high-spin isomer in ^{168}Re has $I^\pi = 7^+$ as the α decay from the ^{172}Ir primarily feeds an excited state. Therefore, we suggest new spin assignments of (9^+), (8^+), and (7^+) for the high-spin isomers in ^{176}Au, ^{172}Ir, and ^{168}Re, respectively.

The 1.05 (1) s isomer in ^{176}Au decays by emission of a 6282-keV α and is assigned a spin of 3 because this α directly feeds the 4.4 s state in the daughter ^{172}Ir [13], which was assigned a spin of 3 as it was observed to beta decay directly to the 2^+ and 4^+ states of the yrast band in ^{172}Os [13]. This is also consistent with the fact that the $I = 2$ state in ^{176}Pt was strongly populated by the β decay from ^{176}Au [103]. Furthermore, Toth *et al.* [105] observed the correlation of four α lines decaying from the ^{180}Tl (2^-) state with the 6282-keV α. It was observed that the most intense α line feeds an excited state. All of this leads to a likely spin of 3 for the 1.05 s state. We observe that the $I = 3$ state in ^{172}Ir α decays at $E_\alpha = 5520$ keV to an excited state at 123 keV in ^{168}Re (see Fig. 6.12(a)). However, we did not observe the coincidence of the 89- and 136-keV γ rays with the 5520-keV α-decay line as previously reported [13]. Also, we did not observe any conversion-electron associated x-rays for the 123-keV γ line, implying an $E1$ transition, such that spins of (3^-), (3^-), and (2^+) are proposed for the low-spin states in ^{176}Au, ^{172}Ir, and ^{168}Re, respectively.

6.4.2 Configuration Assignments

For $N \approx 97$ nuclei, Nilsson orbitals originating from the $f_{7/2}$, $h_{9/2}$, and $i_{13/2}$ subshells are located close to the neutron Fermi suface at a quadrupole deformation of $\beta_2 \approx 0.15$. This deformation was determined by the total Routhian surface calculations (TRS) [28, 29] which predict $\beta_2 = 0.13$, $\beta_4 = -0.01$, $\gamma = -85.2°$ for ^{176}Au (Fig. 6.13(a)),

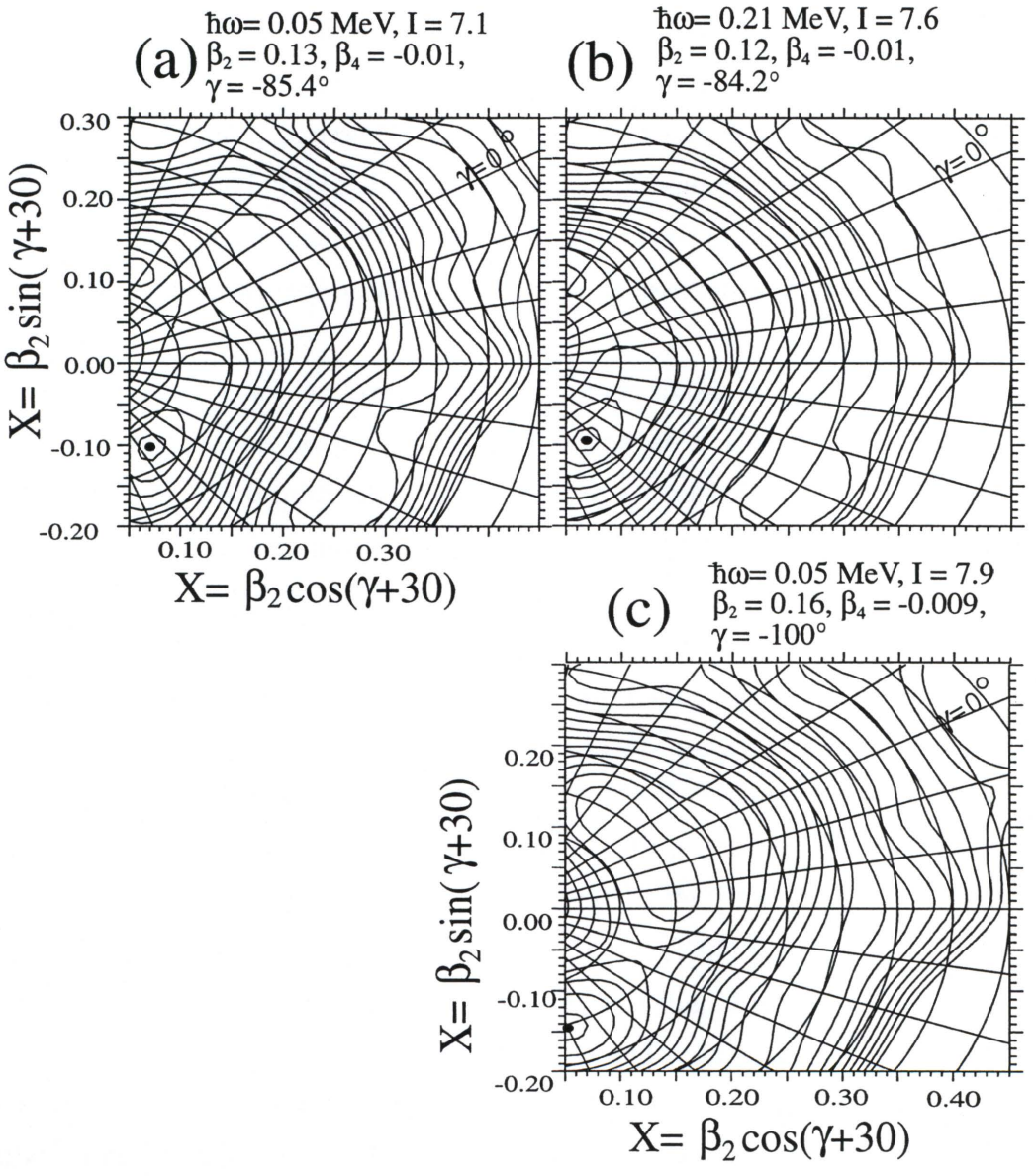

Figure 6.13: Total Routhian Surfaces for ^{174,176}Au and ^{172}Ir. The $\pi h_{11/2} \otimes \nu f_{7/2}$ configuration for (a) ^{176}Au, (b) ^{174}Au, and (c) ^{172}Ir .

$\beta_2 = 0.12$, $\beta_4 = -0.01$, $\gamma = -84.2°$ for ^{174}Au (Fig. 6.13(b)), and $\beta_2 = 0.16$, $\beta_4 = -0.01$, $\gamma = -100.0°$ for ^{172}Ir (Fig. 6.13(c)) at $\hbar\omega = 0.05$ MeV. All these values correspond to the lowest minima.

In these diagrams (Fig. 6.13), one can also see the complexity of these nuclei as multi-minimum surfaces are observed. It is also apparent that these gold and iridium nuclei are soft with respect to γ deformation. Therefore, one should be cautious with the large negative γ values quoted above since these numbers correspond to the lowest calculated minima. The complexity of the TRS diagrams is also illustrated in Fig. 6.9 where various structures, rotational-like, vibrational-like, and single-particle can be seen.

It is difficult to assign configurations for ground (or isomeric) states that have near-spherical or γ-soft structures. K is not a good quantum number when γ is large, which allows for strong mixing between the orbitals. Fig. 6.14 (bottom) displays the Woods-Saxon proton single-particle diagram and at $Z = 79$ and at $\beta_2 \approx 0.13$ the $d_{3/2}$ [402]3/2, $h_{11/2}$ [505]11/2, $s_{1/2}$ [400]1/2, and possibly $d_{3/2}$ [411]1/2 orbitals are located near the Fermi surface.

By inspecting the odd-A Au and Ir nuclei in the mass 170 region, one observes that two alpha-decaying states exist, associated with high-spin $I = 11/2^-$ [11, 13] ($9/2^-$ in Re [13] and ^{175,177,179}Ir [107, 95]) and low-spin $1/2^+$ [11, 98] ($3/2^+$ in ^{179}Au [97]) states. Therefore, the likely proton orbitals involved are the $h_{11/2}$ [505]11/2 ($h_{11/2}$ [514]9/2 in Re and ^{175,177,179}Ir) and $d_{3/2}$ [411]1/2 (or the $s_{1/2}$ [400]1/2). Poli *et al.* [106] proposed $s_{1/2}$ [400]1/2 as the configuration for the $1/2^+$ α-decaying state in ^{173}Au, while in ^{177}Au Kondev *et al.* [11] tentatively assigned $I^\pi = (1/2, 3/2)$ to the low-spin α-decaying state. The authors [11] proposed an oblate $d_{3/2}$ [411]1/2 or the prolate $d_{3/2}$ [402]3/2 configuration to describe the $I^\pi = (1/2,3/2)$ state based on limited decay work on ^{173}Ir [13] and parent ^{181}Tl [99]. The proposed configurations for the odd-A Au, Ir, and Re nuclei can be found in Table 5.2.

Similarly, the Woods-Saxon single-neutron diagram is shown in Fig. 6.14 (top). Two different negative-parity orbitals, $f_{7/2}$ [503]7/2 and $h_{9/2}$ [514]7/2, are found near the Fermi surface for $N = 97$. It is observed that the neighboring odd-A ^{177,179}Hg, $^{173-177}$Pt, and $^{169-173}$Os nuclei exhibit either a $5/2^-$ [12, 18, 59] or $7/2^-$ [9]

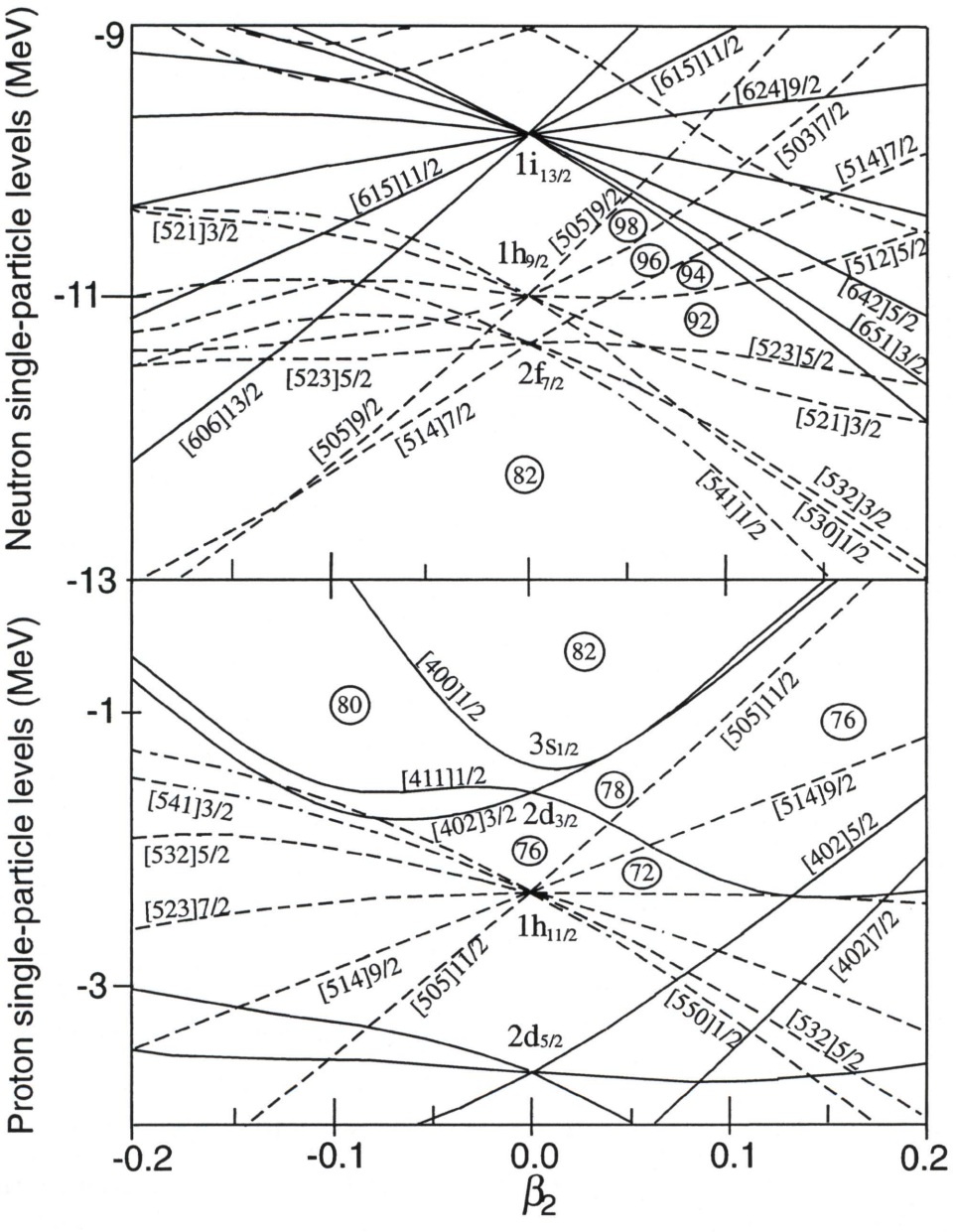

Figure 6.14: Woods-Saxon single-particle diagrams for neutrons (top) and protons (bottom).

Table 6.4: Configurations for the ^{176}Au α-decay chain.

Nucleus	I^{π}	$T_{1/2}$ (sec)	π orbital	ν orbital	$\uparrow\uparrow$ coupling[a]	$\uparrow\downarrow$ coupling
$^{176}_{79}Au_{97}$	3^-	1.05	[411]1/2	[503]7/2	3^-	4^-
	9^+	1.36	[505]11/2	[503[7/2	9^+	2^+
$^{172}_{77}Ir_{95}$	3^-	4.40	[411]1/2	[523]5/2	3^-	2^-
			([400]1/2)	([512]5/2)	(3^-)	(2^-)
	8^+	2.26	[505]11/2	[512]5/2	8^+	3^+
$^{168}_{75}Re_{93}$	3^-		[411]1/2	[523]5/2	3^-	2^-
	2^+		[514]9/2	[523]5/2	2^+	7^+

[a] For an odd-odd deformed nucleus, the parallel coupling of the intrinsic spins give the lowest-energy configuration according to the Gallagher-Moszkowski rule [109].

ground state. The isotone of ^{176}Au, ^{175}Pt [9], has a $7/2^-$ ground state which can be attributed to either the $f_{7/2}$ [503]7/2 or the $h_{9/2}$ [514]7/2 orbitals. These orbitals are strongly mixed in this region. The only way to obtain a 9^+ state in ^{176}Au is to couple a $7/2^-$ neutron orbital with the $h_{11/2}$ [505]11/2 proton orbital. The $\pi h_{11/2} \otimes \nu f_{7/2}$ configuration best describes a 9^+ state, and $\pi d_{3/2} \otimes \nu f_{7/2}$ for a 3^- state. Assuming that the Gallagher-Moszkowski (G-M) [109] rule is applicable, then the specific Nilsson configurations for the ^{176}Au α-decay chain are listed in Table 6.4.

The (3^-) and (8^+) states in ^{172}Ir can be explained by the coupling of the neutron $5/2^-$ orbital with the proton $1/2^+$ and $h_{11/2}$ [505]11/2 orbitals, respectively. Assigning the neutron $5/2^-$ orbital to ^{172}Ir is reasonable because the ground state of ^{171}Os is assigned a $\nu h_{9/2}$ [523]5/2 [108] configuration, while in ^{173}Pt [59] the ground state is likely the mixture of $\nu h_{9/2}$ [523]5/2 and $\nu f_{7/2}$ [512]5/2. Again, if the G-M rule is valid, the $\pi h_{11/2}$ [505]11/2 $\otimes$ $\nu f_{7/2}$ [512]5/2 and $\pi d_{3/2}$ [411]1/2 $\otimes$ $\nu h_{9/2}$ [523]5/2 (or $\pi s_{1/2}$ [400]1/2 $\otimes$ $\nu f_{7/2}$ [512]5/2)) define the (8^+) and (3^-) states in ^{172}Ir, respectively, while the (7^+) and (2^+) states in ^{168}Re both result from $\pi h_{11/2}$ [514]9/2 $\otimes$ $\nu f_{7/2}$ [523]5/2 with opposite K couplings. A $\nu h_{9/2}$ [523]5/2 orbital is chosen for ^{168}Re because both the isotones ^{169}Os [12] and ^{167}W [12] exhibit a $\nu h_{9/2}$ [523]5/2

ground state.

To further support our configuration assignment for the (8^+) state, a plot (Fig. 6.15) of γ-ray transitions of specific configurations for various Ir and Os isotopes is made. In that figure, one can see a smooth trend of all transitions versus neutron number where the energy of the transition increases inversely with deformation. The smooth varying behavior of the 2^+ to 0^+ transition in even-even Os agrees with the TRS calculations which predict lower deformation as the isotope gets lighter. This trend is also observed in odd-A Os ($\nu i_{13/2}$) and odd-A Ir ($\pi h_{9/2}$).

Since the behavior of the $\pi h_{11/2} \otimes \nu f_{7/2}$ band is well-studied in ^{176,178}Ir [110, 111], the transitions from the 13^+ to 11^+ state of that structure is plotted together with a similar transition in ^{172}Ir. One can clearly see that the 587-keV transition from the 13^+ to 11^+ state fits the systematics, indicating that our assignment for the (8^+) states in ^{172}Ir is reasonable.

6.4.3 ^{174}Au Alpha-Decay Chain

Two states were observed to α decay in ^{174}Au. Our data for ^{174}Au show the correlation between the 6433-, 6471-, and 6618-keV alpha lines originating from the 0.16 s state in ^{174}Au with the 6088-keV α decaying from the 0.8 s state in ^{170}Ir. The spin assignments for ^{174}Au and ^{170}Ir are not known since there are no beta-decay experiments on these nuclei. We tentatively assign (8^+) to this ^{170}Ir state and (9^+) to the 0.16 s state in ^{174}Au. These high-spin isomers are believed to have similar properties to the 9^+ and 8^+ states in ^{176}Au and ^{172}Ir. For ^{174}Au, the same arguments used to assign the configurations for ^{176}Au could be applied. ^{170}Ir has two known α-decaying states like ^{172}Ir. We propose using the configurations of the ^{176}Au decay chain for ^{174}Au, because ^{174}Au exhibits a similar α decay pattern to that seen in ^{176}Au. However, we are not certain if the 8^+ and 3^- states in ^{168}Re are excited or instead ground and isomeric states.

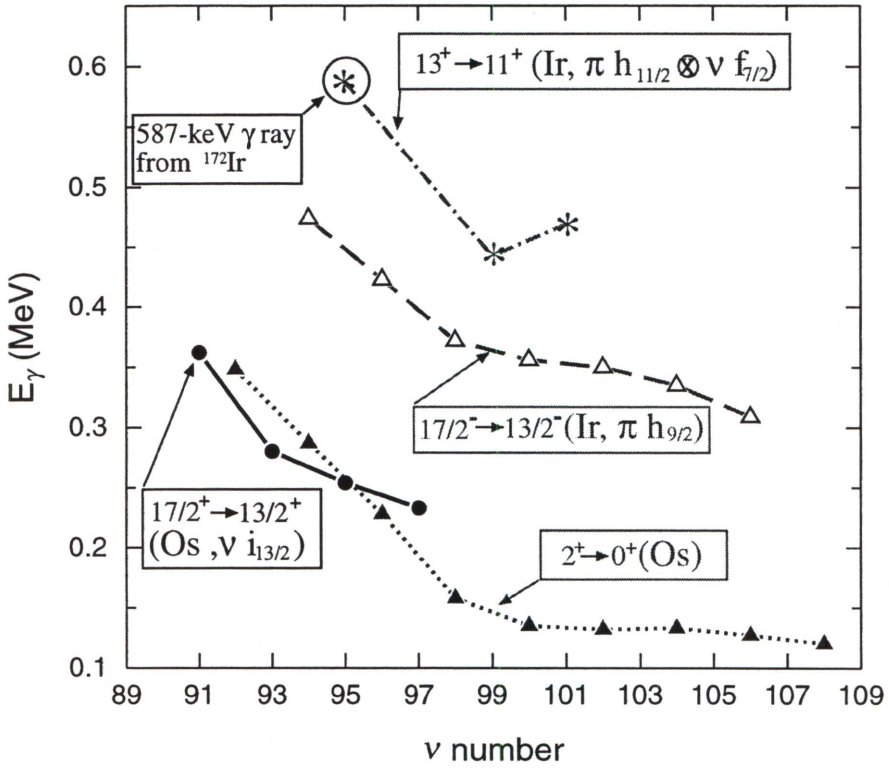

Figure 6.15: Plot of the γ-ray transitions in Ir and Os, associated with respective configurations. Data points are obtained from Refs. [18, 110, 111, 112].

CHAPTER 7

Summary and Conclusions

Great progress has been made towards the understanding of the nuclear properties of the neutron-deficient nuclei near the $Z = 82$ shell gap. Three different reactions used in the experiment produced more than 20 nuclei to study. This has made possible the study of α-decay systematics. This dissertation work greatly benefits by the use of the Recoil Decay Tagging (RDT) technique and the Fragment Mass Analyzer (FMA), which enable the separation and identification of various nuclei with similar energies and half-lives. Table 7.1 illustrates this point. Consider the similar energies of new α lines in ^{174,176}Au and previously known lines of ^{175,177}Au. The α decays of these gold nuclei were studied previously by many investigators [81, 82, 89, 102, 18]. None of these authors were able to separate the new α lines in ^{174,176}Au from the close-lying lines in ^{175,177}Au because their experiments did not utilize recoil mass separators. Without mass separation and application of the RDT method, it is unlikely that one could resolve the α lines associated with these odd-odd gold nuclei from their immediate gold neighbors.

Before the introduction of the RDT method, α-decay investigation and in-beam γ-ray study of a specific nucleus were done separately. In many instances, there was no linking of structures observed using γ-ray spectroscopy with those from α decay studies. This is due to the fact α-decay processes tend to populate low-lying states while states populated in a high-spin studies cluster around the yrast line. With the use of the RDT method, γ-ray transitions populating the ground state of a specific nucleus are correlated with the emitted α particles. The level scheme in ^{172}Ir was obtained by combining information from in-beam γ-ray structures and the α decay of parent ^{176}Au.

Table 7.1: Sample of nuclei with similar α energies.

Nuclei	I^{π}	Energy (keV)
^{174}Au	(9^-)	6433(5)
^{175}Au	$11/2^-$	6431(5)
^{178}Hg	0^+	6429(5)
^{176}Au	(9^-)	6117(5)
^{177}Au	$11/2^-$	6121(5)
^{180}Hg	0^+	6120(5)
^{174}Pt	(0^+)	6040
^{175}Pt	$7/2^-$	6037(5)
^{172}Ir	(8^-)	5830(5)
^{175}Pt	$7/2^-$	5830(5)

The results of α decay measurements from gold and platinum isotopes along with their daughter nuclei have been presented and summarized along with the literature values in Table 5.1. Two isomeric states in ^{176}Au with half-lives of 1.36 (2) and 1.05 (1) s were found. Similarly two isomeric states were observed in ^{174}Au, but only one half-life was measured ($T_{1/2}$ = 0.16(1) s). Our data exhibit several fine structure α peaks seen in the decay of ^{174,176}Au and ^{173}Pt for the first time. The use of the FMA allowed us to mass-select these alphas and clearly associate them with ^{176}Au and ^{174}Au. This was important since their energies and half-lives are similar to the ^{177}Au and ^{175}Au decays. Supporting evidence was provided by the RDT method and the correlation with alpha decay of their daughter nuclei. In addition to the new Au α peaks, in-beam structures of ^{174,176}Au and ^{172}Ir were also observed for the first time. This was made possible by the RDT method (see Fig. 7.1).

It is difficult to assign configurations for states in odd-odd nuclei. This is due to a more complex structure when compared to even-even and odd-A nuclei. Neutron and proton quasiparticles near the Fermi surface can occupy many different single-particle levels. Furthermore, the influence of a proton-neutron interaction on

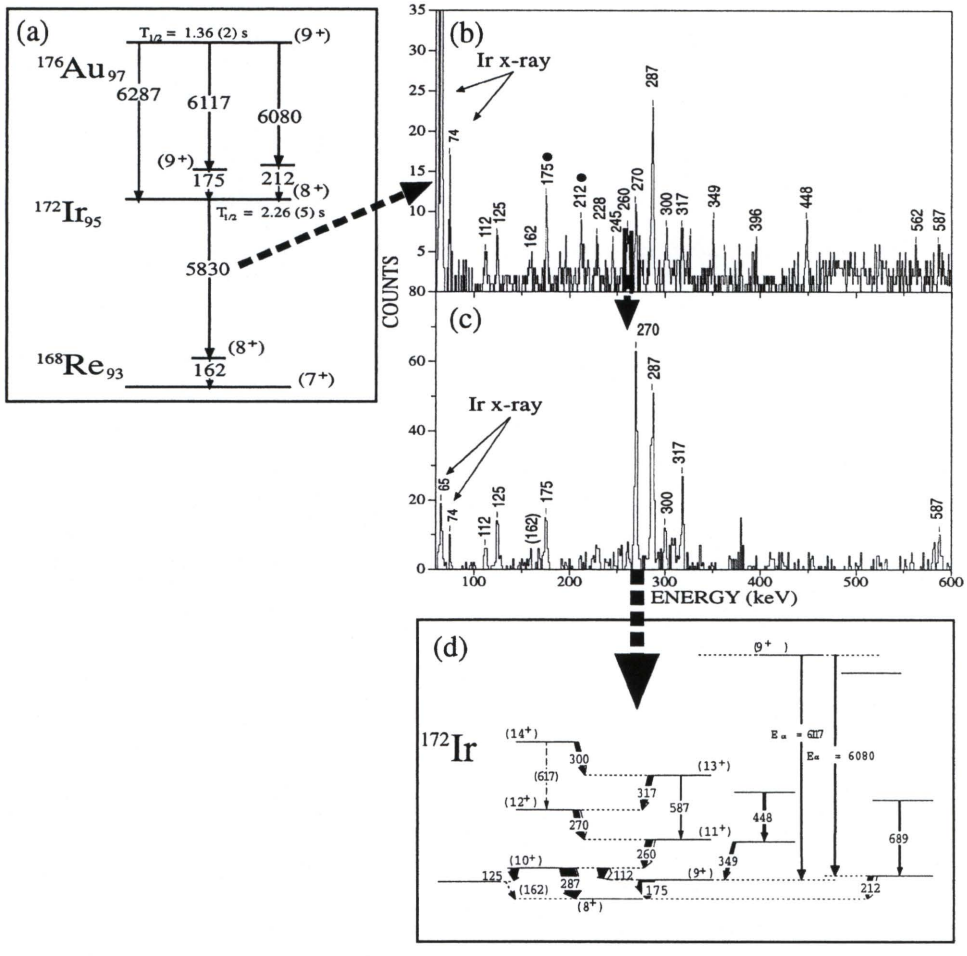

Figure 7.1: Diagram illustrating the power of combining α-decay and γ-ray spectroscopies. Part (a) displays the α-decay chain of ^{176}Au obtained from α-decay work. A gate placed on the 5830-keV α-decay line results in the RDT spectrum of ^{172}Ir (part (b)). With this spectrum, a $A = 172$ $\gamma - \gamma$ matrix was created. Part (c) displays the all γ rays which are in coincidence with the 260-keV γ ray. Finally, a tentative level scheme of ^{172}Ir shown in part (d) was created from the coincidence relations obtained from the $\gamma - \gamma$ matrix. The arrows indicate various steps of the process.

the nuclear structure of the odd-odd nucleus is not fully understood. To further complicate matters, these light odd-odd Au and Ir nuclei are predicted to have triaxial structures which would result in highly mixed K orbitals.

Nevertheless, we made configuration assignments for these odd-odd nuclei, based on the understanding of α, β, and γ decays and the single-particle structure near the Fermi surface. Our analysis and interpretation of experimental data enable the identification of the dominant proton and neutron orbitals for these nuclei, as shown in Table 6.4. It is perhaps surprising that a set of configuration assignments is found to explain the pattern of the observed alpha decays. TRS calculations indicate that ^{166,168}Re are fairly axial in deformation, and thus the assignment of Nilsson orbitals is logical for these nuclei. We show that the distinct pattern of alpha decays from Au to Ir to Re can be explained by continuing the assignment of Nilsson orbitals to Ir and Au nuclei that are surely less deformed and more triaxial than Re. Perhaps this provides some validation that the deformation parameters calculated in TRS are proper and therefore that one can make configuration assignments using the Woods-Saxon model.

The powerful combination of Gammasphere with the FMA allowed an investigation of shape co-existence and its effect at high spin in ^{174}Pt. The extension of the yrast sequence and the establishment of a side band revealed several crossings of different types. A shape change in both structures likely causes the crossings in both bands near 0.24 MeV. The side band then changes configuration from an octupole vibration to a two-quasineutron sequence at higher frequencies, and then undergoes the BC crossing near 0.29 MeV. A delayed AB alignment was observed for the ground-state band, which occurs at $\approx$ 0.28 MeV. An attempt to interpret this crossing with the Cranked Shell Model (CSM) was determined to be inadequate as the CSM is constrained to stable deformation parameters. Thus, it cannot account for any mixing of various shapes at low spin observed in ^{174}Pt. The TRS calculations enhanced the interpretation of these crossings and it was found that the AB alignment is likely delayed by the shape complexity at lower spin.

To conclude, investigation of these nuclei should not end with this dissertation. Future studies should include investigation of high-spin structures in $^{172-178}$Au

and $^{170-174}$Ir nuclei, α-decay studies using the RDT method, and also in-beam structures in the lighter even-even Pt nuclei. Information obtained from this work such, as mid-spin states and proposed bandhead configurations for the ^{174,176}Au and ^{172}Ir, can be used as a basis for future high-spin studies. A better selection of beam energy and reaction channels would definitely help.

In the case of new α-decay studies, the RDT method commonly used to investigate the physics of high-spin states should be used. In addition, I propose the re-investigation of all previously identified α-decaying nuclei such that their decay properties are consistence with in-beam information (e.g. ^{175}Ir). Finally, future experiments should include studies of in-beam structures in even-even ^{168,179,172}Pt so that the phenomena of shape-coexistence and backbending in negative-parity side bands, which is expected to occur, can be investigated and fully understood.

BIBLIOGRAPHY

BIBLIOGRAPHY

[1] R. Casten, *Nuclear Structure From a Simple Perspective*, Oxford Univ., New York (2000).

[2] R. S. Simon *et al.*, Z. Phys. A **325**, 197 (1986).

[3] E. S. Paul *et al.*, Phys. Rev. C **51**, 71 (1995).

[4] F. G. Kondev *et al.*, Phys. Rev. C **61**, 044323 (2000).

[5] M. J. A. De Voigt *et al.*, Nucl. Phys. A **507**, 472 (1990).

[6] M. Danchev *et al.*, Phys. Rev. C **67**, 14312 (2003).

[7] G. D. Dracoulis *et al.*, Phys. Rev. C **44**, R1246 (1991).

[8] B. Cederwall *et al.*, Z. Phys. A **337**, 283 (1990).

[9] F. G. Kondev *et al.*, Phys. Lett. B **528**, 268 (2002).

[10] R. Bark *et al.*, J. Phys. G **17**, 1209 (1991).

[11] F. G. Kondev *et al.*, Phys. Lett. B **512**, 268 (2001).

[12] T. Hild *et al.*, Phys. Rev. C **51**, 4 (1995).

[13] W. -D. Schmidt-Ott *el al.*, Nucl. Phys. A **545**, 646(1992).

[14] P. Möller, J. R. Nix, W. D. Myers, and W. J. Swiatecki, At. Data Nucl. Tables **59** 185 (1995).

[15] O. Zeiden, Ph.D. Dissertation at Univ. of Tennessee, 16 (2002).

[16] S. G. Nilsson, Dan. Mat.-Fys. Medd. **16**, 16 (1955).

[17] S. G. Nilsson *el al.*, Nucl. Phys. A **241**, 341 (1975).

[18] Table of Isotope 8th ed.,R.B. Firestone (Ed.) **2** (1996).

[19] S. Ćwiok. *el al.*, J. Phys. G **241**, 61 (1979).

[20] J. Bardeen *et al.*, Phys. Rev. **106** 162 (1957).

[21] A. Bohr *et al.*, Phys. Rev. **110**, 936 (1958).

[22] D. Hartley, Ph.D. Dissertation at Florida State Univ., 16 (1998).

[23] D. R. Inglis, Phys. Rev. C **61**, 126 (1954).

[24] D. R. Inglis, Phys. Rev. C **62**, 795 (1956).

[25] R. Bengtsson and S. Frauendorf, Nucl. Phys. A **327**, 139 (1979).

[26] M. J. A. Voigt, *et al.*, Rev. Mod. Phys. A **55**, 949 (1983).

[27] http://ns.ph.liv.ac.uk/ esp/nuclear/TRS/.

[28] W. Nazarewicz *et al*, Nucl. Phys. A **503**, 285 (1989).

[29] R. Wyss *et al*, Nucl. Phys. A **511**, 324 (1990).

[30] S. M. Harris, Phys. Rev. B, **138**, 509 (1965).

[31] V. F. Weisskopf, Phys. Rev. , **83**, 1073 (1951).

[32] W. D. Hamilton, *The Electromagnetic Interaction in Nuclear Spectroscopy*, North-Holland, New York, (1975).

[33] S. M. Wong, *Introductory Nuclear Physics*, John Wiley & Sons, New York, (1998).

[34] G. H. Winslow, Phys. Rev. **96**, 1023 (1954).

[35] J. O. Rasmussen, Phys. Rev. **113**, 1593 (1959).

[36] R. D. Woods and D. S. Saxon, Phys. Rev. **95**, 1617 (1954).

[37] *Heavy ion collisions* **2**, edited by R. Bock (North-Holland Pub. Co., Amsterdam; New York) (1982).

[38] R. M. Diamond and F. S. Stephens, Annu. Rev. Nucl. Part. Sci. **30**, 85 (1980).

[39] F. G. Kondev, *private communication.*

[40] I. Y. Lee, Nucl. Phys. A **520**, 641C (1990).

[41] C. N. Davids and J. D. Larson, Nucl. Instrum. and Meth. B **40/41**, 1224 (1989).

[42] C. N. Davids, *et al.*, Revista Mexicana de Fisica 39, Suppl. 2, 56 (1993).

[43] C. N. Davids *et al.*, Phys. Rev. B **70**, 358 (1992).

[44] C. J. Gross *et al.*, Nucl. Instrum. and Meth. A **450** 12 (1997). e vi

[45] D. C. Radford, Nucl. Inst. and Meth. A **361** 297 (1995).

[46] K. S. Krane *et al.*, Nucl. Data Tab. **11**, 351 (1973).

[47] A. Krämer-Flecken *et al.*, Nucl. Data Tab. **11**, 351 (1985).

[48] L. Peter Ekström and Andres Nordlund, Nucl. Inst. and Meth. A **313**, 421 (1992).

[49] A. N. Andreyev *et al.*, Nature **405**, 430 (2000).

[50] F. G. Kondev *et al.*, Phys. Lett. B **528**, 221 (2002).

[51] D. G. Jenkins *et al.*. Phys. Rev. C **66**, 011301(R) (2002).

[52] F. G. Kondev *et al.*, Phys. Lett. B **512**, 268 (2001)

[53] P. M. Davidson, *et al.*, Nucl. Phys. A **657**, 219 (1999).

[54] G. D. Dracoulis, *et al.* Nucl. Phys. A **534**, 173 (1991).

[55] R. A. Bark, J. Phys. G **17**, 1209 (1991).

[56] R. Bengtsson and W. Nazarewicz, Z. Phys. A **334**, 269 (1989).

[57] G. D. Dracoulis, Phys. Rev. C **49**, 3324 (199).

[58] M. P. Carpenter *et al.*, Phys. Rev. Lett. **78**, 3650 (1997).

[59] J. TM. Goon *et al.* to be published.

[60] W. R. Leo, *Techniques for Nucl. and Particle Phys. Expts*, Springer-Verlag, 105, (1987).

[61] G. D. Dracoulis *et al.*, Nucl. Phys. A **486**, 414 (1988).

[62] P. M. Davidson *et al.* J. Phys. G **12**, L97 (1986).

[63] P. M. Davidson *et al.* Nucl. Phys. A **568**, 90 (1994)

[64] B. Fabricius *et al.*, Phys. Rev. A **511**, 345 (1991).

[65] R. M. Lieder *et al.*, Nucl. Phys. A **645**, 465 (1999).

[66] D. G. Popescu *et al.*, Phys. Rev. C **55**, 1175 (1997).

[67] D. T. Joss *et al.* Nucl. Phys. A **689**, 631 (2001).

[68] M. P. Carpenter *et al.*, Nucl. Phys. A **513**, 125 (1990).

[69] G. D. Dracoulis *et al.*, Nucl. Phys. A **486**, 414 (1988).

[70] R. A. Bark *et al.*, Nucl. Phys. A **514**, 503 (1990).

[71] G. D. Dracoulis *et al.*, Nucl. Phys. A **383**, 119 (1982).

[72] F. W. N. De Boer *et al.* Phys. A **290**, 173 (1977).

[73] S. Juutinen *et al.*, Nucl. Phys. A **526**, 346 (1991).

[74] K. Neergard and P. Vogel, Nucl. Phys. A **145**, 33, (1970).

[75] F. G. Kondev *et al.*, Phys. Rev. C **61**, 011303(R) (1999).

[76] P. D. Cottle and V. Zamfir, Phys. Rev. C **54**, 176 (1996).

[77] P. D. Cottle and V. Zamfir, Phys. Rev. C **58**, 1500 (1998).

[78] A. F. Barfield, J. L. Wood, and B. R. Barrett, Phys. Rev. C **34**, 2001 (1986).

[79] W. -T. Chou, R. F. Casten, and V. Zamfir, Phys. Rev. C **45**, R2545 (1992).

[80] Y. A. Akovali, Nucl. Data Sheets **84**, 1 (1998).

[81] R. D. Page *et al.*, Phys. Rev. C **53**, 660 (1996).

[82] J. R. H. Scheinder, Daresbury Report No. GSI-84-3 (1984).

[83] A. Siivola, Nucl. Phys. **84**, 385 (1966).

[84] H. Gauvin *et al.*, Nucl.Phys. A **208**, 360 (1973).

[85] R. A. Bark *et al.*, Nucl. Phys. A **514**, 503 (1990).

[86] F. G. Kondev *et al.*, *to be published.*

[87] R. A. Bark *et al.*, Nucl. Phys. A **657**, 113 (1999).

[88] B. Cederwall *et al.*, Z. Phys. A **337**, 283 (1990).

[89] M. W. Rowe *et al.*, Phys. Rev. C **65**, 054310 (2002).

[90] P. J. Sellin *et al.*, Z. Phys. A **338**, 245 (1991).

[91] J. Simpson *et al.*, J. Phys. G **18**, 1207 (1992).

[92] M. P. Carpenter *et al.*, *to be published.*

[93] J. Gerl *et al.*, Nucl. Phys. A **443**, 348 (1985).

[94] A. Melerangi *et al.*, Phys. Rev. C **68**, 041301 (2003).

[95] B. Cederwell *et al.*, Phys. Rev. C **43**, R2301 (1991).

[96] G. D. Dracoulis *et al.*, Nucl. Phys. A **534**, 173 (1991).

[97] A. J. Larabee *et al.*, Phys. Lett. B **169**, 21 (1986).

[98] C. N. Davids *et al.*, Phys. Rev. C **55**, 2255 (1997).

[99] M. P. Carpenter *et al.*, *to be published.*

[100] J. Uusitalo *et al.*, Z. Phys. A **358**, 375 (1997).

[101] V. G. Soloviev, *Theory of Complex Nuclei*, Pergamon Press, (2000).

[102] C. Cabot *el al.*, Nucl. Phys. A **241**, 341 (1975).

[103] P. M. Davidson *et al.*, Nucl. Phys. A **657**, 219 (1999).

[104] F. Meissner *el al.*, Z. Phys. A **343**, 283 (1992).

[105] K. S. Toth *et al.*, Phys. Rev. C **58**, 1310 (1998).

[106] G. Poli *et al.*, Phys. Rev. C **59**, R2979 (1999).

[107] G. D. Dracoulis *et al*, Nucl. Phys. A **534**, 173 (1991).

[108] R. Bark *et al.*, Nucl. Phys. A **646**, 399 (1999).

[109] C. J. Gallagher and S. A. Moszkowski, Phys. Rev. **111**, 1282 (1958).

[110] R. Bark *et al.*, Phys. Rev. C **67**, 014320 (2003).

[111] Y.-H. Zhang *et al.*, Chin. Phys. Lett. **18**, 1323 (2001).

[112] Y.-H. Zhang *et al.*, Phys. Rev. C **65**, 014302 (2002).

VITA

The author was born in Georgetown, Penang, Malaysia on January 22, 1974. He attended La Salle primary school in Penang, and finished his primary education in SRKSJ primary school (Selangor, Malaysia). He attended SMKSJ high school (Selangor) and obtaining his high-school diploma in 1992. He completed his pre-Univestiy study (Form 6) at TAR College in 1993.

He earned his associate degree from Inti College (Malaysia) and transfered to the University of Oklahoma (Norman, OK) in 1995. In December 1996, he obtained a B.S. degree in Astrophysics. In Fall 1997, he attended the University of Tennessee (Knoxville, TN) as a graduate teaching assistant. In 1999, he accepted a research assistantship to study experimental nuclear physics under the supervision of Dr. Lee Riedinger.